Kinetic modelling of glutamate transport and anion channel function of vesicular glutamate transporters

Inaugural-Dissertation

Zur Erlangung des Doktorgrades

der Mathematisch-Naturwissenschaftlichen Fakultät

der Heinrich-Heine-Universität Düsseldorf

vorgelegt von

Bart Borghans

Jülich, October 2024

Aus dem Institut für Biologische Informationsprozesse (IBI-1)

Molekular- und Zellphysiologie

des Forschungszentrums Jülich

Gedruckt mit der Genehmigung der

Mathematisch-Naturwissenschaftlichen Fakultät der

Heinrich-Heine-Universität Düsseldorf

Berichterstatter:

1. Prof. Dr. Christoph Fahlke
2. Prof. Dr. Christine Rose

Tag der mündlichen Prüfung:

21 October 2025

I. Table of contents

II. List of illustrations

Figures

Tables

III. Abbreviations

Physiologically relevant ions

Asp^-	Aspartate
Ca^{2+}	Calcium
Cho^+	Choline
Cl^-	Chloride
$Gluc^-$	Gluconate
$Glut^-$	Glutamate
H^+	Proton, hydrogen ion
HCO_3^-	Bicarbonate
K^+	Potassium
Na^+	Sodium
NO_3^-	Nitrate
OH^-	Hydroxide
P_i	Inorganic phosphate

General terms

[*x*]	Concentration of substance *x* in mol/L
AMPA	α-amino-3-hydroxy-5-methyl-4-isoxazolepropionic acid
ATP	Adenosine triphosphate
apo	Apoprotein or apoenzyme, required cofactors are not bound
CHES	N-Cyclohexyl-2-aminoethanesulfonic acid
CNS	Central nervous system
DgoT	D-galactonate transporter
DMEM	Dulbecco's Modified Eagle Medium

e	Elementary charge, electric charge of H^+ or electrons (1.602×10^{-19} C)
eGFP	Enhanced green fluorescent protein
EGTA	Ethylene glycol-bis (β-aminoethyl ether)-N,N,N′,N′-tetraacetic acid
GlpT	Glycerol-3-phosphate transporter
GS	Glutamine synthetase
HEPES	4- (2-hydroxyethyl)-1-piperazineethanesulfonic acid
K_D	Dissociation constant, ratio of unbinding to binding rates of a complex
MES	2- (N-morpholino)ethanesulfonic acid
NMDA	*N*-methyl-D-aspartic acid
PAC	Proton-activated chloride channel
PAG	Phosphate-activated glutaminase
pH	Reciprocal metric for acidity, approximated as $-\log_{10}([H^+])$
pK_a	Negative base-10 logarithm of acid dissociation constant K_a
pK_M	Non-equilibrium equivalent of pK_a using the Michaelis constant K_M
$VGLUT1_{PM}$	Plasma membrane-targeted mutant of VGLUT1
RB	Rose Bengal
RSS	Residual Sum of Squares
TMA-OH	Tetramethylammonium hydroxide
WT	Wild type, non-mutated typical variant of protein

IV. Abstract

Vesicular glutamate transporters load glutamate into synaptic vesicles and play an integral role in neuronal signal transduction. This work describes the function of these transporters with a combination of cellular electrophysiology and kinetic modelling. A mutant transporter with increased plasma membrane expression, generated by the neutralisation of its cellular targeting sequence ($VGLUT1_{PM}$), was heterologously expressed in HEK293T cells and characterised with whole-cell patch clamp electrophysiology. VGLUTs have multiple transport modes. They function not only as secondary active H^+-glutamate exchangers but also as Cl^- channels. These transport functions were analysed at different voltages as well as at external pH and Cl^- concentrations. The Cl^- channel was simulated with open and closed states that are either not, singly, or doubly protonated and can all additionally bind a Cl^- ligand. This model describes all experimental results, especially the activation and deactivation of voltage jumps or changes in pH and $[Cl^-]$. Kinetic analyses show that bound Cl^- supports the first protonation of VGLUT1 allosterically and stabilises the open channel, primarily when it is singly protonated. Histidine 120 appears to play an important role in the way allosteric Cl^- promotes channel opening, which increases steady-state current and the activation rate during pH- and voltage jumps. Neutralisation of this amino acid causes increased Cl^- dissociation rates and reduces opening under single protonation. H120A $VGLUT1_{PM}$ mostly opens from doubly protonated states. The transport of glutamate and aspartate was simulated with an alternating access mechanism that requires double protonation for substrate binding. The transition from the inward- to the outward-facing conformation with glutamate bound is negligible as long as no proton dissociates and occurs only in the singly protonated state. After the translocation, glutamate dissociates only after re-protonation on the luminal side of the membrane. Cl^- allosterically activates the transport of glutamate by increasing the glutamate binding rates and supports transitions in the transport cycles. An increase in the pK_a prevents cytoplasmic deprotonation after aspartate is bound, which causes it to be translocated in the doubly protonated state. The difference in protonation between glutamate and aspartate transport leads to H^+-glutamate exchange and to the uniport of aspartate.

V. Zusammenfassung

Vesikuläre Glutamattransporter beladen synaptische Vesikel mit Glutamat und spielen eine Schlüsselrolle in der neuronalen Signalübertragung. In dieser Arbeit wurde die Funktion dieser Transporter mit einer Kombination aus zellulärer Elektrophysiologie und kinetischer Modellierung beschrieben. Ein mutanter Transporter mit erhöhter Plasmamembranexpression durch Neutralisierung der zellulären Zielsequenz ($VGLUT1_{PM}$) wurde in HEK293T-Zellen heterolog exprimiert und mit Ganzzell-Patch-Clamp-Elektrophysiologie charakterisiert. VGLUTs können mehrere Transportfunktionen vermitteln. Sie sind nicht nur sekundär-aktive H^+-Glutamat-Austauscher, sondern auch Cl^- Kanäle. Diese Transportfunktionen sind bei unterschiedlichen Spannungen sowie externen pH und Cl^--Konzentrationen analysiert. Der Cl^--Kanal wurde mit geschlossenen und offenen Zuständen simuliert, die entweder nicht, einfach oder doppelt protoniert sind und entweder einen Cl^- Liganden binden oder nicht. Dieses Modell beschreibt alle experimentellen Befunde, insbesondere die Aktivierung und Deaktivierung durch Spannungssprünge oder Änderungen in pH und [Cl^-]. Kinetische Analysen zeigen, dass gebundenes Cl^- die erste Protonierung von VGLUT1 allosterisch erleichtert und den offenen Kanal stabilisiert, hauptsächlich im einfach protonierten Zustand. Histidin 120 scheint eine wichtige Rolle dabei zu spielen, wie allosterisches Cl^- die Kanalöffnung fördert, was den stationären Strom und die Aktivierungsrate bei pH- und Spannungssprüngen erhöht. Neutralisierung dieser Aminosäure führt zu erhöhten Cl^--Dissoziationsraten und weniger Öffnungen durch einfache Protonierung. H120A $VGLUT1_{PM}$ aktiviert vorwiegend im doppelt protonierten Zustand. Der Transport von Glutamat und Aspartat wurde mit einem alternierenden Zugangsmechanismus simuliert, der die doppelte Protonierung zur Bindung eines Substrats erfordert. Der Übergang von der inneren zur äußeren Konformation mit gebundenem Glutamat ist, solange kein Proton dissoziiert ist, vernachlässigbar und passiert nur im einfach protonierten Zustand. Nach der Translokation dissoziiert Glutamat nach einer erneuten Protonierung auf der luminalen Membranseite. Cl^- aktiviert den Glutamattransport allosterisch durch Erhöhung der Glutamat-Bindungsraten und erleichtert den Übergang im Transportzyklus. Nach Bindung von Aspartat verhindert ein hoher pK_a-Wert die zytoplasmatische Deprotonierung und Aspartat translociert im doppelt protonierten Zustand. Die unterschiedliche Protonierung während Glutamat- und Aspartattransport führt zum H^+-Glutamat-Austausch und zum Aspartat-Uniport.

1. Introduction

1.1 Neurotransmission

Our nervous system processes incoming information and links it to rapid physiological responses at different scales. Santiago Ramón y Cajal demonstrated that this information processing relies on the close and effective interaction of individual neurons at synaptic connections (Lopez-Munoz et al., 2006 [1]). The brain is probably the most important and well-known part of this network of neuronal cells, spanning the body and connecting to all sensory organs (Nickel, 2004 [2]). While many differences exist, the mechanisms underlying this system in humans are equivalent to those in other living animals, with rare exceptions like sponges that lack it altogether (Sakarya et al., 2007 [3]). Similar to a computer with several inputs and outputs connected by cables, the brain receives electrical signals via neurons in both the central and peripheral nervous system. While other cells in the body tend to be more compact, the membrane enclosing neurons forms characteristic appendages (Figure 1, left) that reach away from the nucleus.

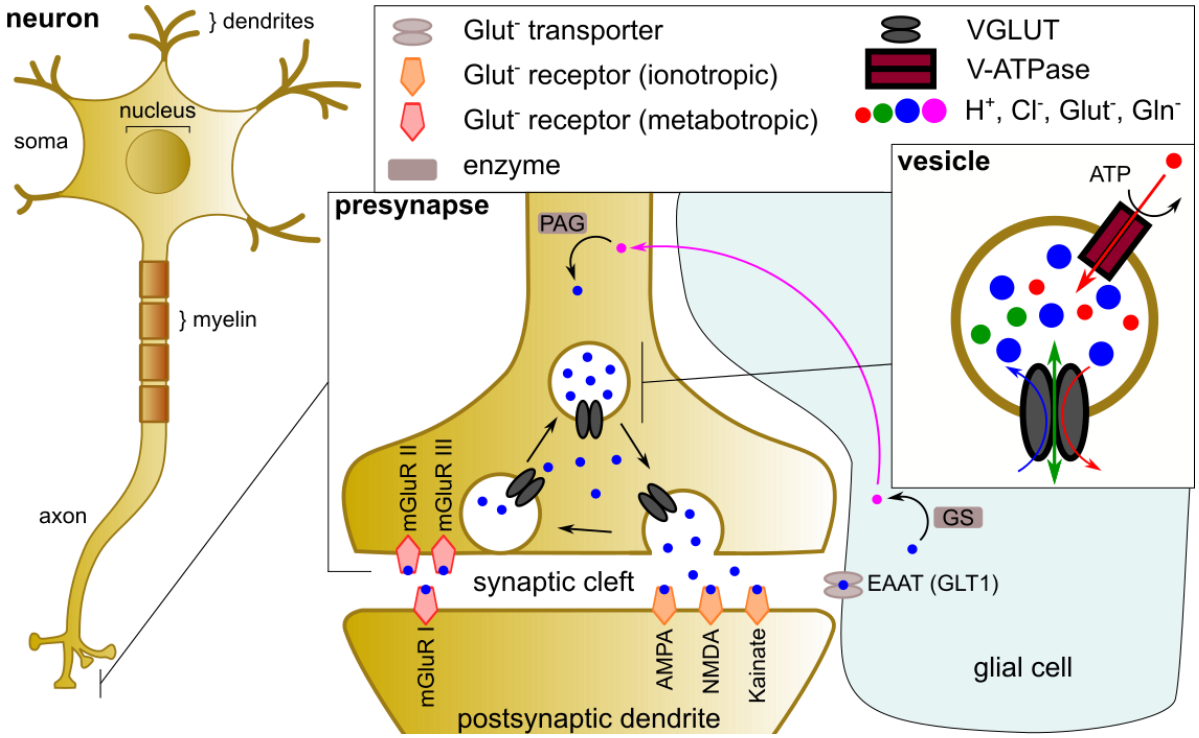

Figure 1: anatomy of the neuron and glutamatergic signalling. *Excitable neuron with its axon supported by a myelin sheath (left), presynaptic axon releasing Glut⁻ into the synaptic cleft where it is bound by dendritic and glial receptors (middle), and synaptic vesicle with VGLUT (right) functioning as both an active Glut⁻ transporter (driven by the proton gradient established by a V-ATPase) and as a Cl⁻ channel. The glutamine synthetase (GS) and phosphate-activated glutaminase (PAG) enzymes facilitate recycling of Glut⁻ as glutamine via glial cells.*

Signal transduction tends to be directional, where external stimulation through the dendrite of a neuron can be passed on through its axon. Axons are often orders of magnitude longer

than the soma and connect to other neurons. This connection is not necessarily linear but can branch to multiple other cells and split into multiple pathways (Han et al., 2018 [4]). Barely a century ago, neuronal signalling was first recorded through substances now known as neurotransmitters by demonstrating that heart rate is chemically regulated by soluble acetylcholine (Loewi, 1921 [5]). Many neurotransmitters have been found since then, with glutamate, referred to as $Glut^-$ (the anionic form of the amino acid glutamic acid) being the primary excitatory neurotransmitter in humans and other vertebrates (Meldrum, 2000 [6]). When excreted into a synapse by presynaptic cells, it drives signalling by binding to receptors of postsynaptic cells, promoting the initiation of action potentials.

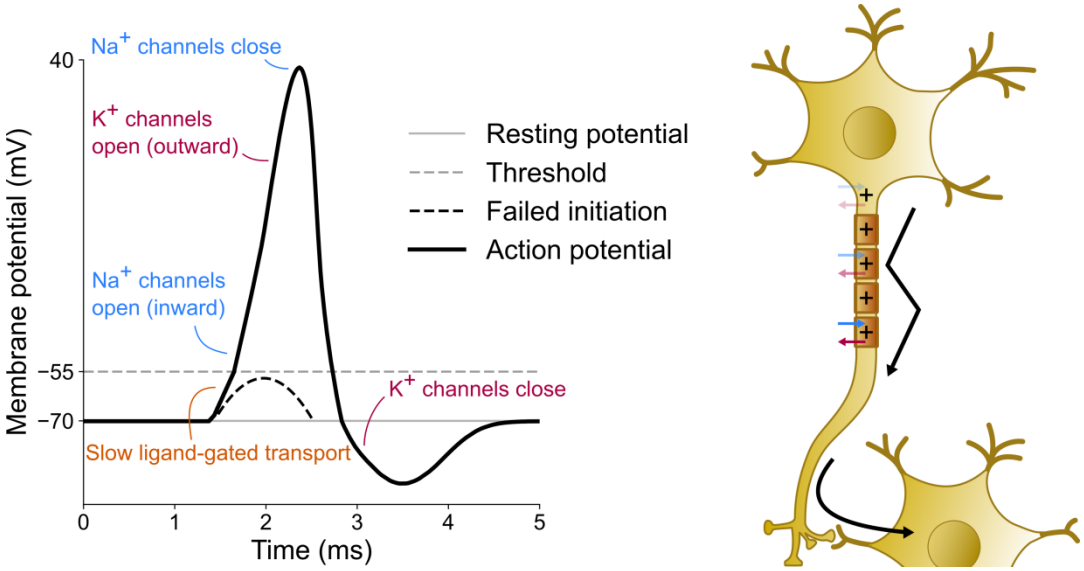

Figure 2: main cation channel action and current flow during an action potential. *Processes responsible for the depolarisation phase leading to the peak of an action potential, and those causing the repolarisation that brings the membrane potential back down (left), and this effect responsible for triggering the $Glut^-$ release shown in dark blue in the middle of Figure 1 running along the cell membrane of excitable neurons (right).*

Through a cascade of activations and deactivations of membrane proteins, the voltage across the membrane changes rapidly. Under the influence of excitatory neurotransmitters, positive charge entering through ligand-activated ion channels induces slight depolarisation from the resting membrane potential of approximately −70 mV. If the resulting reduction of negative voltage exceeds the threshold of the cell, an action potential is generated. Voltage-gated Na^+ channels open, allowing Na^+ to enter the cell and to rapidly drive the membrane voltage up to and beyond 0 mV. The resulting positive potential activates K^+ channels, which then cause K^+ to flow out of the cell, thereby repolarising it. In many neurons, the membrane potential even dips below its starting value and the end of the action potential. The action potential runs along the neuron and its axon, activating Ca^{2+} channels, which causes a cascade of Ca^{2+} flowing into the cytosol of the presynaptic nerve ending. This triggers the fusion of synaptic vesicles to the membrane of presynaptic nerve terminals and release of their contents to the extracellular space, functioning as a chemical signal across the synaptic

cleft that allows the sequence to repeat and continue through other neurons (Rusakov, 2006 [7]).

Glutamatergic signals between neurons are mediated via a variety of receptors, divisible into two categories: ionotropic and metabotropic. The ionotropic glutamate receptors, the iGluRs, are ion channels that activate pathways downstream by depolarising postsynaptic membranes. AMPA receptors are the first of the main three superfamilies in this category and are permeable to multiple cations such as Na^+, K^+, and Ca^{2+}. Their high speed of activation makes them a major component of fast synaptic transmission (Platt, 2007 [8]). They also have an essential role in synaptic plasticity, where their activity is required for the strengthening of synaptic activity through long-term potentiation (Maren et al., 1993 [9]). With a more delayed influx of mostly Na^+ and K^+, the family of Kainate receptors plays a smaller role in transmission and synaptic plasticity (Contractor et al., 2000 [10]). Finally, NMDA receptors are known for their central role in excitotoxicity, overstimulation of receptors in and near the synapse leading to damage or death of nerve cells (Hardingham et al., 2002 [11]). They also affect neuroplasticity via their Ca^{2+} conductance (Carvajal et al., 2016 [12]).

There are also metabotropic $Glut^-$ receptors (mGluRs) that affect neuronal function downstream in a less direct way. These are found on both sides of the synaptic cleft and mainly modulate the activity of NMDA receptors, thereby affecting neuroplasticity. Based primarily on these characteristics, the eight receptors in this class are divided into three groups. Group I contains mGluR 1 and 5, which are mostly expressed postsynaptically and increase NMDA activity. Group II consists of mGluR 2 and 3, while the remaining mGluR 4, 6, 7, and 8 are in group III. Groups II and III are distinguished by their interaction with agonists and antagonists, and they are both mainly expressed in the presynapse, where they decrease NMDA activity (Shigemoto et al., 1997 [13]).

Although they are dual-function proteins with a channel function that is selective for other anions, excitatory amino acid transporters (EAATs) are named for their active transport of glutamate across cell membranes (Fahlke et al., 2016 [14]). EAAT2 and, to a lesser extent, EAAT1, are responsible for approximately 90% of human glutamate uptake from the synaptic cleft (Anderson et al., 2000 [15]). This transport utilises gradients of Na^+ and K^+, exchanging each $Glut^-$ with 3 Na^+ and 1 H^+ against a single K^+ cation (Zerangue et al., 1996 [16]). All five human EAATs use similar transport mechanisms (Mim et al., 2005 [17]). This process loads $Glut^-$ mostly into the glial cells surrounding the neurons, specifically astroglia (Cisneros et al., 2014 [18]). The glia internally metabolise part of the $Glut^-$ into glutamine using glutamine synthetase (GS), after which it is transported into neurons where phosphate-activated glutaminase (PAG) converts it back into $Glut^-$ (Martinez-Hernandez et al., 1977 [19]). A combination of this recycling and newly synthesised $Glut^-$ allows the neuronal pool to be

maintained. If this recycling is impeded, excess Glut⁻ in the extracellular space causes neurotoxicity—at least in part through excitotoxicity (Lau et al., 2010 [20]).

1.2 Vesicular glutamate transporters

The aforementioned EAATs, expressed mainly in the plasma membrane of glial cells, are not the only transporters of Glut⁻ that are relevant for neuronal function (Danbolt, 2001 [21]). Vesicular glutamate transporters (VGLUTS) accumulate Glut⁻ in synaptic vesicles. There are three human VGLUTs, VGLUT 1–3, proteins encoded in genes named SLC17A7, SLC17A6, and SLC17A8, respectively (Reimer, 2013 [22]). They are members of the SLC17 family of solute carriers, which itself is part of the major facilitator superfamily. VGLUTs are important for normal neurological function. All three VGLUT proteins are highly homologous in both structure and function, despite varying expression levels across the brain (Fremeau et al., 2004 [23]). VGLUT2 is the only VGLUT with a resolved 3D structure (Figure 3), obtained via cryo-EM (cryogenic electron microscopy) of the protein as found in rats (Li et al., 2020 [24]).

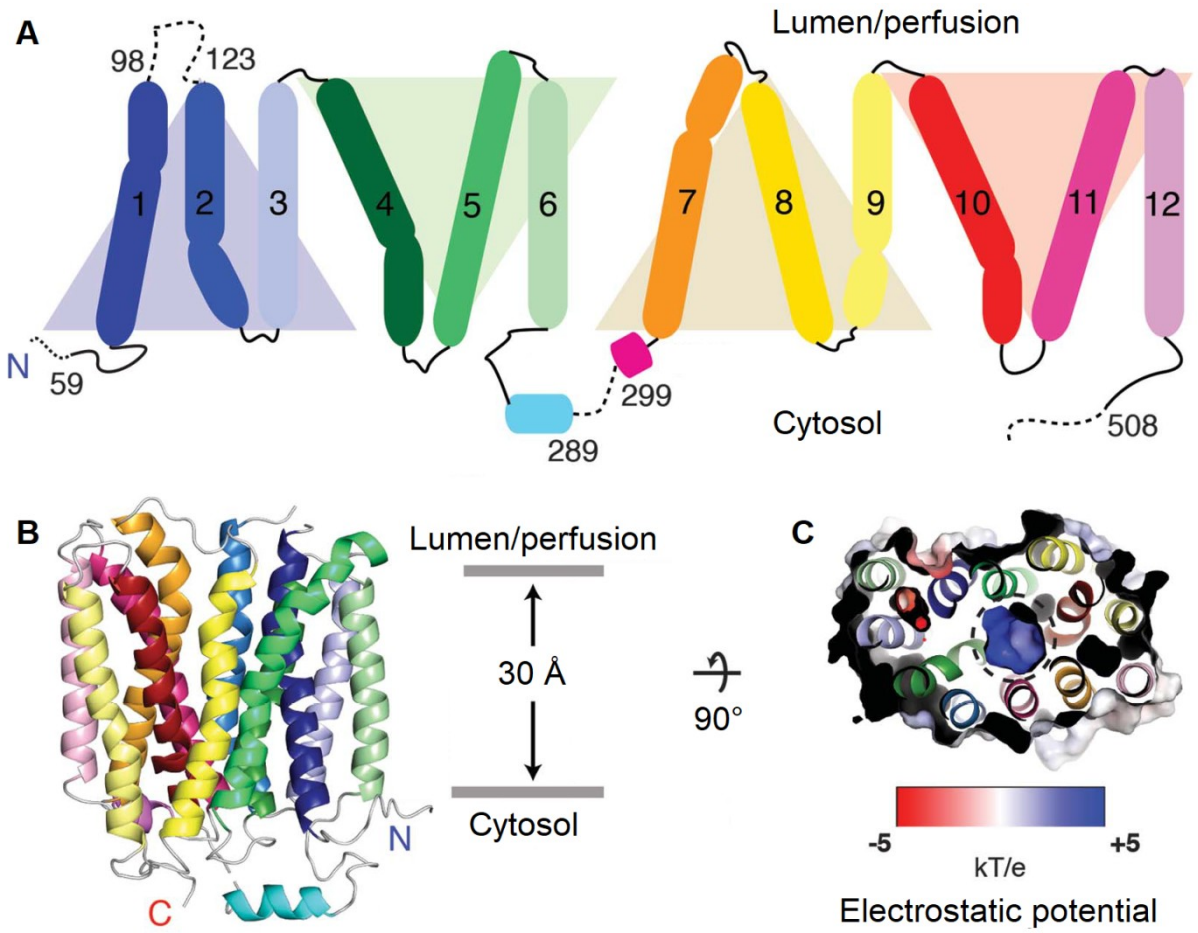

Figure 3: cryogenic electron microscopy-based protein structure of VGLUT2. *Simplified residue distribution into helices (A), 3D orientation of transmembrane helices with grey lines indicating membrane location from a side view (B), and electrostatic surface centred on positively charged pore as seen from the cytosol (C) as an outward/lumen-facing approximation of VGLUT1. The lumen/perfusion side faces the centre of the vesicle when expressed therein, but faces the perfusable outside the cell when expressed in the plasma membrane. This figure was adapted from Figure 1 in a published work (Li et al., 2020 [24]).*

Research is currently performed with the understanding that all three VGLUTs, the human proteins as well as their rat equivalent, consist of 500–600 amino acids that form twelve transmembrane helices around a central pore lined with positively charged residues. Both the N- and C-termini are on the cytosolic side of the membrane, accompanied by a cytosolic loop connecting helix 6 to helix 7. Just like many other proteins, genetic variants are known to affect the function of VGLUTs—both those originating from human experimentation and naturally occurring mutations that may or may not cause disease symptoms. With $Glut^-$ transport being its defining characteristic, a good way to investigate the underlying mechanisms is to contrast proteins to variants that differ in minor features but are otherwise as similar as possible. A histidine in transmembrane domain 2 (residue 120 in VGLUT1, 128 in VGLUT2) is a suitable example of this. The histidine was originally identified in VGLUT2 and is conserved in all VGLUTs but not in other anion transporters (Juge et al., 2006 [25]). It maintains a similar location across VGLUTs, near the central binding pocket of the protein. Disabling the chemical influence of the histidine through mutation abolishes normal $Glut^-$ transport, demonstrating that this function is heavily dependent on the histidine.

1.3 VGLUT transport modes

$Glut^-$ transport by VGLUTs is fuelled by a proton electrochemical gradient, which is maintained by the vacuolar-type ATPase (V-ATPase). This allows the inside of vesicles to be more acidic than typical cells, with a pH of approximately 5.7 based on fluorescence measurements (Egashira et al., 2015 [26], Miesenböck, 1998 [27]). $Glut^-$ transport is also enhanced by Cl^- within the vesicular lumen, which appears to turn into inhibition when its concentration exceeds 10 mM (Naito et al., 1985 [28]). VGLUTs also transport inorganic phosphate (P_i) into synaptic vesicles, which competes with $Glut^-$, but its affinity is noticeably lower at 4.3 mM compared to $Glut^-$+P_i with 1.44 mM and just $Glut^-$ with 1.09 mM (Preobraschenski et al., 2018 [29]).

It was initially thought that $Glut^-$ uptake into synaptic vesicles is the product of uniport, driven primarily by the electrical component of the membrane potential and only secondarily affected by a chemical pH gradient (Eriksen et al., 2020 [30]). While this conclusion rested largely on a perceived lack of evidence for the antiport of protons, it fits with findings such as imaging experiments tracking vesicle loading through various proteins. These reported clear evidence for VGAT being an antiporter but did not draw the same conclusion for VGLUT (Farsi et al., 2016 [31]). Regardless, these findings are also compatible with the strong voltage dependence of VGLUT $Glut^-$ transport through exchange for protons. Evidence appears to be increasingly in favour of the role of vesicular pH gradients being an integral component of VGLUT antiporter activity (Farsi et al., 2017 [32]). Live-cell imaging with fluorescent pH probes (Martineau, 2017 [33]) and Nernst potential calculations incompatible

with $Glut^-$ uniporter function of $VLGUT1_{PM}$ (Kolen et al., 2023 [34]) suggest the antiporter mechanism is a valid assumption to make—at least with this specific construct.

While there appear to be no direct measurements or solid evidence for the membrane potential of vesicles, it was roughly estimated to approach 80 mV after they separate from the plasma membrane (Pietrancosta et al., 2020 [35]). Their voltage dependence reportedly allows VGLUTs to fill vesicles with between 60 mM $Glut^-$, quantified in immunoisolated vesicles (Burger et al., 1989 [36]), and a maximum of 150 mM $Glut^-$ calculated using the Donnan rule (Takamori et al., 2006 [37]), up from 5–10 mM in the cytosol (Omote et al., 2011 [38]). This is surprising, as the difference is smaller than one would expect from active transport powered by proton coupling. If these numbers are correct, it could be an indication that $Glut^-$ has a way to escape the vesicles. Alternatively, fully exporting the Cl^- during loading may disable its allosteric effect and prevent VGLUTs from reaching their saturation concentration of $Glut^-$.

The transport rate of $Glut^-$ by $VGLUT1_{PM}$, heterologously expressed in the plasma membrane of HEK293T cells, has been determined with 40 mM extracellular Cl^- at pH 5.5 and −160 mV (Kolen et al., 2023 [34]). It was calculated by multiplying the ratio of fluorescence-normalised $Glut^-$ and Cl^- current (approximately 1:32), measured with whole-cell patch clamp, by the effective or average unitary VGLUT1 Cl^- current (5.8 fA, the open unitary current of 24 fA multiplied by the calculated open probability of 0.24). This provides a combined $Glut^-$ and H^+ antiport of 0.18 fA, and dividing by twice the elementary charge (e) to account for the transport of two ions gives a $Glut^-$ transport rate of 561 ± 123 s^{-1} (mean and 95% confidence interval).

VGLUTs are known for their active transport, but they also allow anion currents to pass through in a channel mode. This channel is dependent on [Cl^-], pH, and membrane potential. It appears to mainly facilitate Cl^- conductance *in vivo*, reducing the concentration of circa 120 mM in vesicles after endocytosis (Martineau, 2017 [33], Maycox et al., 1990 [39]). Where active transport typically involves a series of binding steps involving a substrate and conformational changes to move it in a certain direction, channels operate via different mechanisms. Many are gated and still undergo conformational changes in order to facilitate conditional permeability, including VGLUTs, but the passage through which this occurs is typically wide or fast enough to avoid discrete binding events (Hille, 2001 [40]). These features contribute to a lack of strict conductance stoichiometry in channels compared to active transport, and the regulation of channel activity is typically viewed as transitioning between “open” and “closed” states instead (Chay, 1988 [41]). Exploring different physiological functions requires careful control of the conditions, especially since VGLUTs

are known to conduct multiple ion types via both of these transport modes (Kolen et al., 2023 [34]).

1.4 Research goal

The purpose of this work is to describe the mechanisms of VGLUT $Glut^-$ transport and anion channel function by experimentally characterising this behaviour under various conditions and simulating the modulation in kinetic models. Since cytosolic concentrations do not seem to undergo major modification during synaptic function, such models can be simplified to only account for the effects of luminal pH, and [Cl^-] (Martineau, 2017 [33]). Similar to how neuronal action potentials were described by Hodgkin, Huxley, and Katz in the 1950s (Hodgkin et al., 1952 [42]), a properly defined set of physiologically relevant kinetic properties can describe the sequence of molecular processes that enable and modulate current through the protein. If the kinetic constants converge on a simulation with sufficient accuracy, the behaviour of the protein can be simulated given only the conditions, for functions such as the Cl^- channel and $Glut^-$-proton exchange of VGLUT1, as modulated by membrane V, pH and [Cl^-]. Kinetic models predict various characteristics of the protein they describe, such as ligand affinities and conformational changes. Variations in activity can be modelled, induced by a choice in substrates between $Glut^-$ and Asp^- or between WT and H120A VGLUT1. The kinetic parameters can be analysed and contrasted to validate the transport mechanisms themselves and provide novel insights into the chain of cause and effect driving vesicular ion conductance.

2. Materials and methods

2.1 Constructs

The transfection and induction strategies for the patch clamp experiments used rely on pcDNA3.1 vectors containing the VGLUT constructs, along with an enhanced green fluorescent protein (eGFP) tag at their C-terminus. The sequence for WT VGLUT1 was taken from the common brown rat (Rattus norvegicus), the protein version for which the majority of available structural information was generated using cryo-EM analysis of VGLUT2 (Li et al., 2020 [24]). Whereas many protein types can have their function investigated quite well *in vitro*, those that function through permeation have to be inserted into a membrane within a controlled environment. With their physiological functions in neurons and especially in vesicles, VGLUTs are expressed minimally in the plasma membrane of HEK293T cells by default. Previous research has identified amino acid sequences at the N-terminus (E_6, E_7, L_{11}) and C-terminus (E_{505}, E_{506}, F_{510}, V_{511}) of VGLUT1, responsible for targeting the protein to vesicles in the cytosol. Mutating these residues to alanine results in a significant portion of protein expression shifting to the plasma membrane, as previously shown for both VGLUT1 (Foss et al., 2013 [43]) and VGLUT2 (Eriksen et al., 2016 [44]). This construct, hereafter referred to as $VGLUT1_{PM}$, was used for the WT, point mutation H120A, and inactive triple mutant H191K H426K D428Q (Kolen et al., 2023 [34]).

$VGLUT1_{PM}$ is visibly expressed in the plasma membrane, but the transfection procedure that inserts the DNA into cells could theoretically alter membrane structure to make it measurably permeable. This introduces the risk of protein-independent currents, leading to false positives in the measured constructs. To test for this, the $VGLUT1_{PM}$ was compared to an inactive triple mutant, H191K-H426K-D428Q. It is transfected and expressed normally, but its altered glycosylation minimises plasma membrane targeting and reduces current below even that of the unmodified WT (Figure 4). This confirms that the unmodified WT allows for a small amount of Cl^- current across the plasma membrane and that the protein $VGLUT1_{PM}$, not merely the transfection process, is responsible for its significantly improved current compared to controls. Because they have minimal current output and consequently negligible gating, the measurement protocol used for the triple mutant was shorter than those applied to other constructs.

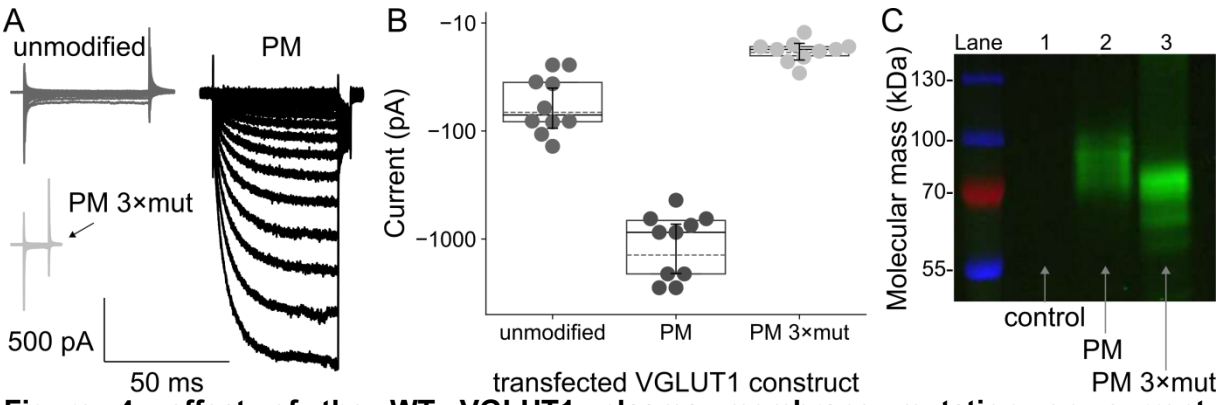

Figure 4: effect of the WT VGLUT1 plasma membrane mutation on current. *Representative current traces of unmodified, PM-mutated, and triple mutation of the PM mutant constructs of VGLUT1 (A), quantified current for each of the constructs with error bars depicting a 95% confidence interval (B), and SDS-PAGE lysates from two experiments showing GFP-tagged protein expression in HEK293T cells compared to untransfected cells as controls (C). Panel C was adapted from the SDS-PAGE results of Supplementary Figure 2i in a published work (Kolen et al., 2023 [34]). Here, lysates were visualised using a fluorescence gel scanner (Typhoon FLA9500, GE Healthcare) at 100 µm resolution, with eGFP excited at 473 nm and emissions recorded using a 530/20 bandpass filter.*

2.2 Cell culture

All measurements on VGLUT variants were performed on HEK293T (Sigma-Aldrich, Burlington, Massachusetts, USA) cells, cultured in DH10 medium (500 mL DMEM, 50 mL FBS, and 5 mL Penicillin-Streptomycin at 5000 U/mL) at 37°C with 5% CO_2. Experiments were generally performed starting at passage 3 to give the cells time to stabilise, which were replaced by a new frozen batch at passage 13 to limit the risk of degradation of the cells.

For various experiments with consistently high current, mostly involving permeation of Cl^- and NO_3^- with high external [Cl^-], thawed aliquots of Flp-In T-Rex stable cell lines were used. These use the same HEK293T cells and an application of the Flp-In T-REx (Thermo Fisher Scientific) regulated gene expression system. It is based on the Flp recombination system found in yeast as well as tetracycline repressor (TetR) and tetracycline operator (TetO) sequences (Hillen et al., 1994 [45]). The Flp-In stable cell lines were already equipped with the desired construct, requiring overnight induction through incubation with approximately 2.5 µg tetracycline (1.5 mg per mL of 70% ethanol solution) per mL medium for each seeded 5 cm Petri dish. This provides the advantage of faster and more consistent sample generation, where the uniform but lower expression is sufficient.

After confirming general comparability to results obtained from Flp-In stable cell lines, other permeable anions and conditions with lower current were transiently transfected with the same constructs. While some of these transfections were done with PEI MAX or Lipofectamine 2000 reagents (Thermo Fisher Scientific, 24-hour incubation with 3 µg DNA or 7-hour incubation with 2 µg DNA, respectively), performance was not noticeably better than

the primarily used calcium phosphate method. The calcium phosphate transfection was performed with 1 µg DNA in approximately 1 µL H_2O. This was mixed with 42 µL H_2O, 123 µL CaCl, and 165 µL 2× HEBS, distributed over a largely confluent 5 cm Petri dish, and incubated for at least 20 hours. Cells were grown to near-confluence in separate 5 cm Petri dishes for each day of experimentation and then seeded (after transfection, but prior to induction when using stable cell lines) into the 5 cm dishes from which they were patched the next day. No differences were found between the experimental results obtained through various transfection methods.

2.3 Patch clamp electrophysiology

VGLUT transport can be measured as electric current flowing through the membrane using the well-established patch clamp technique, largely credited to work done by Neher and Sakmann in the 1980s, which eventually earned them a shared Nobel Prize (Sakmann et al., 1984 [46]). The *voltage clamp* mode sets a voltage over the measured system so that current can be recorded. Currents passing through the membrane of a single cell are typically recorded with the use of a small glass pipette, the content of which becomes the local liquid environment and conducts membrane ion flow via aqueous electrolytes and an electrode inside the pipette. An external reference electrode closes the circuit through the bath solution.

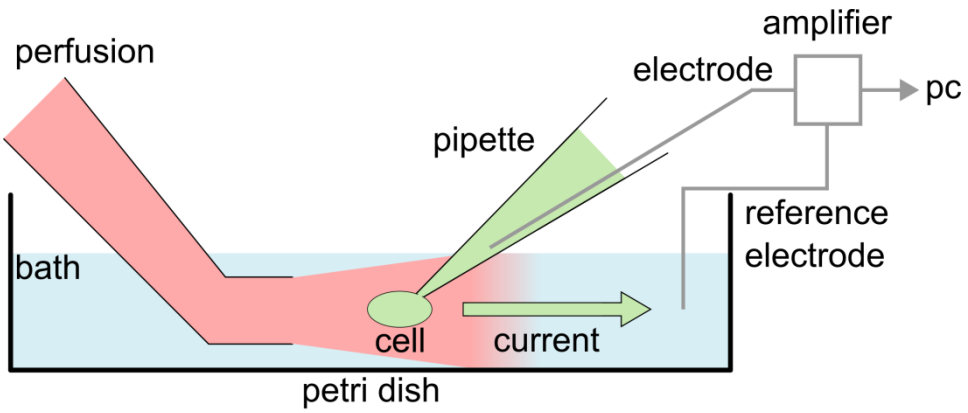

Figure 5: side view of a typical whole-cell patch clamp experiment in a Petri dish. The internal solution containing a transported ion is shown in green and perfusion with an external solution in red. The amplifier in voltage-clamp mode sets a negative membrane potential across the cell, which triggers the conductance of negative ions out of the cell and towards the more positive external reference electrode, and measures the resulting current flow.

Achieving solid contact with a cell, commonly named a gigaseal after its 1,000,000 Ω electrical resistance, initially enables the use of a *cell-attached patch* that primarily measures transport through the small piece of membrane enclosed by the pipette. From here, this area of the membrane can be made porous using chemical agents for a *perforated patch* or ruptured to provide a *whole-cell patch* configuration wherein the pipette solution becomes the internal environment of the cell. Further modifications exist, but whole-cell patch clamp is a

suitable method and was chosen for the analysis of VGLUT currents. All of these patch clamp measurements were performed using a headstage (S/N 520021) and operated via HEKA PatchMaster through an EPC10 amplifier (Multi Channel Systems MCS GmbH, Reutlingen, Germany). The headstage was electronically controlled via a Luigs & Neumann SM-5 micromanipulator control panel, powered by an SM-6 amplifier. Borosilicate capillaries with an internal filament (30-0050 1.2 OD × 0.94 × 100 L mm, Harvard Apparatus) were pulled in half to create pipettes. These were fire-polished for a final open pipette resistance of 1–2 MΩ using a Narishige MF-830 microforge.

Patch clamp electrodes are commonly made out of silver, a material with suitable electrical conductance that allows for effective solution charge exchange when complexed with Cl^-. The Cl^- part of this Ag/AgCl electrode has a strong influence on the activity of VGLUTs, which means it could interfere with experiments performed under deliberate exclusion of this element. Excessive amounts of electrode-associated Cl^- in solution could modulate the current output of VGLUTs while potentially also hampering the conductance between solutions and electrodes when too little of it is available. Salt bridges, plastic tubes filled with a solid gel that are placed over electrodes, can be used to control the number of free ions whenever there is no Cl^- in the solution. This helps with both sides of this problem: the ions in this gel help current pass between the solutions and the electrodes, while also limiting the amount of Cl^- dissociating from the electrode. These bridges were made by heating approximately 2% agarose in 0.5–3 M KCl until it turned liquid and filling thin tubing with it using suction applied by a syringe and connected to it via a needle. The salt bridges were cut to size and stored in a KCl solution to maintain their ionic concentration. The reference electrode was in a bath solution that contained Cl^- by design during nearly all experiments, so the salt bridges were primarily used on the internal electrode during measurements of anions other than Cl^- and NO_3^-.

Measurements were performed at 23°C using a Leica DMIL inverted microscope equipped with a GFP filter to allow for the selection of cells expressing any of the fluorescently tagged VGLUT-based membrane protein constructs. Cells were selected based on isolation, being healthy enough to remain attached to the bottom of the Petri dish during seal formation, and having no aberrant size. Where transient transfection was required for the recording of currents, cells with high fluorescence were additionally sought out. After attaching the pipette with a stable gigaseal (≥2 GΩ), these cells were lifted from the bottom before starting the measurement.

Perfusion was routed through a manually constructed network of polyethylene tubing and other inert plastic connectors. Each solution was gravity-driven from an elevated tube controlled by a three-way valve, also connected to a small syringe to allow for manual

flushing of the system, directly onto cells via a glass or plastic outlet with a suitable flow rate. Default perfusion outlets were placed in the same focal plane as the cell and opened for several seconds to provide a stable environment before recording. For all experiments with various perfusion conditions, the application order of solutions was reversed for approximately half of all measurements to compensate for time-based effects. Cells in experiments with permeable anions that would be overpowered or obscured by Cl^- current were additionally kept at a holding potential below the reversal potential of Cl^-, typically at −50 mV for two minutes. This allows for Cl^- export before analysis and reduces import between the voltage sweeps of individual measurement.

Charged substances in solution have an ionic mobility, which largely determines their diffusion properties. Whenever solutions with different concentrations of these electrolytes meet, a *liquid junction potential* (LJP) is generated from the sum of all diffusion across the contact surface (Zielen, 1963 [47]). Using a variety of concentrations is a standard part of patch clamp perfusion, and the Cl^- that plays a major role in the function of VGLUTs happens to have a mobility value among the highest in these solutions. As a result, experiments with asymmetric Cl^- can reach potentials that exceed individual voltage steps. To account for this, all experiments were compensated for this effect whenever the calculated LJPs reached 10 mV, the smallest voltage step used. Expected junction potential values were calculated using solution ion concentrations and the Junction Potential tool of Axon Clampex (Molecular Devices, San Jose, California, USA). The junction potential between the applied perfusions and the bath solution was subtracted from the junction potential between the pipette solution and the bath solution. The resulting value was entered into HEKA PatchMaster, where the applied voltage is changed by the amplitude of this potential in the voltage protocol. The actual voltage across the cell membrane has the intended value in experiments with standard perfusion. Where significant LJPs were generated in protocols where the solution changes during the voltage sweep, the applied voltage protocol was manually adjusted to align with solution change. Where LJPs were not adjusted *a priori*, the voltage range used in the analysis was shifted by the same amount to correct the values.

2.4 Solutions

The choline cation (Cho^+) was used as the counter-ion for each permeable anion and added with most of the Cl^- on either side of the membrane as ChoCl, which is highly hygroscopic. To avoid the absorbed water from causing weighing inaccuracies, ChoCl was added as a stock solution with a concentration calculated from its measured osmotic concentration. The $[Cl^-]$ in external solutions ranged from 0 to 180 mM, and for lower concentrations it was substituted with $Gluc^-$ up to a total anion concentration of at least 140 mM. The pH for all external solutions was titrated with ChoOH, where some conditions with low pH and reduced

Cl^- required the initial ratio of $Cho^+/Gluc^-$ to be reduced to avoid starting above the target pH. The solutions were buffered with 50 mM MES below pH 7 and with 30 mM HEPES for everything else. Bath solutions had a standard pH of 7.4 and $[Cl^-]$ of 140 mM. Measurements involving lower external $[Cl^-]$ or internal solutions based on large anions that compete with Cl^- transport had a $[Cl^-]$ of 40 mM to stay closer to the optimal allosteric activation of $Glut^-$ and reduce the risk of inward Cl^- current.

Typical internal solutions contained 140 mM of the permeable anion, 5 mM ethylene glycol-bis (β-aminoethyl ether)-N,N,N′,N′-tetraacetic acid (EGTA), and 5 mM magnesium. EGTA is a chelating agent that binds cations, primarily Ca^{2+}, to keep the soluble concentration close to its low physiological value, well below that of magnesium (Bagur et al., 2017 [48], Vormann, 2016 [49]). Magnesium was added as MgCl for the small anions where Cl^- affinity and competition would not cause problems (Cl^- and NO_3^-), as a salt complexed with the larger permeable anions where available, and otherwise as $Mg(OH)_2$. Internal solutions were titrated to pH 7.4 with TMA-OH, and HCO_3^- was bubbled with carbogen (5% CO_2 in O_2) until the start of the experiment to maintain a stable pH.

The osmotic concentration of solutions was measured with a Gonotec Osmomat (3000 basic) freezing point osmometer to ensure it was not significantly higher than in external solutions. External molar concentrations were adjusted with glucose to at least 5 mOSM above the internal levels if necessary to prevent osmotic gradients from causing the swelling and rupturing of cells. The swelling itself can cause volume-regulated anion channels like LRRC8A to open, which may lead to interference with experiments when measuring above 80 mV (Osei-Owusu et al., 2018 [50]). In addition to measuring and adjusting the osmotic concentration, limitations to the applied voltages avoided such problems. Measurement ranges were selected between 80 mV and larger negative values, typically −160 mV.

Construct	Experiment	Permeable anion	Perfusion $[Cl^-]$	Perfusion pH
WT	noise analysis	140 mM Cl^-	180 mM	5.0, 5.25, 5.5, 5.75, 6.0, 6.5, 7.0, 7.5, 8.2
WT	pH dependence (low Cl^-)	140 mM Cl^-	0 mM	4.6, 4.9, 5.1, 5.2, 5.6, 6.1, 6.6, 7.1*
WT	pH dependence (high Cl^-)	140 mM Cl^-	140 mM	5.0, 5.25, 5.5, 5.75, 6.0, 6.5, 7.0, 7.5
WT	Cl^- dependence	140 mM Cl^-	0, 5, 10, 20, 40, 80, 100, 140 mM	5.0
WT	pH application (low Cl^-)	140 mM Cl^-	0 mM	5.0 & 7.5
WT	pH application (high Cl^-)	140 mM Cl^-	140 mM	5.5 & 7.4
WT	Cl^- application (low Cl^-)	140 mM Cl^-	0 & 40 mM	5.0
WT	Cl^- application (high Cl^-)	140 mM Cl^-	0 & 140 mM	5.0

H120A	noise analysis	140 mM Cl^-	140 mM	5.0, 5.5, 6.0, 6.5, 7.0, 7.5
H120A	pH dependence (low Cl^-)	140 mM Cl^-	0 mM	4.6, 4.9, 5.1, 5.4, 5.6, 6.1, 6.6, 7.1*
H120A	pH dependence (high Cl^-)	140 mM Cl^-	140 mM	5.0, 5.25, 5.5, 5.75, 6.0, 6.5, 7.0, 7.5
H120A	Cl^- dependence	140 mM Cl^-	0, 5, 10, 20, 40, 90, 140 mM	5.5
H120A	pH application (low Cl^-)	140 mM Cl^-	0 mM	5.0 & 7.4
H120A	pH application (high Cl^-)	140 mM Cl^-	140 mM	5.0 & 7.5
H120A	Cl^- application (high Cl^-)	140 mM Cl^-	0 & 140 mM	5.0

Table 1: conditions for WT and H120A Cl^- current experiments with multiple solutions. *The pH of solutions marked with an asterisk (*) were re-measured after discovering that the pH meter had provided inaccurate readings.*

Construct	Experiment	Permeable anion	Perfusion [Cl^-]	Perfusion pH
WT	pH dependence	140 mM $Glut^-$	40 mM	5.0, 5.25, 5.5, 5.75, 6.0, 6.5, 7.0, 7.4
WT	Cl^- dependence	140 mM $Glut^-$	0, 5, 10, 20, 40, 80, 100 mM	5.5
WT	pH application	140 mM $Glut^-$	40 mM	5.0 & 7.4
WT	Cl^- application (low Cl^-)	140 mM $Glut^-$	0 & 40 mM	5.0
WT	Cl^- application (high Cl^-)	140 mM $Glut^-$	0 & 140 mM	5.5
WT	pH dependence	140 mM Asp^-	40 mM	5.0, 5.25, 5.5, 5.75, 6.0, 6.5, 7.0, 7.5
WT	Cl^- dependence	140 mM Asp^-	0, 5, 10, 20, 40, 80, 100, 140 mM	5.5
WT	pH application	140 mM Asp^-	40 mM	5.0 & 7.4
WT	Cl^- application (low Cl^-)	140 mM Asp^-	0 & 40 mM	5.5

Table 2: conditions for WT $Glut^-$ and Asp^- current experiments with multiple solutions.

2.5 Anion current blocking with Rose Bengal

Rose Bengal (RB) is a known VGLUT blocker that was previously validated as high-affinity and non-competitive, at least for vesicular $Glut^-$ transport (Ogita et al., 2008 [51]). For a pharmacological test for possible contributions of background signals to the measured current, amplitudes of RB were applied at various concentrations to cells transfected with $VGLUT1_{PM}$, dialysed with solutions containing $Glut^-$, Cl^-, NO_3^-, Asp^-, $Gluc^-$, HCO_3^-, or MES^{55}. Measurements were compared at pH 5.5, 40 mM Cl^-, and −160 mV, and blocking affinity was determined by fitting the data to the Michaelis-Menten equation. Cl^- and NO_3^-, small anions with high conductance, were blocked most efficiently with 94.1 ± 2.2% (mean

and 95% confidence interval; K_M = 123) and 89.1 ± 6.2% (K_M = 151), respectively, by the highest concentration of 1600 nM RB (Figure 6, top). In contrast, the larger organic substrates of HCO_3^- (82.2 ± 4.9, K_M = 411), $Glut^-$ (78.7 ± 4.2, K_M = 286), Asp^- (78.6 ± 6.7, K_M = 466), MES^- (75.9 ± 4.0, K_M = 459), and $Gluc^-$ (71.6 ± 15.3%, K_M = 687) saw reduced but still significant blocking. The remaining current at 1600 nM RB was found to be indistinguishable from the background for all tested anions, with p-values of 0.92, 0.06, 0.57, 0.36, 0.30, 0.65, and 0.09, respectively (Figure 6, bottom). This demonstrates that the observed currents are mediated by $VGLUT1_{PM}$.

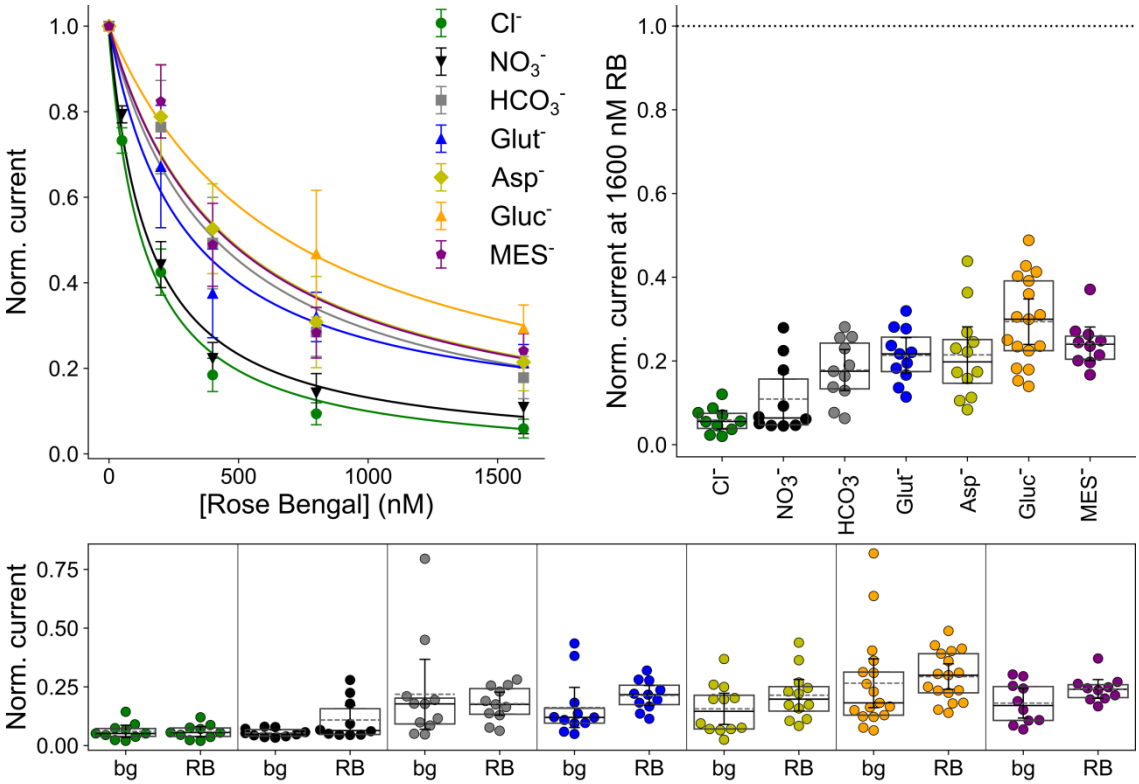

Figure 6: Rose Bengal blocking $VGLUT1_{PM}$ transport of various anions. *Relative blocking for various anions conducted at pH 5.5 and −160 mV, depicted with Michaelis-Menten fits of concentration dependence (left), cellular distribution of current at 1600 nM (right), and comparison to unblocked background current at pH 7.4 (bottom). Boxplot medians are shown as solid lines and means as dashed lines. $Gluc^-$ measurements of low but nonzero concentrations of RB were inconsistent and therefore omitted, along with a maximum concentration of 3200 nM RB that was consistent with other results but only measured for $Gluc^-$.*

2.6 Fast application

Techniques to track biochemical interactions in response to changes in solutes, with a time resolution of a few milliseconds, have been used since the early 90s (Cannell et al., 1991 [52]). Among the methods developed during this time is the use of piezoelectric actuators to move the solution interface of continuous perfusion flow around a cell (Smith et al., 1991 [53]). For an adaptation of this strategy, standard patch clamp perfusion was routed through

glass tubing attached to the moving part of the piezoelectric actuator. Multiple sets of devices were used, based on either a PiezoMove P-601.30L or P-840.40 actuator (Physik Instrumente, Karlsruhe, Germany). Their movement was controlled via an MXPZT controller (Siskiyou Corporation, Grants Pass, Oregon, USA) or PI E-836 Piezo Driver in combination with a USBPGF-S1 Instrumentation Amplifier Low Pass Filter to smoothen the signal and reduce vibration (Alligator Technologies, Charlottesville, Virginia, USA), respectively. Piezoelectric actuators were mounted onto a manual manipulator, which in turn was attached to the vibration isolation table. Actuators were connected to the EPC10 amplifier and controlled using HEKA PatchMaster software.

2.6.1 Perfusion pipettes

Glass dual-channel capillaries (2.0 OD × 0.3 Wall × 0.22 Septum × 150L mm, Harvard Apparatus, Holliston, Massachusetts, USA) were pulled into pipettes using a Sutter Instruments Flaming/Brown micropipette puller model P-1000. Since initial pipettes had narrow tips, they were trimmed using a diamond-tipped glass cutter to ensure they were larger than cells. These tips were subsequently heated using the clamp of a List Medical L/M-3P-A vertical pipette puller with a custom filament and manually bent to an angle of approximately 45 degrees (Figure 7). This enables horizontal solution flow from both channels onto cells in the same focal plane.

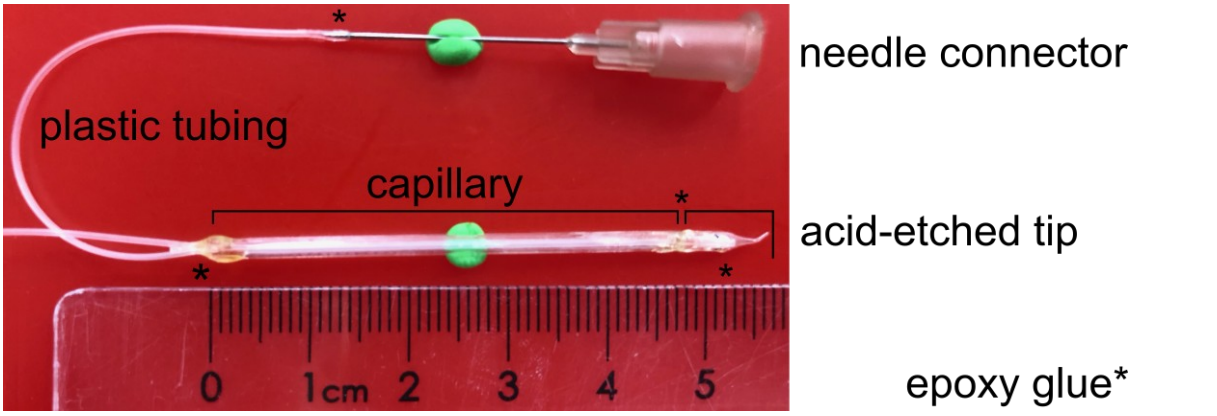

Figure 7: composition of dual-channel fast application perfusion pipettes. *Plastic tubing runs from the needle connector through the capillary and into the pipette tip. All parts are connected with epoxy glue and green plasticine was used to temporarily align the ensemble.*

Each tip was acid-etched to make the glass septum in between its channels thinner and reduce turbulence upon solution outflow. To achieve this, around 1 cm of the tip was separated from the capillary using the aforementioned glass cutter and inserted into a short rubber tube, which was connected to a polypropylene syringe. Hydrofluoric acid was gently flushed from the syringe and through the tip (handling of this chemical was exclusively performed by a qualified employee of the Mechanical Workshop of the Forschungszentrum Jülich) for 0.5 to 5 minutes, depending on the width of the glass tip. The finished glasswork was thoroughly water-rinsed with the same combination of tube and syringe, with an inward

flow to reduce the chance of aquatic and rubber debris from the tubing entering the tip. Fine plastic tubing (0.61 OD × 0.28 ID mm, PE-10, Warner Instruments, Hamden, Connecticut, USA) was sealed into both channels of the tip with epoxy glue (UHU Plus 2-K-Epoxidkleber Endfest 300, UHU GmbH & Co. KG, Bühl, Germany), injected into the capillary end with a syringe and needle (Ø 0.45 × 25 mm, Braun 100 Sterican, B. Braun SE, Melsungen, Germany) along the outside of the tubing. The ends of these tubes were threaded through a longer and untreated piece of dual-channel glass, which was then connected to the glass tip with more epoxy glue. The same type of needle was inserted into each end of the tubing and reinforced with a drop of epoxy glue so its plastic end can connect to standard perfusion tubes.

2.6.2 Protocols

To rule out directional bias in piezoelectric movement, the side of the perfusion pipette to which each solution was connected was alternated over different days of measurement. Small differences in the positioning of measured cells and perfusion flow can affect the timing of the response, so cells were manually aligned before individual normalisation to the highest steady-state value. Since the signal-to-noise ratio tends to be low for small and positive voltage values, only those obtained at more negative voltages (between −100 mV and −160 mV) were selected for analysis.

Aside from voltage, $[Cl^-]$ and pH are the most important factors affecting the current output of VGLUT1. Different concentrations were used, changing one variable at a time. Each dataset was measured in two directions to test and control for asymmetry. Measurements are shown with the low-current solution both at the start and at the end of a voltage sweep, applying and subsequently removing an activating condition in what was termed the *forward direction*. The *reverse direction* measurement has the activating solution both at the start and at the end, with a deactivating solution in the middle. No major asymmetries related to gating were found in the data presented here, but similar numbers of cells for activations and deactivations from both directions were combined just in case. All solution change segments were individually normalised to their maxima, and results are always depicted in the forward direction, activation followed by deactivation.

Measurements obtained with these protocols were fitted with exponential functions, in all cases requiring one or two exponents to be described well. To determine which is more appropriate, nonlinear regression was used on the selected voltages for the activation and deactivation of all datasets. The quality of monoexponential fits was compared to that of a biexponential function, the latter with typical biexponential starting parameters. Based on the least squares difference and an F-test, only data that was found significantly better

represented by the sum of two exponential functions (with a p-value of 0.05) is represented with both exponential components and the amplitude ratio of the slowest.

2.6.3 Time resolution

To determine whether this solution exchange is fast enough for reliable time resolution, controls were occasionally recorded after completing fast application measurements. The cell was blown off the pipette, and moderate positive pressure was maintained while a testing protocol was run. This applies the same voltage amplitude to activate the piezoelectric manipulator but applies no voltage to the patch pipette. Normally obscured by the cell, the current of open pipette solution exchange can be recorded to reveal the rise time for the new environment. This relies on the difference in ion mobility between the solutions. Measurements with a stable baseline and straight horizontal current segments were selected over multiple years. With the difference between low and high current as 0 and 100%, solution exchange time was calculated from the number of data points between the first value above 10% and the last value below 90%. Since each measurement performed two back-and-forth exchanges, the on-off pair with the best resolution was chosen and averaged for each recording. These measurements were pooled, and an exchange time of 0.87 ± 0.2 ms (mean and 95% confidence interval) was calculated, with high-end extremes being an additional 1–2 milliseconds slower (Figure 8A).

The fastest time constant, determined by fitting either a single or double exponential function to the most negative voltage, was determined for all piezo-based experiments. These values were compared to the aforementioned time resolution. With a minimum of 3.7 ms, even the fastest cellular response was slower than the worst open pipette exchange time (Figure 8B). Not just the fastest processes, but also the total duration of $VGLUT1_{PM}$ activation and deactivation continue well beyond the approximately 1 ms rise time. There appears to be a sufficiently large part of the time course available for analysis outside any region of uncertainty for all experiments.

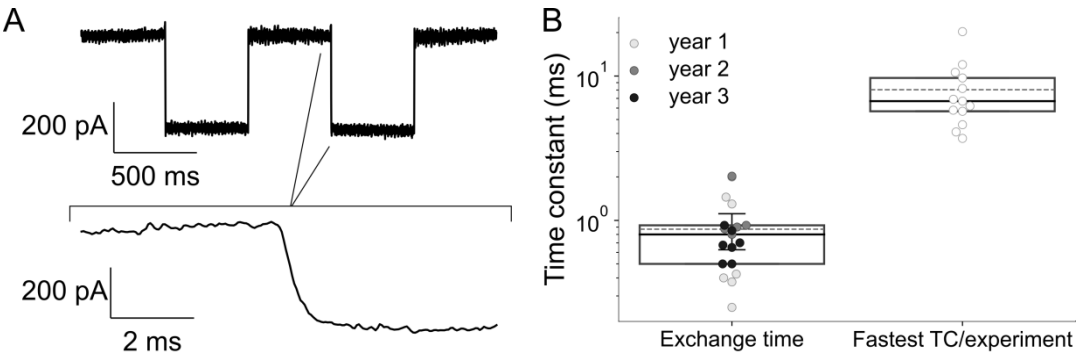

Figure 8: fast application time resolution. *Representative recording of the protocol used to test open pipette solution exchange time, typically between different [Cl^-] (A), and calculated exchange times collected across several years compared to the fastest rate of all solution exchange experiments (B). Exchange time error bars represent a 95% confidence interval.*

2.7 Stationary noise analysis

The current recorded during patch clamp experiments is the sum of the unitary currents across all cell membrane channels that happen to be active or open at the time (Gray, 1999 [54]). To mathematically break macroscopic current down into its components and determine further characteristics, one has to make several assumptions. Firstly, the number of channels *N* is homogeneous with comparable unitary current i. Secondly, all channels are either conducting, with probability *p*, or not conducting. Lastly, each channel is independent of others in this characteristic (Ehrenstein et al., 1970 [55]). Based on these assumptions, measured current can be defined as

Equation 1 $$I = \mathrm{N} \bullet i \bullet p$$

With this representation, the variance of current through a channel σ^2_I can be understood as the sum of squared deviations from the mean for each possible combination of probability and deviation, where 1 − *p* is *q,* the closed probability (Sigworth, 1980 [56]):

Equation 2 $$\sigma^2_{\mathrm{I}} = p\,(i - ip)^2 + q\,(-ip)^2 = i^2pq$$

The cumulative variance σ^2 can be obtained by multiplying the previous equation with the number of channels in the system:

Equation 3 $$\sigma^2 = \mathrm{N}i^2pq$$

Equation 1 and Equation 3 can be combined into Equation 4, which shows that the variance as a function of current is described by a parabola. It has a value of 0 either when I is 0 (unitary current is 0 or all channels are closed) or when I is equal to $N \cdot i$ (all channels open to its unitary current), and a maximum when half of all channels are open (Alvarez et al., 2002 [57]).

Equation 4 $$\sigma^2 = iI - \frac{I^2}{N}$$

The parameters in Equation 4 can also be rearranged to produce a linear function. Unitary current i can now be extracted from the ratio of variance and current instead:

Equation 5 $$\frac{\sigma^2}{I} = i - \frac{I}{N}$$

The tips of patch clamp pipettes for noise analysis experiments were dipped into molten dental wax (Moyco Technologies) to cover them and reduce capacitance, and briefly re-polished to melt away excess wax. Through a variety of pH conditions, a range of current amplitudes was recorded at a high sampling rate of 100 kHz. The usual 2.9 kHz Bessel filter

was disabled during the measurements and the results were Bessel filtered at 99 kHz between acquisition and analysis instead. Since it cannot be guaranteed that the current of each cell reaches steady-state in time, any low relaxation of pre-steady-state gating was removed using an additional 200 Hz Butterworth high-pass filter. Analysis was performed on variance determined over the last 30 ms of data, after at least 70 ms of each sweep. Positive and small negative voltages were not used to maintain a good signal-to-noise ratio. Background noise was determined using the same procedure on the first 9 ms of data at 0 mV and subtracted.

2.8 Filter frequency analysis

The data used to determine single-channel current was filtered by Butterworth low-pass filters with increasing cut-off frequencies, from 99 to 80, 40, 20, 10, 8, 4, 2, and 1 kHz. Dividing 10^6 µs by a proposed open time gives *m,* the expected closing rate in μs^{-1}. Combined with an open probability of 0.24 based on earlier noise analysis (Kolen et al., 2023 [34]), *m* then allows for the calculation of a corresponding opening rate *n*:

Equation 6

$$n = \frac{m \bullet p}{1 - p}$$

A random number generator was used to produce 10 µs time steps for a sequence significantly longer than the open time, in this case having values in the lower hundreds of ms. Gating rates *m* and *n* can now be used to simulate a channel alternating between one open and one closed state (Alekov et al., 2009 [58]). This was done for a group of channels with an arbitrary population of 10^5, producing the same result as with ten times more channels. The collective variance of their opening can be summed up into a replica of the experimental current. The same Butterworth filter frequencies listed previously were applied to the last 100 ms steady-state of simulated noise. The effect of filtering on the remaining variance was compared to experimental values, and manual adjustment of the simulated closing rate found it matched empirical results when between 60 and 120 µs. A range of 15 evenly distributed values for *m* was created from 60 to 120 µs, and residual sums of squares (RSS) were calculated to determine which simulated open time fits the data best. The simulation was run ten times to assess simulation consistency and obtain a statistical measure of variance.

2.9 Kinetic modelling

Protein function was simulated using kinetic models, with each unique combination of protein conformation and ligand binding represented as a Markov state. Each connection between states represents a possibility for direct transition between them (Figure 9, left). This can consist of conformational change of the protein or the association and disassociation of

ligands. Such transitions describing binding events are dependent on the concentration of the substance binding to the protein. Where Markov models are typically calculated using probability, kinetic models use reaction rates (in s^{-1}) to describe transitions. This Markov property relies on two assumptions: that state-to-state transition rates are constant under identical conditions and that each resulting event is independent of past interactions and only determined by the current state (Sharpe et al., 2021 [59]).

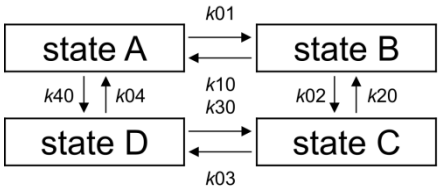

state A	-*k*01 -*k*40	+*k*10		+*k*04
state B	+*k*01	-*k*02 -*k*10	+*k*20	
state C		+*k*02	-*k*03 -*k*20	+*k*30
state D	+*k*40		+*k*03	-*k*04 -*k*30

Figure 9: hypothetical kinetic model and corresponding transition matrix. *Directional rate numbers are chosen arbitrarily, and full equations are omitted from the matrix for clarity. Any ligand binding rate, k0X according to the chosen convention, would additionally be multiplied by the concentration of this ligand for both its appearances in the matrix.*

Changes in state occupancy are computed via rate equations, each describing an interaction between two states, combined in a transition matrix (Figure 9, right). For any environmental condition, each row of the matrix represents all flows in and out of a state. The sum of all outgoing rates is placed within the diagonal of this matrix (the top left to bottom right), each vertically lined up with the same values as incoming rates for a column sum of 0. Solving this matrix of ins and outs as a series of algebraic equations provides the steady-state distribution towards which it converges under these conditions. When simulating current change over time, this method is used to generate a ground state matrix. This is used as a starting point for a second transition matrix describing the next set of conditions, for which the change in state distribution is calculated by solving the first-order ordinary differential equation for the experimental duration.

A hypothetical transition 1 from state A to state B is calculated as rate *k*01 with an exponential function, with the calculation for its dependence on voltage and temperature based on the Arrhenius equation:

Equation 7

$$k01 = k1 \bullet e^{z \bullet d \bullet V \bullet \frac{F}{R \bullet T}} \left(\bullet [ligand] \right)$$

For each pair of connected states, the rates describing transition in both directions are calculated using a total of four variables: *k*1, *k*2, *z*, and *d*. Transition A to B is described with *k*1 is the rate constant, *z* represents charge movement but can also be interpreted as gating charge or electrogeneity, and *d* is a symmetry factor equivalent to *α* or *β* in the Butler-Volmer equation (Björketun et al., 2013 [60]). V is the voltage across the cell membrane, and the rest of the equation consists of constants: *F* is the Faraday constant (96485.33 C · mol^{-1}), *R* is the gas constant (8.3144621 J · K^{-1} · mol^{-1}), and *T* is the temperature (295.15 K for 22°C). The

last remaining variable *k*2 is the rate constant from B to A, used to calculate rate *k*10 in the direction opposite to *k*01:

Equation 8 $$k10 = k2 \bullet e^{-z \bullet (1-d) \bullet V \bullet \frac{F}{R \bullet T}}$$

Its unique rate constant is multiplied by the inverse of *z* and the complement of *d*, but the other constants remain the same as in Equation 7. Rates describing ligand binding get multiplied by the concentration of that ligand to account for its availability, which modulates this rate. All rates describing ligand binding or transition to a conformation that allows for anion permeation are assigned *k*0*X* and *k*1 (as opposed to *kX*0 and *k*2) by convention.

2.9.1 Microscopic reversibility

Many dynamic systems that involve particles and can be described by equations exhibit time-reversible symmetry. While this principle does not extend to the macroscopic scale in a way humans can comprehend, being influenced by factors like entropy, it is generally true for the microscopic scale at which electrophysiology is applied. A relevant consequence of this is that, thermodynamically speaking, it is not possible for net cycling to occur in a system in a state of equilibrium: the rates of all processes must, on average, be equal to their inverse rate (Lewis, 1925 [61]). In practice, this means that the directional bias in the absence of a driving force must be zero. Using the principle of detailed balance, the kinetic application of microscopic reversibility, the reversing of time can be represented by a reversing of arrows in a kinetic scheme. Under detailed balance, the product of rates describing any cycle of the model must equal the product of the inverse (clockwise versus counterclockwise) path:

Equation 9 $$\frac{\Pi\, clockwise}{\Pi\, counterclockwise} = 1$$

This requirement can be fulfilled by dividing the model into interconnected cycles, where each rate must be included in at least one cycle. For each cycle, the equation is rearranged to isolate one rate from the fraction, and its value is calculated from the rest. Similarly, charge movement at equilibrium must be 0 when no net transport occurs, which is achieved by calculating one *z* variable from the sum of all others in a cycle:

Equation 10 $$\sum charge\ movement = 0$$

Where a kinetic cycle is capable of causing directional transport, and consequently the sum of charge movement through it does not equal zero in equilibrium, the value of this charge replaces 0 in the calculation. Each instance of VGLUT1 transporting 1 $Glut^-$ anion towards the reference electrode in exchange for 1 H^+ causes a combined charge movement of −2 *e* ($-H^+ + Glut^-$). Since Asp^- appears to be transported without meaningful coupling, uncoupled transport cycles are assigned a total charge movement of −1 *e*. When a state transition is

physiologically unlikely in a certain direction specifically, blocking it would interfere with the reversibility part of the detailed balance calculations in the model. Instead, such rate constants were limited in scale, unable to exceed 1 s^{-1} prior to modification by the membrane potential. This was applied to all transitions describing the opening of the anion channel of unprotonated VGLUT1. The same restriction was used for doubly protonated and $Glut^-$-bound VGLUT1, transitioning between inward and outward-facing conformations in either direction. Only $Glut^-$ transport requires this limitation to exhibit proton coupling in its transport cycles, so the rate constants were not restricted for Asp^-.

2.9.2 Data selection

Rates describing modelled transitions were estimated by fitting the model to experimental results, which include multiple stationary values such as overall open probability modulated by allosteric activation by H^+ or Cl^- (calculated as a fraction of relative current amplitude) and estimated channel open time (based on filter frequency analysis). Various time courses resulting from changes in V, pH, and $[Cl^-]$ were compared between experiments and the simulation for the duration of the measurement. The voltage across the membrane plays a role in the configuration of the protein, but jumping from (negative) potentials to 0 in experiments shows current permeation dropping effectively instantaneously. This happens before the protein itself can undergo changes in either conformation or ligand binding, which suggests that voltage also functions as a direct driving force (Figure 10A). Consequently, direct linking of measured current to simulated open probability was only possible for steady-state current modulated by $[Cl^-]$ and pH (Figure 10B). Maximum current, as either open probability or active transport amplitude, was normalised to the highest steady-state amplitude for each voltage sweep in both simulation and experimental data. To ensure a sufficient signal-to-noise ratio, only the four most negative voltages of each fast application experiment (and comparably negative voltages when measuring single solutions) were used for kinetic modelling.

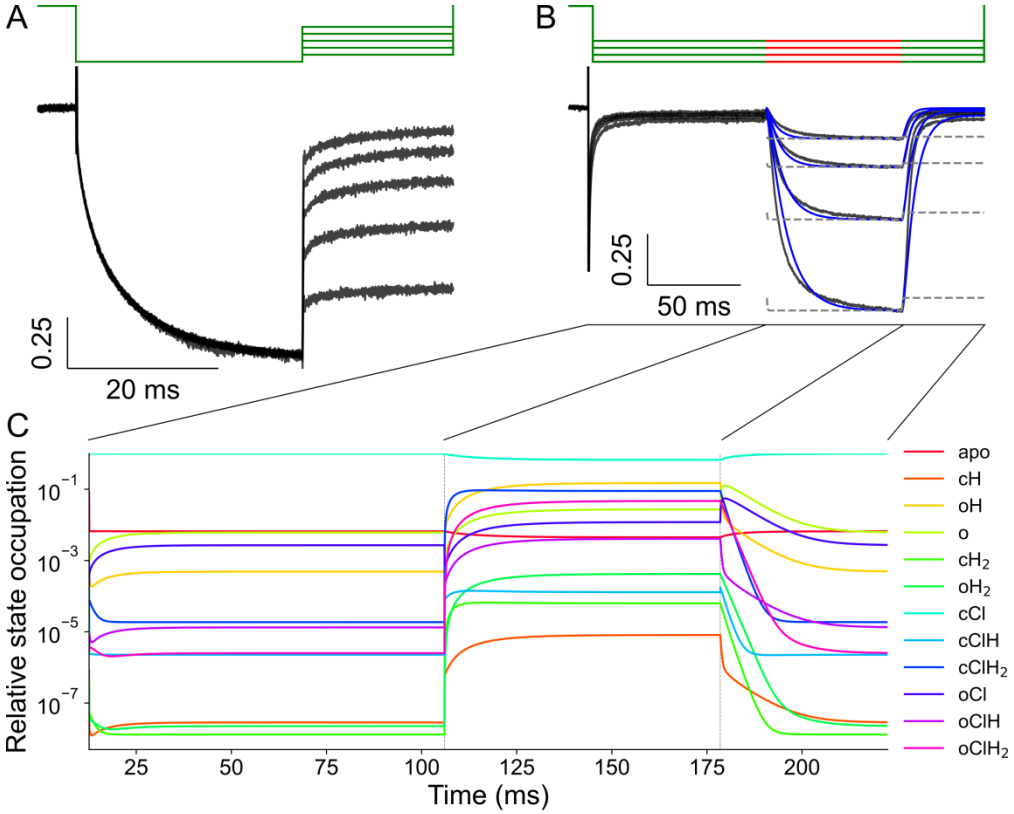

Figure 10: voltage as driving force, simulated pH jump optimisation, and state distribution. *A pair of experimental datasets for Cl^- current with 140 mM external Cl^- consisting of a negative voltage jump, followed by the functionally instantaneous change in V driving force and resulting current drop upon jumps to various more positive values (A), modelled current activation by pH 5.5 jump from pH 7.4 with the acidic condition in red, simulations with initial unoptimised parameter starting values in dashed grey and optimised parameters in blue (B), and simulated distribution of open and closed states for the pH jump (C). State names starting with "o" are open; others are closed.*

2.9.3 Current quantification

The set of calculated paths between transition matrices was used to quantify anion permeation, with different methods depending on the simulated mechanism. For the channel function of VGLUT1, the relative distribution of state occupancy in the transition matrix is used to calculate the fraction of open states (representing open probability) as the output value (Figure 10C). The active transport of individual $Glut^-$ and Asp^- anions is independent of a singular state property and instead based on transport cycles through an alternating access mechanism. Net transition flux between states, multiplied by the corresponding *z* value, provides current as the total charge movement through the model. In steady-state conditions, the simulated value is mostly determined by the charge offset used in the detailed balance calculations of the transport cycles. Ion permeation via coupled transport was calculated as half of the simulated value because its current output is calculated as −2 *e*, while uncoupled transport output (as is expected for Asp^-) is already represented in anions per second.

The various models were trained to mimic the experimentally determined Cl^- channel open probability or $Glut^-$ transport rate, with the value for Asp^- transport calculated from its relative current normalised by fluorescence (Kolen et al., 2023 [34]). This ensures the kinetic model produces realistic and physiologically relevant currents. The number of channels, open time, and unitary current are assumed to be irrelevant or independent of all modelled factors.

2.9.4 Optimisation

At the first use of a kinetic model, the starting values of rate constants are chosen to have intermediate amplitudes and be as homogeneous as possible to allow modification in either direction with minimal initial bias. They are then subjected to a population-based optimisation procedure inspired by biological evolution. For this, they are continuously varied randomly using an adaptation of the Distributed Evolutionary Algorithms in Python (DEAP) software package (Fortin et al., 2012 [62]). An initial parameter set is used as a parent to generate a population of at least 50 clones (Figure 11A), with a bad fit as seen in Figure 10B, as dashed grey lines. All these individuals have a chance for each of their parameters (excluding those calculated from others to maintain detailed balance) to be mutated (p = 0.5) by a random amount. Mutation of each set of parameters is based on random number generation, with the mean amplitude set as (a fraction of) the standard deviation of a normal distribution centred on the initial value. Additionally, with the hypothetical pairing of each two consecutive individuals in the population, randomly selected pairs may mate (p = 0.7). Instead of swapping alleles within chromosome pairs, as is the case in the biological process after which it was named, the individuals trade their values for a specific variable. In mating parameter set pairs, this occurs separately for a random selection of variables.

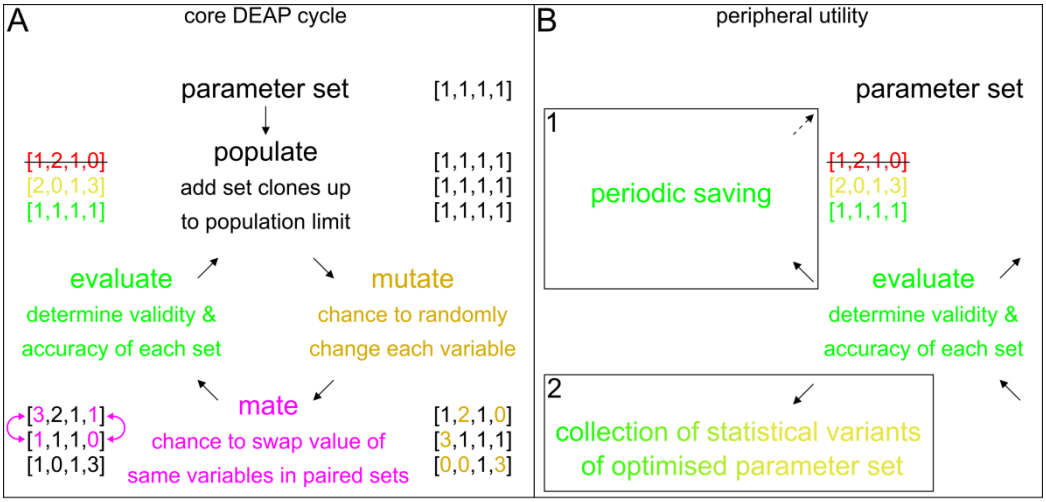

Figure 11: schematic representation of DEAP software package applications. *Core uses of DEAP applied to each cycle of parameter optimisation (A) and post-evaluation functions that are not applied in every cycle (B). The best individual is saved as a potential optimised set or restarting point whenever a threshold of new generations is passed (1). Once a parameter set has been deemed optimised, all valid sets can be saved as a measure of statistical variance (2).*

Rate constants are limited to 10^5 s^{-1} for conformational changes and to 5×10^9 for the binding and unbinding of ligands, all positive. Charge movement can range from −1 to +1, and symmetry from 0 to 1. The mutation of these parameters by DEAP can cause invalid values when they fall outside these bounds, which will demarcate the individual as unfit and remove it from the population. The fitness of each individual in the population is further evaluated via the cumulative difference between its simulated behaviour and experimental data. Comparisons are made for a combination of various calculated values and experimental time courses, mostly as RSS to increase the importance of larger deviations. Different points of comparison are split into different categories, such as the ligand dependence of steady-state current or the time courses of separate experiments, to allow their evaluation to be balanced with separate calculations and weight multipliers. Weights were regularly adjusted manually to ensure sufficient driving force to improve the different points of comparison. Individuals with parameters that replicate experimental data better are more likely to get cloned via a tournament-style selection by fitness.

In order to determine preferred channel opening pathways, the kinetic transition rates describing fluxes into states were converted into probabilities describing the departure from states. The reactive flux module of the Deeptime Python library was then able to calculate the relative probability distribution based on transition path theory (Metzner, 2009 [63]). Activation pathways were described starting from the *apo* state to any conductive state, and deactivation pathways from the two most common open states (oH or $oClH_2$) to either of the two unprotonated closed states (*apo* and cCl).

2.10 Statistical analysis

To make statistical analysis of modelled rates possible, two measures of variance and confidence were generated for each application of a model. The experimental data used for evaluation was uncoupled from weights and instead normalised for several points of comparison. Calculated values were used as one point of comparison each for pK_a values and either open probabilities and open times for the modelled Cl^- channel or transport rates for modelled active transport, and all dependency curves served as separate comparisons. Each individual experiment, including all different voltage sweeps and also distinct condition change segments for most, was combined into one point of comparison.

As the first measure of variance, relative RSS was determined for a range of values centred on the optimised value of each parameter. For *z* and *d* variables, the distance between the upper and lower bound was split at the optimised value, and each side was divided into 25 equal steps for a total of 50 new values. For rate constants, a logarithmic range was generated between $1/100^{th}$ of this rate and 100 times this rate for 25 logarithmically equidistant steps in each direction and a total of 50 new values. The point of comparison with

the largest deviation from baseline variance for each variable was compared to a goodness-of-fit limit. This was placed at 150% of the RSS as a sum of the squared difference between each point of data and its simulated equivalent. This makes sure the variants are only considered viable if they perform reasonably well for each point of comparison. If the RSS of compared parameters did not connect, the tested value range could be extended. For the kinetic model representing Cl^- current for the WT and H120A mutant, several symmetry parameters did not have enough impact to significantly affect goodness of fit. Where a value affected RSS for only one construct, its value was copied to the other. Where neither had a value sharply defined by RSS, both were locked at 0.5 to represent a lack of meaningful asymmetry.

Since not all model characteristics are easily judged from a single rate, the second measure of variance was generated by varying parameter sets collectively. A modified version of the aforementioned default DEAP cycle was used to generate set-wise rate variants through exploratory mutation (Figure 11B-2). All individuals were stored if they remained below 125% of the RSS of each point of comparison calculated from the initial parameter set. Unlike the previous method, having both binding and unbinding rates for each protonation directly provides variance for simulated pK_a and K_D. Optimised parameter sets were mutated until over 10,000 individuals were collected. The sigma controlling the mutation size was set to 1% of the optimised parameter value for applications of the Cl^- channel model. Aside from the aforementioned locked symmetry, which was found to not meaningfully affect RSS, there were at least 3000 variants generated for each parameter for both applications of the modelled Cl^- channel. To account for the increased constraint of the larger model for $Glut^-$ and Asp^-, its sigma was lowered to steps of 0.1% of the allowed variable range, or 10 s^{-1}. This allowed mutation to generate at least 982 variants per parameter, distributed over 20,000 sets, after eliminating sets that did not contribute to the variation of protonation parameters. The amplitudes of modelled z, d, and rate constant variables generated during exploratory mutation are given as medians, with the total range as a confidence interval. Compared values are deemed distinct if their values do not overlap in neither of the two variance metrics.

Patch clamp measurements used to determine numerical characteristics for various $VGLUT1_{PM}$ characteristics were subjected to nonlinear regression applied to individual cells in a bootstrapping protocol with a global fit and sampling of 1000: single and double exponential functions were used for the time constants of activation and deactivation, the Michaelis-Menten equation with an additional linear offset to allow for current in the absence of external Cl^- for K_M values, and the Hill equation for pK_M because the Michaelis-Menten equation was unable to consistently fit acid saturation. The K_M of $Glut^-$ and Asp^- was

determined with a single fit to concentration means because cells measured at few solutions made bootstrapping unreliable. Statistical analysis between bootstrapped values was performed using two-tailed bootstrap hypothesis testing with a sampling of 10,000. Comparisons between a group of individual cellular fits and a value determined by fitting a function to means directly, as was applied to the K_M between Cl^- current and $Glut^-$ or Asp^- current, were done with one-sample Wilcoxon signed rank tests to avoid issues with normality.

3. Results

VGLUTs transport various anions, primarily out of the cytosol, with mechanisms that interfere with one another. Small amounts of luminal Cl^- amplify active $Glut^-$ transport, but higher [Cl^-] either restricts or competes with it, while cytosolic $Glut^-$ alters the gating of the Cl^- channel by impeding closure (Kolen et al., 2023 [34]). To separate the different conductive properties of $VGLUT1_{PM}$, the internal solutions that substitute the cytosol were made only with Cl^-, $Glut^-$, or Asp^-. For all experiments that involve active transport, [Cl^-] was limited to 40 mM, the value that elicited the maximum outward $Glut^-$ transport (Kolen et al., 2023 [34]). Negative voltages help to restrict currents to those leaving the cytosol, as the perfusion solutions contain no cations that are known to pass through VGLUT1. This strategy of controlling the voltage and the solute distribution on both sides of the membrane ensures that measured currents properly represent the anion of interest.

3.1 VGLUT1 Cl^- currents increase with negative voltage and with external Cl^- and H^+

The conductive properties of VGLUTs appear to be primarily modulated by voltage and [Cl^-], as well as the external [H^+]. The aggregation of positively charged amino acids in their pore or active site allows for interactions with and transport of a wide range of anions (Figure 3). Whole-cell voltage patch clamp was used to quantify and characterise passive transport through the Cl^- channel of a modified rat VGLUT1 ($VGLUT1_{PM}$), where the N- and C-terminal targeting signals were neutralised to enable sufficient expression in the plasma membrane of HEK293T cells.

Negative voltage steps from 0 towards −160 mV strongly and exponentially increase the current of $VGLUT1_{PM}$, unlike positive steps up to 60 mV (Figure 12A). Allosteric Cl^- increases current, and this effect starts to plateau around 140 mM. Bootstrapped nonlinear regression global fit with a sampling of 1000 and the Michaelis-Menten equation, with an offset enabling nonzero baseline current, provides an apparent K_M of 28.3 ± 0.7 (mean and 95% confidence interval) for the WT construct (Figure 12B). Compared to 140 mM, approximately 20% of the current amplitude remains during perfusion without Cl^-.

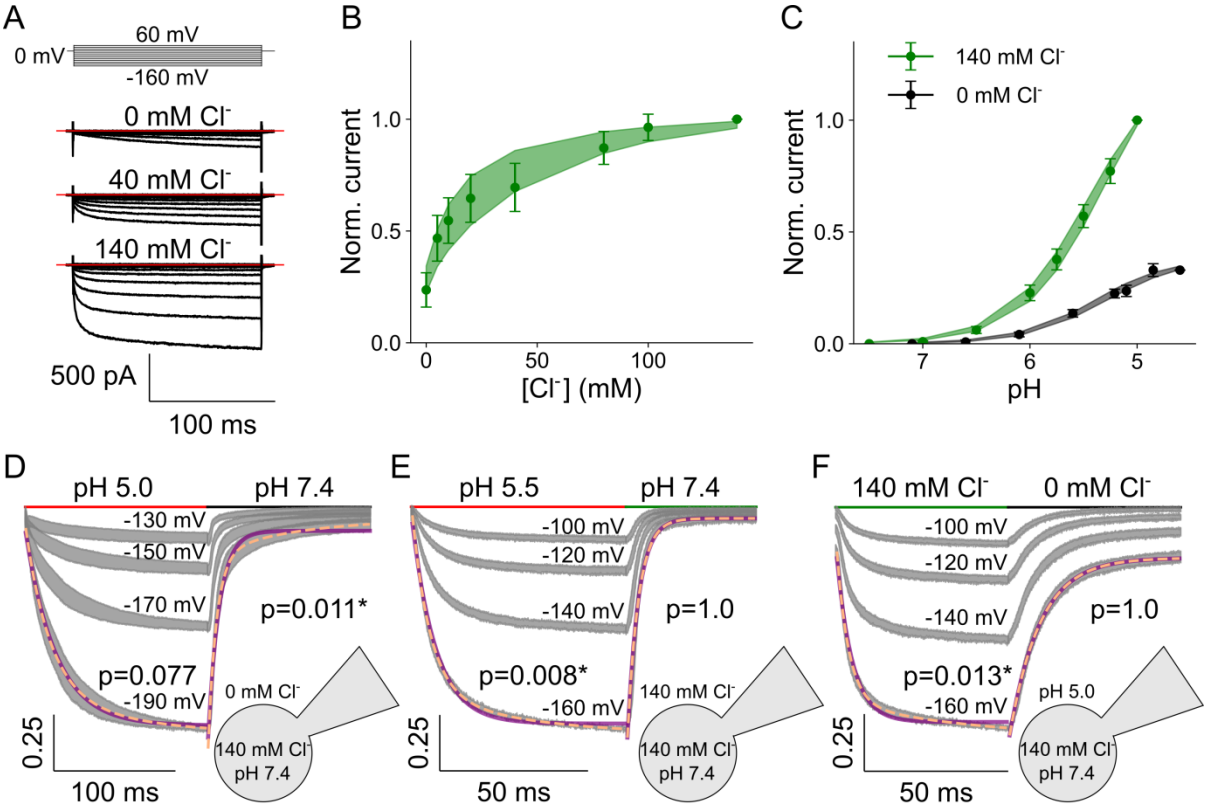

Figure 12: WT VGLUT1$_{PM}$ Cl^- current modulated by voltage, external pH, and [Cl^-]. *Representative recording depicting voltage steps at pH 5.5 and various external [Cl^-] (A), steady-state current dependence on external [Cl^-] up to 140 mM (B, −160 mV and pH 5.0, n = 11), and steady-state current dependence on pH (C, −160 mV, no external Cl^- in black with n = 10 and 140 mM Cl^- in green with n = 11), and current response to fast solution exchange during pH jumps without external Cl^- (D, n = 11), pH jumps with 140 mM external Cl^- (E, n = 12), or [Cl^-] jumps at pH 5.0 (F, n = 12) at continuous voltages. Data is shown as mean ± 95% confidence interval; p-values indicate whether the maximum current trace is described significantly better with a double (dashed orange) rather than a single (purple line) exponential function.*

Dependence on external pH was measured separately for both the aforementioned maximum and minimum concentrations of Cl^-. The results were normalised and scaled to the relative current obtained from the Cl^- dependence at pH 5.0. Both show negligible current at pH 7.4 and above but a sharp increase when the pH drops, with a saturation point somewhere below 5.0. Bootstrapped global fit with the Hill equation (to better capture the minor saturation) and a sampling of 1000 provides a similar apparent pK_M, with a value of 5.3 ± 0.003 with 0 mM Cl^- and 5.4 ± 0.003 with 140 mM Cl^- (p = 0.083). This should be taken as a rough estimate since an exact pK_a definitionally requires equilibrium conditions and is difficult to establish within this pH range, which is limited by available cell lines and biological buffer systems (see discussion). Gating induced by piezo-driven solution change shows monoexponential activation by Cl^--free acidification followed by biexponential deactivation (Figure 12D), biexponential activation and monoexponential deactivation with similar pH jumps in the presence of external Cl^- (Figure 12E), and biexponential activation when this Cl^- itself is introduced followed by monoexponential deactivation (Figure 12F). The result of

statistical testing regarding the number of exponents in fast application experiments is provided in Table 4-S.

3.2 External Cl^- and Br^-, but not I^-, activate VGLUT1 Cl^- and $Glut^-$ current

As shown previously in Figure 12, Cl^- currents through $VGLUT1_{PM}$ increase with the [Cl^-] in the destination environment. This allosteric effect is a known trait of VGLUTs and varies between different activating anions (Kolen et al., 2023 [34], Chang et al., 2018 [64]). As a member of the halogen group, there are several elemental ions with characteristics similar to those of Cl^-. Of these, only fluoride has a smaller atomic radius (133 pm), while bromide (196 pm) and iodide (219 pm) are larger than Cl^- with 181 pm (Slater, 1964 [65]). For each of the latter 3, cells were perfused with these halogens to quantify the allosteric activation of Cl^- and $Glut^-$ currents (Figure 13). The left graph additionally provides a further visual representation of the current-voltage relationship shown in Figure 12A, while the right graph does the same for $Glut^-$ in Figure 33A.

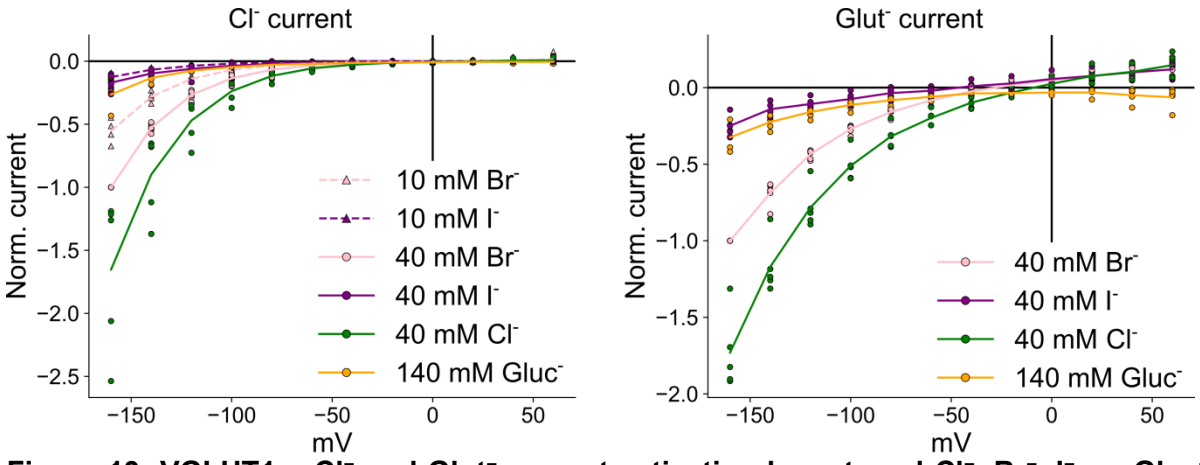

Figure 13: $VGLUT1_{PM}$ Cl^- and $Glut^-$ current activation by external Cl^-, Br^-, I^-, or $Gluc^-$. *The current of both permeable anions is normalised to corresponding measurements perfused with 40 mM of Br^-, and shows the mean as a line over individual cell measurements for Cl^- (4 × 10 mM Br^-, 4 × 10 mM I^-, 9 × 40 mM Br^-, 9 × 40 mM I^-, 4 × 40 mM Cl^-, and 5 × 140 mM $Gluc^-$) and $Glut^-$ (6 × 40 mM Br^-, 5 × 40 mM I^-, 5 × 40 mM Cl^-, and 5 × 140 mM $Gluc^-$). Where available, 10 mM concentrations of the tested halogen are shown as triangular markers and dashed lines.*

Halogen solutions were made in concentrations of either 10 or 40 mM, with $Gluc^-$ added for a total anion concentration of 140 mM. A solution with no halogens and only $Gluc^-$ was used as a control, representing a minimal allosteric activation that was indistinguishable to that provided by 40 mM I^- for currents of both Cl^- and $Glut^-$ ($p = 0.46$ and $p = 0.41$, respectively). Table 3 lists the quantified activation with the allosteric effect of Cl^- set to 100% for both anion currents. As the most similar to Cl^-, Br^- provides a consistent concentration-dependent activation to the current of both Cl^- and $Glut^-$ ($p = 0.003$ and $p = 0.037$, respectively, at 40 mM); 10 mM is not enough to activate Cl^- current more than the $Gluc^-$ control ($p = 0.081$).

Since I^- is larger than Br^- and Cl^-, its lack of current activating properties suggests that its increased size prevents it from accessing the binding site used by the other tested halogens. This finding touches base with earlier reports of similar allosteric activation of $Glut^-$ uptake, especially by VGLUT2 (Eriksen et al., 2016 [44]). Although 40 mM Br^- consistently elicited a smaller current increase than Cl^- in these measurements, the difference was not statistically significant at this sample size ($p = 0.32$ for Cl^- and 0.41 for $Glut^-$).

Halogen in perfusion	Relative activation of Cl^- current	Variance	Relative activation of $Glut^-$ current	Variance
40 mM Cl^-	(100%)	77%	(100%)	79%
40 mM Br^-	67%	27%	70%	47%
10 mM Br^-	42%	31%	N/A	N/A
40 mM I^-	12%	6%	14%	10%
10 mM I^-	11%	12%	N/A	N/A
140 mM $Gluc^-$	17%	17%	19%	15%

Table 3: quantified allosteric activation of Cl^- and $Glut^-$ current by various halogens. *Allosteric effects were measured separately for currents of Cl^- and $Glut^-$ and are shown with a 95% confidence interval as a measure for variance. Activation was calculated relative to the allosteric effect of Cl^-, all with a sample size as given in Figure 13. Shown [anion] are in combination with $Gluc^-$. "N/A" signifies that current activation and variance were not measured at this concentration.*

3.3 H120A VGLUT1 does not affect steady-state voltage dependence or rectification

Histidine H120 of VGLUT1 is located within the outward-facing side of the protein. Outward-facing conformations give it a prominent spot in the cavity, from where it is easily accessible and able to interact with the various ions involved in VGLUT transport (Figure 14). The imidazole group of the histidine, at the end of its side chain and reaching towards the centre of the channel, has two non-adjacent nitrogen atoms that share electrons along an aromatic ring with three carbon atoms. This makes histidine a protonatable residue with a pK_a of approximately 6. Histidines in the active site of VGLUTs have both their imidazole nitrogens protonated most of the time and consequently a positive average charge since the vesicular lumen reportedly has a pH lower than the pK_a of histidine (Miesenböck, 1998 [27]). This protonated charge makes it a likely candidate for interactions with anions like Cl^- or $Glut^-$ during transport processes within the protein (Li et al., 2020 [24]).

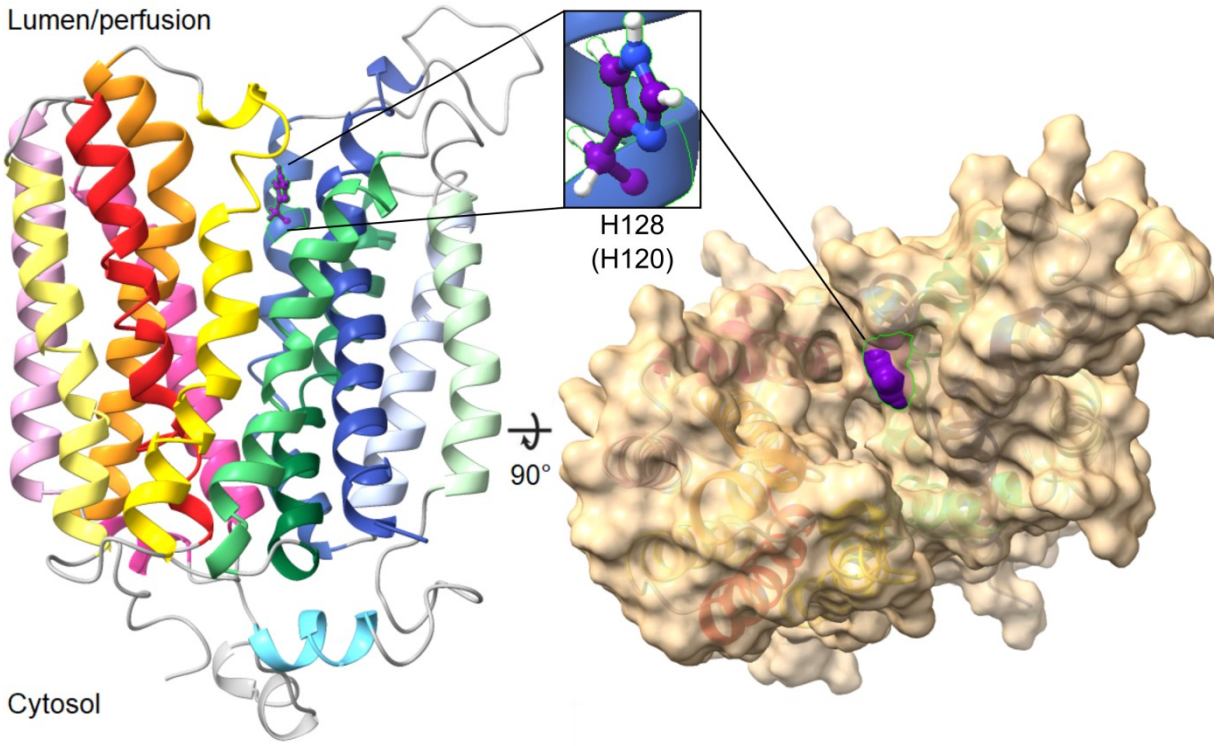

Figure 14: structural location of H128 in VGLUT2, equivalent to H120 in VGLUT1. *Protein in ribbon side view with histidine 128 in purple stick-and-ball representation on the left, a more detailed zoom-in of the histidine (bottom purple carbon connects to the helix backbone ribbon, nitrogens in blue) in the centre, and topside view of protein surface with the residue in sphere representation on the right.*

Testing this type of chemical interaction with individual amino acids often makes use of the properties of alanine. Its side chain of a single uncharged methyl group makes it the most chemically neutral amino acid and a good baseline. Whereas similarly sized proline and glycine amino acids can disrupt secondary protein structure with their unique shapes, alanine is the simplest and smallest amino acid with a typical backbone structure (Imai et al., 2005 [66]). Its small hydrophobic methyl group limits steric hindrance and negates both attractive and repulsive electrostatic interactions, consequently having an intermediate interaction with water. H120A VGLUT2 has previously been compared to WT VGLUT2, reconstituted in proteoliposomes *in vitro*, and was shown to reduce $Glut^-$ uptake to approximately 20% while Na^+-dependent P_i transport was not meaningfully altered (Juge et al., 2006 [25]). This loss of function hints at an important role *in vivo* that is centred on $Glut^-$ transport and may involve the uncoupling of $Glut^-$-proton exchange because a direct correlation between pH gradient and reversal potential is only seen in WT VGLUT1 (Kolen et al., 2023 [34]).

The rectification of a current is defined by its directional preference for positive charge conduction. Patch clamp measurements of $VGLUT1_{PM}$ under various voltages revealed a tendency for the cellular export of Cl^- and other anions, with respect to an external reference electrode, which qualifies this transport as inwardly rectifying. Although the membrane potential is often considered the main driving force behind VGLUT function (Naito et al., 1985

[28], Hnasko et al., 2010 [67]), a comparison of steady-state Cl^- currents across different voltages between H120A and WT $VGLUT1_{PM}$ does not show significant differences between these constructs. Peak amplitudes seem similar or even a bit larger for H120A under standard conditions, with the mutant slightly less stable with more noise at small currents near 0 mV and in the absence of external Cl^-. The current-voltage behaviour for both constructs overlaps, which indicates that the inward rectification produced by the WT is unaffected by this mutation.

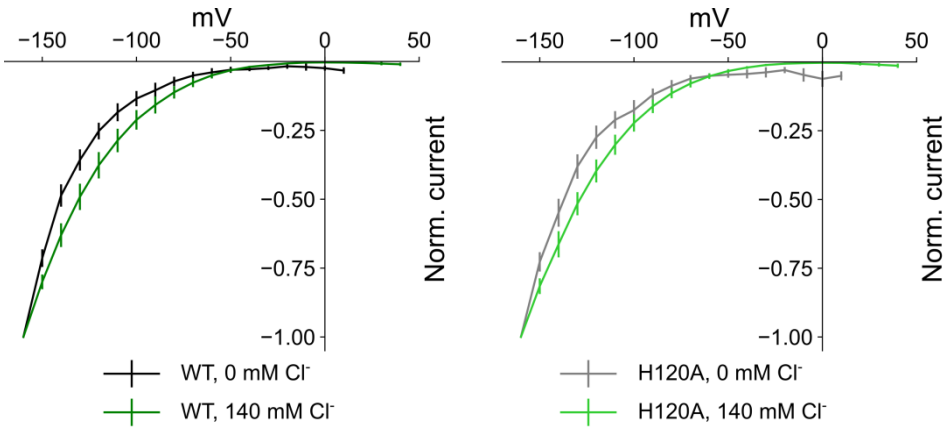

Figure 15: WT $VGLUT1_{PM}$ and H120A, Cl^- current-voltage relationship modulated by Cl^-. *Leak currents were subtracted for all data, either by recording it using the built-in P/n leak subtraction function of HEKA PatchMaster (as P/4) or by manually subtracting the corresponding current at pH 7.4. While measurements without external Cl^- (n = 11 for the WT, n = 10 for H120A) reduced current to roughly a quarter in both constructs compared to 140 mM (n = 10 for the WT, n = 11 for H120A), their current is depicted normalised to the same value for both [Cl^-] to allow easier comparison. Error bars represent a 95% confidence interval.*

3.4 H120A slows down VGLUT1 activation and deactivation, except those induced by Cl^--free changes in pH

While H120A is similar to the WT in steady-state current and voltage modulation, the mutation of this histidine elicits clear differences in time-based gating behaviour. Figure 16 depicts various experiments with both constructs, aligned to highlight differences.

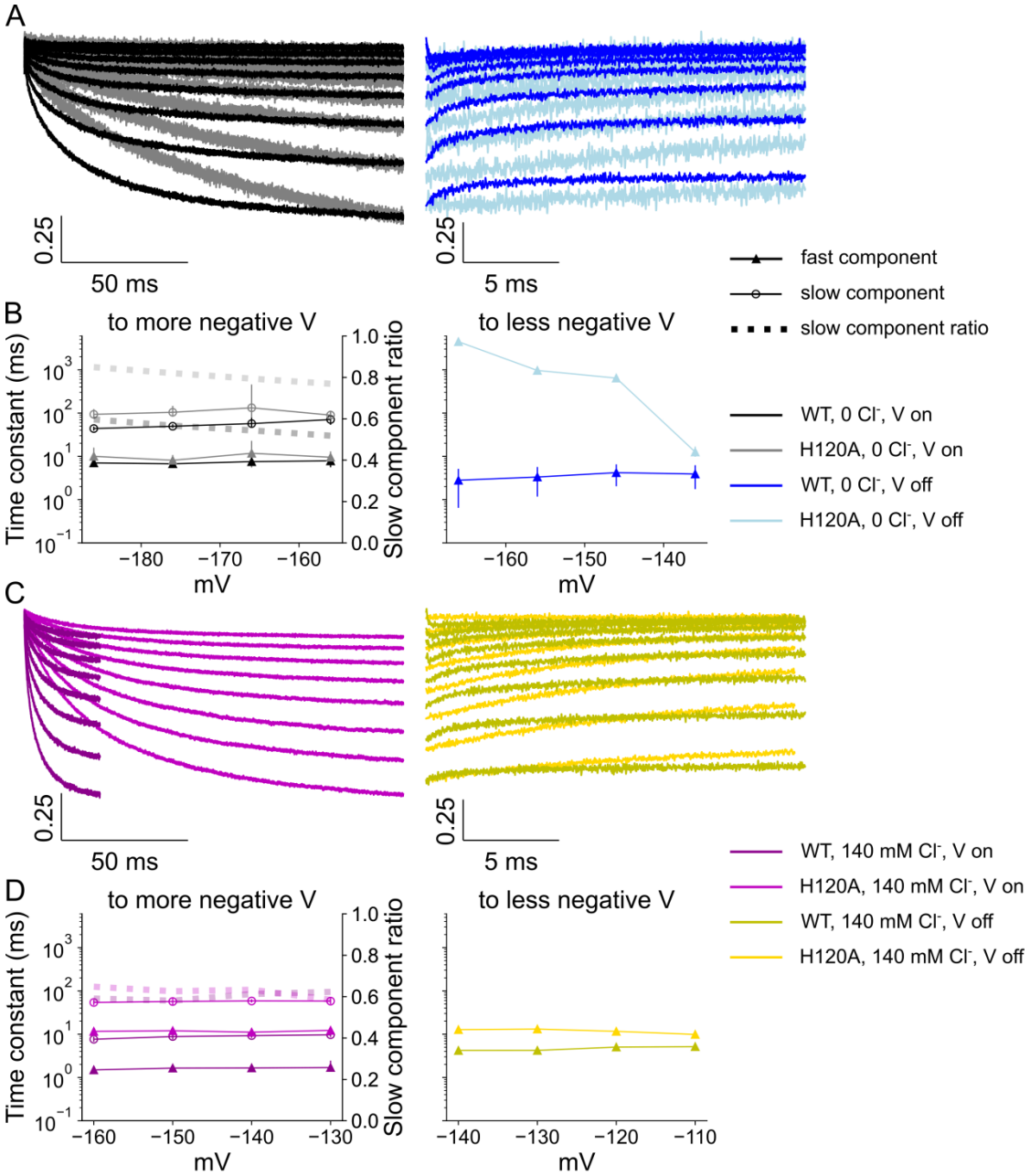

Figure 16: WT VGLUT1$_{PM}$ and H120A, voltage activation and deactivation rates. *Activation by the application of negative V and non-instantaneous deactivation by making the V more positive, in the absence of external Cl^- (A, greys and blues) with corresponding time constants for the WT and H120A (B, n = 11 and 10 for activation on the left, n = 10 and 12 for deactivation on the right), and with 140 mM Cl^- (C, purples and yellows) with corresponding time constants (D, n = 10 and 11 for activation on the left, n = 10 and 11 for deactivation on the right). Data are given as means, obtained by bootstrapping with a global fit with a sampling of 1000, and 95% of the bootstrapped values as confidence interval error bars.*

The most negative voltage, with the highest signal-to-noise ratio, was fitted with exponential functions. If the biexponential function represented the time course better according to an F-test, the fit was broken down into two rate constants with a dashed line quantifying the relative slow component amplitude. All other rate constants were determined with a single exponential function and rate constant. Each figure uses time constants, the inverse of rate constants, to aid in interpretation. The values are distinguished as “on” and “off” when they

show corresponding voltage jumps measured in different experiments. H120A is always shown in a lighter shade of the same base colour than the WT.

Voltage jumps in the absence of external Cl^- activate H120A more slowly than the WT, with a larger slow component, and voltage deactivation becomes nearly linear (Figure 16A). When both are perfused with 140 mM Cl^-, the difference in activation becomes more pronounced in both fast and slow components, while the deactivation and relative slow component amplitude remain about the same for both constructs (Figure 16D). Currents conducted by H120A $VGLUT1_{PM}$ are visibly slower in reaching steady-state current than the WT, so the measurement duration for most experiments with the mutant was increased. The same trend is seen using fast application of different [Cl^-], from 0 to 140 mM on the left and from 140 to 0 on the right (Figure 17). H120A gating in response to [Cl^-] is slower when deactivating and much slower when activating, since it lacks the secondary component that makes the WT faster. This difference suggests that neutralisation of histone 120 reduces the speed with which VGLUT1 interacts with external Cl^-, implying that the histidine normally plays a role in this interaction.

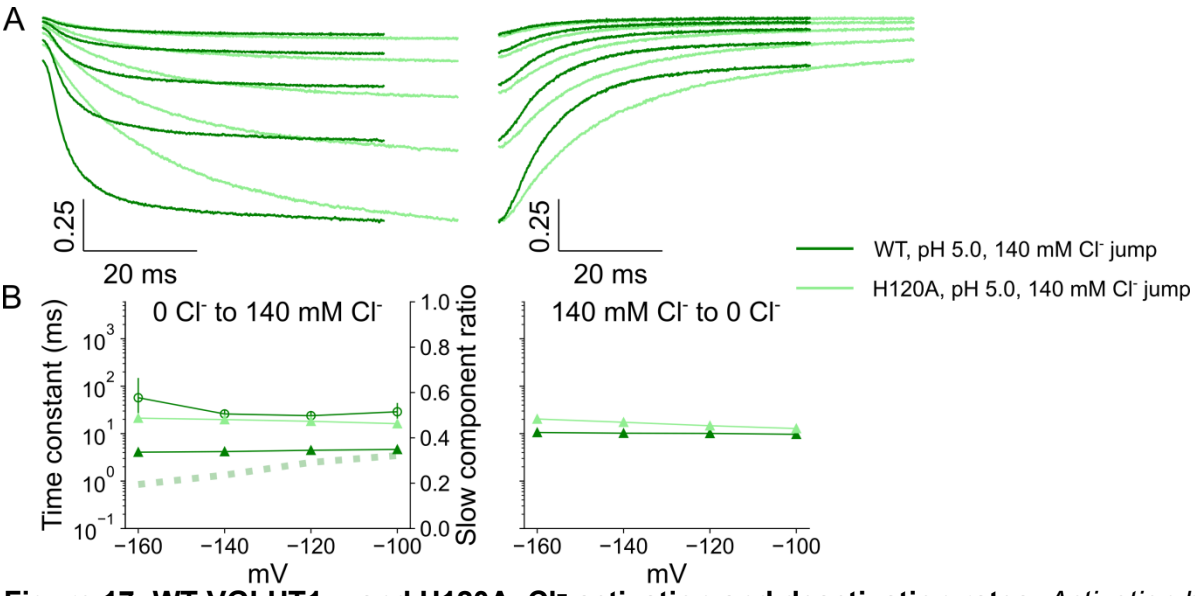

Figure 17: WT $VGLUT1_{PM}$ and H120A, Cl^- activation and deactivation rates. *Activation by increasing external [Cl^-] from 0 to 140 mM followed by deactivation when perfused with 0 Cl^- (A) and corresponding time constants (B, n = 12 for the WT and 13 for H120A). Data are given as mean, obtained by bootstrapping with a global fit with a sampling of 1000, and 95% of the bootstrapped values as confidence interval error bars.*

Activating current with pH 5.5 while keeping the [Cl^-] on the level previously used to activate current, H120A remains slower in both activation and the corresponding relatively fast deactivation (Figure 18A). After removing external Cl^-, however, something interesting happens. The shift in the distribution of exponential rates does not immediately make it clear in the time constants, with only the activation of H120A and the deactivation of the WT being biexponential, but the overall speed of the current response now functionally overlaps (Figure

18C). The only situation where H120A has an overall time course that is not slower than the WT is during pH jumps without allosteric activation by Cl^-.

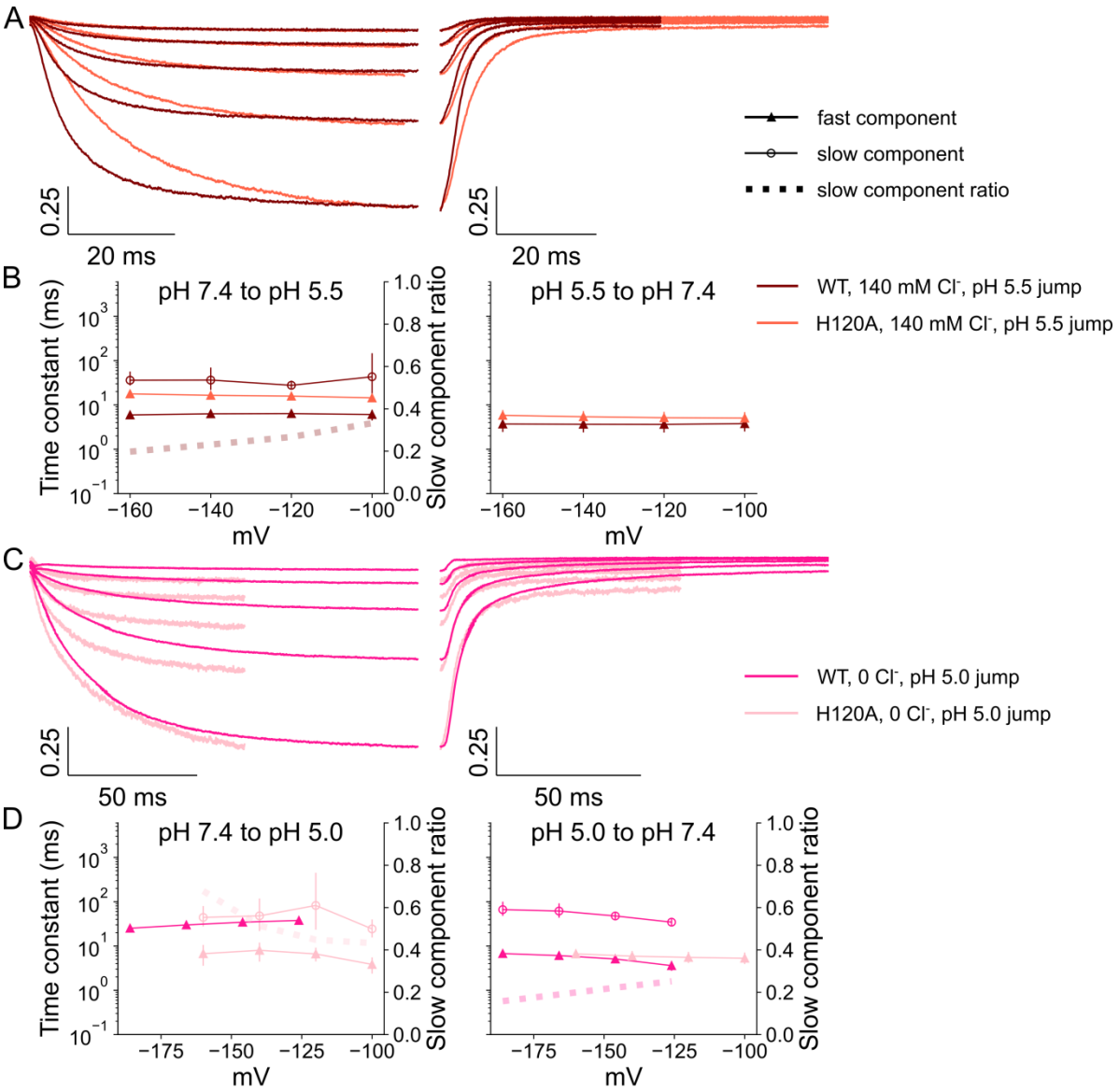

Figure 18: WT VGLUT1$_{PM}$ and H120A, pH activation and deactivation rates. *Activation by application of pH 5.5 and deactivation by returning to pH 7.4, with 140 mM Cl^- (A, reds) with corresponding time constants (B, n = 12 for the WT and 15 for H120A), and with pH 5.0 in the absence of external Cl^- (C, pinks) with corresponding time constants (D, n = 11 for activation and 10 for deactivation of the WT, and 12 for H120A). Data are given as mean, obtained by bootstrapping with a global fit with a sampling of 1000, and 95% of the bootstrapped values as confidence interval error bars. Dataset voltage differences are the result of* a posteriori *liquid junction potential correction.*

Aside from this single exception, H120A VGLUT1$_{PM}$ current responses to changing V, pH, and [Cl^-] are always slower in both activation and deactivation time courses than the WT. Changes in the absence of external Cl^- cause biexponential gating in at least one direction, but only for the WT during activation by an increase in external [Cl^-] or pH. All deactivations with external Cl^- are monoexponential. An overview of experimental time constants describing activation and deactivation is provided in Table 5-S.

3.5 Noise analysis shows H120A increases single channel current in VGLUT1

While stationary noise analysis (at pH 5.5, 140 mM Cl^-, and −160 mV) has previously been used to establish an open probability of 0.24 ± 0.01 (mean and 95% confidence interval) and a unitary current amplitude between 24 ± 1.1 and 25 ± 2 fA (Kolen et al., 2023 [34]), conditions used for the experiments presented here did not elicit enough variance in noise to reliably extrapolate using a parabolic function. To verify this, F-tests were used for individual cells to compare parabolic and linear fits (p = 0.61, 1.0, 0.79, 0.17, 1.0, 1.0, 1.0, 1.0, 1.0, 0.76, 0.96, 1.0, 1.0), finding the relationship between current and variance to indeed be best represented as linear. This means that, instead of Equation 4, the linear function of Equation 5 was used to estimate unitary current. This is calculated from the value representing the slope, fitted to the relationship between its variance and current.

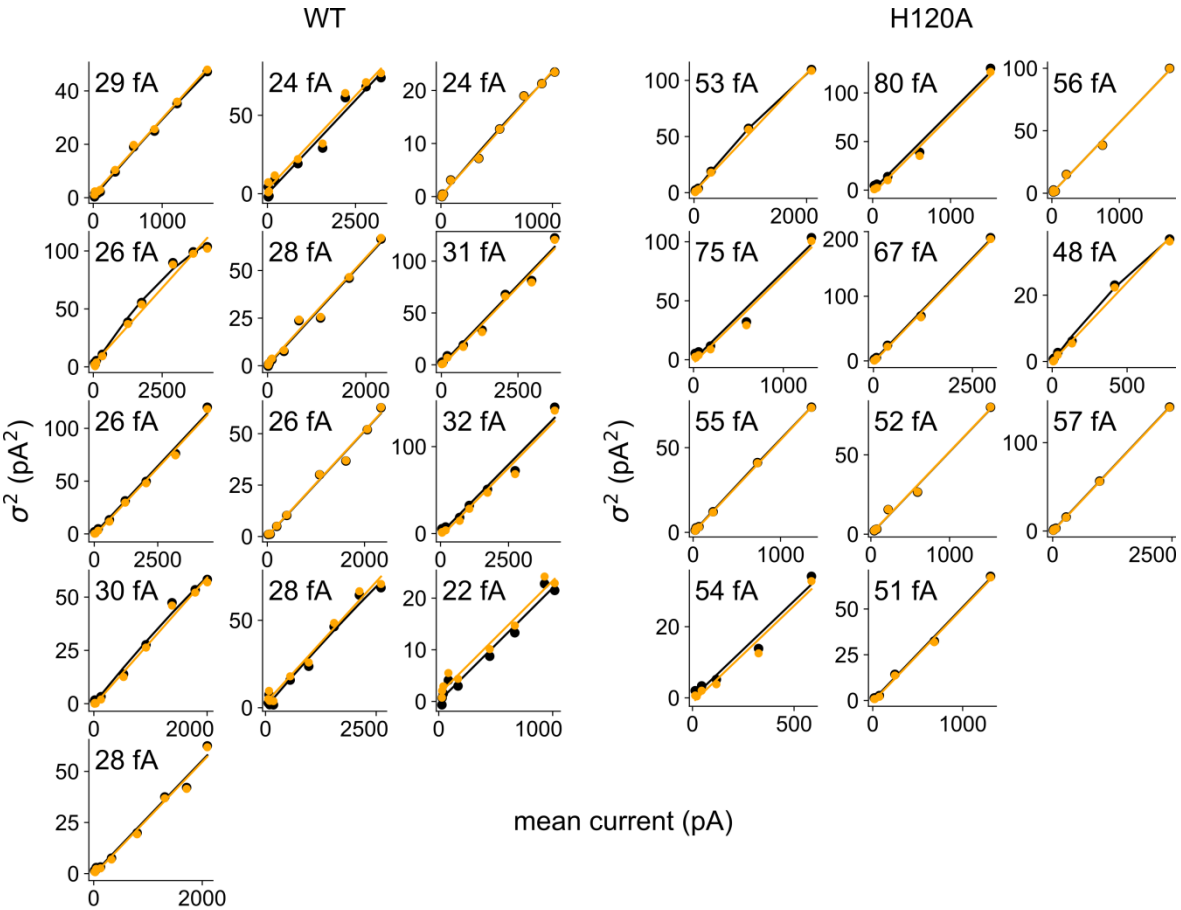

Figure 19: fit of variance-current ratio for WT and H120A VGLUT1$_{PM}$. *Measured points for individual cells fitted with a linear slope function are shown in orange, and the same points fitted with a parabolic function after y-offset subtraction are shown in black. Only linear fitting is used for unitary current calculation, as parabolic fitting was found to not be statistically better overall.*

With 180 mM external Cl^- and −160 mV, this results in average unitary current amplitudes of 27.5 fA ± 0.32 when utilising a global linear fit. This is slightly higher than the previously reported values, possibly because the latter was recorded with a lower [Cl^-] of 140 mM. For

mutant H120A, the data distribution was once again not significantly parabolic (p = 0.08, 1.0, 1.0, 1.0, 1.0, 0.29, 0.68, 1.0, 1.0, 1.0, 1.0). The same global linear fit method found unitary current amplitudes of 59.6 ± 1.1 fA using a similar pH range as the WT. The mutation clearly produces increased unitary current, even though these values are once again slightly higher than those found in previous experiments (52 ± 3.0 fA), now measured at the same [Cl^-] (Kolen et al., 2023 [34]).

External pH and membrane potential do not affect VGLUT1 channel open time

Based on the open time of the Cl^- channel and the frequency with which the data was filtered, the apparent unitary current can change (Silberberg et al., 1993 [68]). The difference is expected to be small while the open time of a channel exceeds the sampling interval, while high-pass filtering of the signal will eventually eliminate significant amounts of channel activity occurring in lower frequencies. Increasing the amount of filtering gradually causes an underestimation of variance, visible as a reduction in calculated unitary current. The way this variance depends on the filter frequency is mainly determined by the duration of the conductive state of the protein, and the way this characteristic is modified by external factors can provide valuable insights into the mechanisms involved. Figure 20 visualises the influence of pH and membrane potential on standard deviation as a proxy for unitary current. The low-pass filter frequency reduces the observed variance in current by obscuring channel opening in a pattern that is dependent on the open time of the channel.

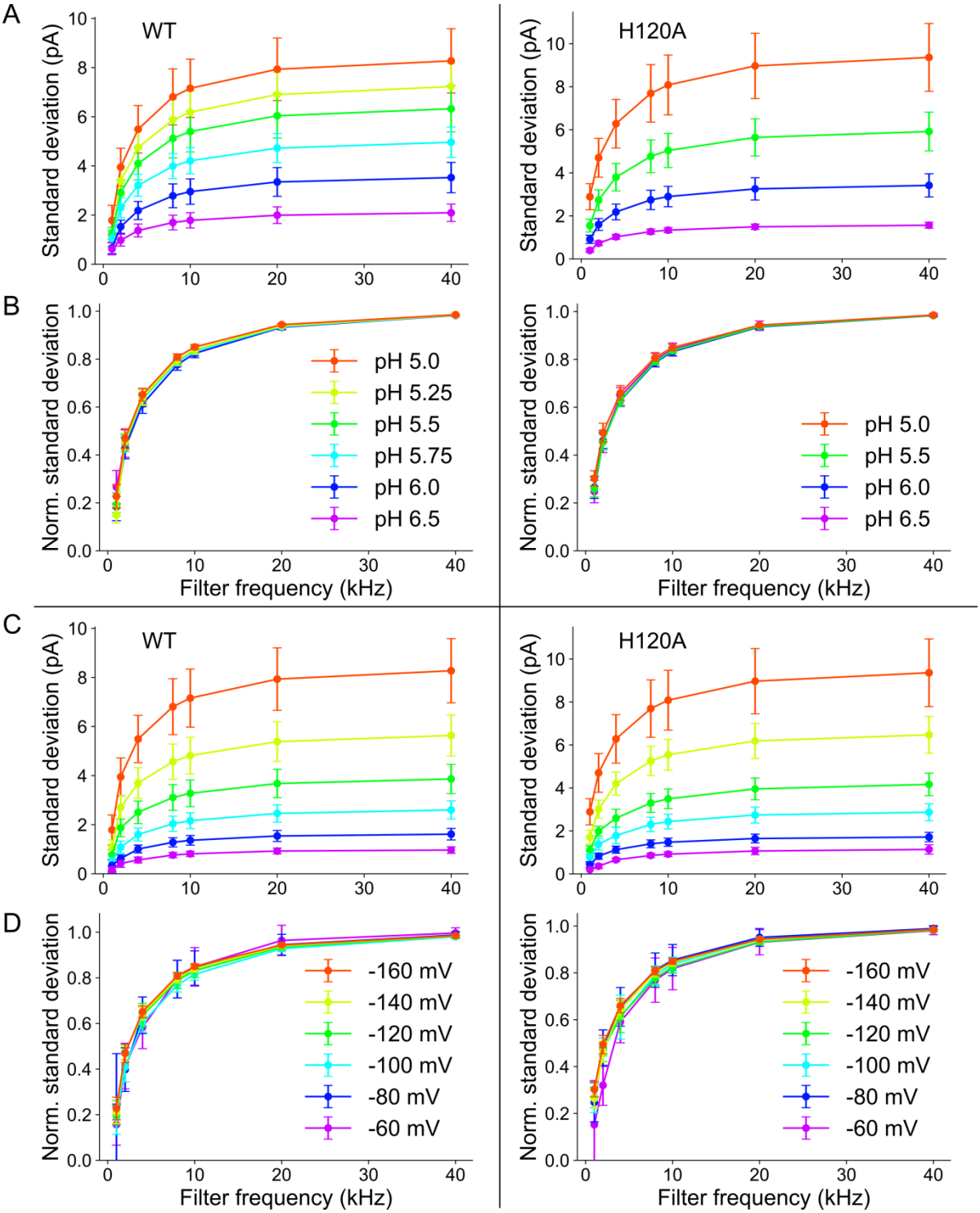

Figure 20: effect of filter frequency on the noise of WT and H120A channel activity. *Standard deviation of current at −160 mV and different external pH values in absolute (A) and normalised (B) amplitudes, and standard deviation of current at pH 5.0 and different voltages in absolute (C) and normalised (D) amplitudes, based on filtering of the same data shown in Figure 19. The noise of the current is calculated as the standard deviation in pA after subtraction of the corresponding 0 mV background. Low current traces with insufficient signal-to-noise ratio are omitted.*

While factors like voltage and pH determine the absolute variance during measurements (Figure 20A and C), normalising this variance shows that all tested conditions exhibit the same decrease with increased filtering (Figure 20B and D). This is evidence that for WT and

H120A VGLUT1$_{PM}$, voltages between −160 and −60 mV and extracellular pH values between 5.0 and 6.5 do not affect channel open time and are therefore not directly involved in the opening and closing of the VGLUT1$_{PM}$ Cl^- channel.

3.6 Short VGLUT1 open times suggest flickering Cl^- channel function

While the average open time of VGLUT1$_{PM}$ does not appear to be directly affected by pH and V, its actual value is also indicative of the transport mode of the protein: channel open times of 1 ms are reportedly affected only mildly by filtering between 1 and 15 kHz, while the noise simulated for active transport through an alternating access mechanism with an approximated duration of 10 µs decreases in an approximately linear fashion (Alekov et al., 2009 [58]). This implies a gradient of filter frequency dependence between transporter open times of circa 10 µs and classical channels that remain open for 1 ms or more. The open time of a channel can be estimated with a stochastic representation that simulates random channel opening and closing using a given open probability. Using a variety of open times for the simulation, chosen in such a way that it matches the experimental filter frequency dependence, the real open time can be approximated. This method found an average open time of 82.5 ± 5.7 µs (mean and 95% confidence interval) for WT VGLUT1$_{PM}$ at −160 mV and 180 mM external Cl^-. The H120A mutation appears to leave the channel open time mostly unchanged, with 86.2 ± 3.6 µs at −160 mV and 140 mM external Cl^-. An open probability of 0.24 was used for both (Kolen et al., 2023 [34]).

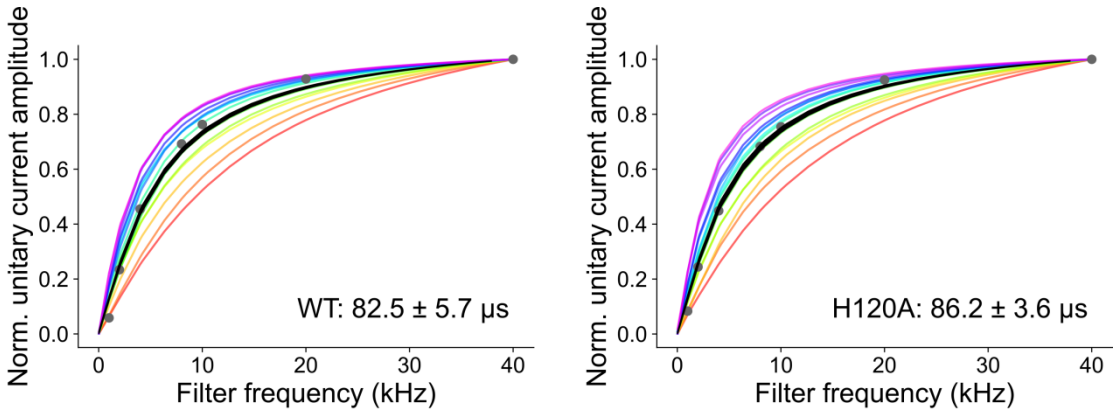

Figure 21: filter frequency dependence of experimental and simulated unitary current. *Empirical values based on linear fits (Figure 19) represented by grey markers and a representative run of 15 simulated open times in red to violet (60–120 µs). The mean of the most accurate open times from ten simulations is shown as a black 95% confidence interval.*

The accuracy of this result, aside from the calculations and the provided data being correct, is reliant on multiple assumptions. Ideally, the various conformational and ligand-bound states of the protein can be fairly summarised as one open and one closed state. Open times for this protein should have relatively limited variation, and the bulk of channel open times may not be below the simulated time step of 10 µs. Based on the results shown above and

available information, it seems these assumptions hold for $VGLUT1_{PM}$. It appears that all experiments analysing the Cl^- channel of $VGLUT1_{PM}$, both WT and H120A, consistently show an open time of approximately 100 µs. This places it firmly in the intermediate flickering channel range, among other channels responsible for a significant portion of noise in neuronal circuits (Yu et al., 2017 [69]).

3.7 A kinetic model to describe VGLUT1 channel function

The kinetic model describing $VGLUT1_{PM}$ Cl^- current relies on a combination of experimental experience and several assumptions. Any Cl^- channel capable of producing significantly different current amplitudes at a single voltage, depending on other conditions, requires at the very least a closed and open state. The simplest kinetic model for such a situation would only have two states, which leaves no room for modulation by ligands or other allosteric effects. A protonation to a second closed step can be added for a third state, connecting the closed *apo* state and the (now protonated) open state. It would, however, be difficult to justify the absence of a way to unbind its proton from such an open and environmentally exposed structure. It makes sense to add an unprotonated open state between the protonated open state and the *apo* state. This produces a square with symmetrical transition pairs, each along their own dimension in the scheme. The resulting four-state model effectively has a single activation process.

Based on previously shown Cl^- current gating analysis of WT $VGLUT1_{PM}$, channel opening by either voltage or acidification occurs through processes best described as a combination of two exponential functions. This already applies before modulation by external [Cl^-] is taken into account. The four-state kinetic model would be unable to fully reproduce such biexponential gating and is therefore insufficient as a starting point. This was confirmed by the failure of various small models to represent experimental data. Consequently, the model that was ultimately chosen was given a second sequential protonation site for a total of six states. Computational approaches used to investigate VGLUT1 and its family members consistently find multiple protonatable residues in its active site, which makes double protonation possible and a likely prerequisite for its full channel function (Thompson et al., 2020 [70]). The six-state model permits channel opening through two differently protonated states. As a simplified version, it was tested on measurements of voltage and pH jumps in the absence of external Cl^- (Figure 12D) to ensure viability. After proving to be suitably flexible, the data used for model fitting was extended with experiments involving increased [Cl^-] (Figure 12E and F) and used with a completed model where each state can bind Cl^-.

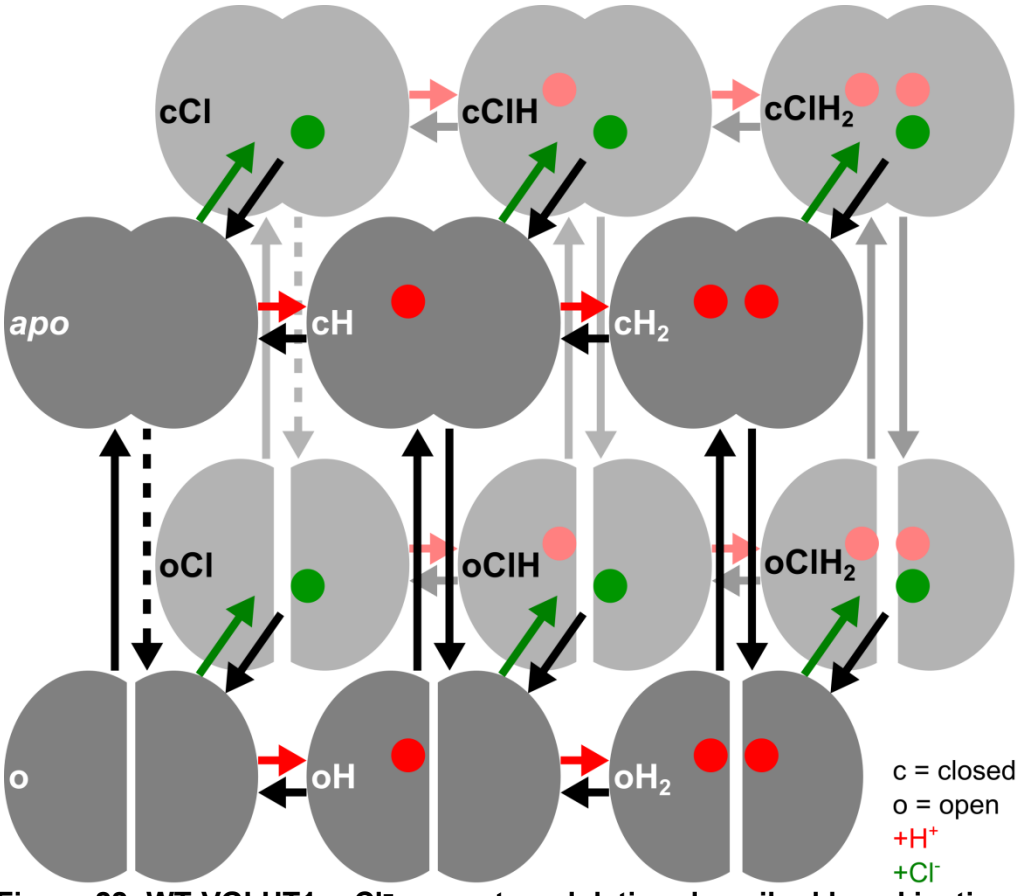

Figure 22: WT VGLUT1$_{PM}$ Cl^- current modulation described by a kinetic model. *Twelve-state model where columns separate the binding of ligands H^+ (red, left to right) and Cl^- (green, from the front to the lighter-coloured background) with binding step arrows in the same colour and unbinding in black. The six states on top depict a closed channel, able to open via black-arrowed vertical conformational change (restricted unprotonated opening shown as dashed lines) to the six open channel states on the bottom with varying channel width to represent current increase with ligand binding.*

Each transition must be possible in both directions. VGLUT1 empirically requires acid activation, so it cannot show substantial channel opening directly from *apo* or the closed state with only Cl^- bound. This unprotonated opening (shown as a dashed line in model schematics) is deemed unfeasible and limited to a base rate constant of 1 s^{-1}, a factor 10,000 lower than the upper bound for other conformational changes. Modification by the membrane potential allows a limited ability for net transition rates to exceed this restriction.

3.7.1 Simulated WT VGLUT1 Cl^- current

Through a customised DEAP algorithm for model fitting, an initial set with charge movement (*z*), symmetry (*d*), and rate constants of intermediate value was subjected to mutation and optimisation. The goodness-of-fit was determined using various quantifications of activity for both the simulation and the experimental training data, and the RSS between them was minimised by continuously selecting the most accurate parameter sets. The final optimised set of parameters is shown in Table 6-S. To get an impression of the specificity of the model and its parameters, this optimised set was subjected to exploratory mutation within 125% of

the goodness-of-fit for each point of comparison to collect at least 10,000 viable individuals. An equidistant selection of 250 of these individuals was simulated for each experiment (Figure 23A–I), where the spread represents the variance present in a population that closely matches the experimental characteristics of VGLUT1$_{PM}$.

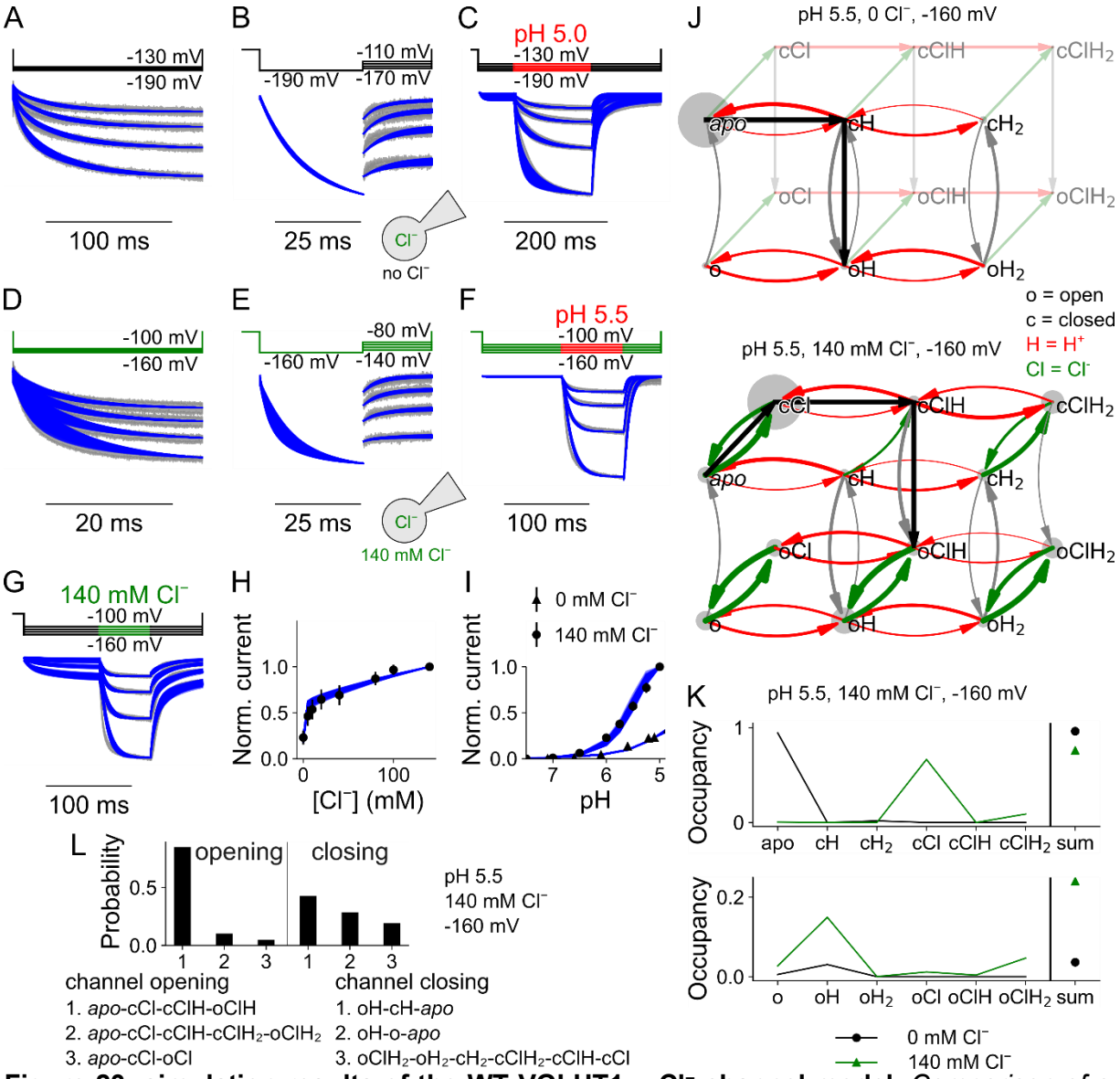

Figure 23: simulation results of the WT VGLUT1$_{PM}$ Cl⁻ channel model. *Comparison of a 95% confidence interval of experimental results overlaid with 250 equidistant simulations of the same conditions in blue from a population of 10,000 for voltage steps from 0 down to negative V (A), from more negative to less negative V (B), and during pH change (C) in the absence of external Cl⁻ (black voltage protocols), voltage steps from 0 down to negative V (D), from more negative to less negative V (E), and during pH change (F) with 140 mM [Cl⁻], Cl⁻ jump from 0 to 140 mM (G), and overall dependence on [Cl⁻] (H) and pH (I, data with 0 external Cl⁻ was normalised, and then scaled to relative current compared to 140 mM Cl⁻ at pH 5.0), relative state occupancy in grey circles and rates as black arrows at 0 and 140 mM Cl⁻ showing the primary* apo*-to-open pathway (J), occupancy of closed and open states (K), and three most common opening and closing pathways (L, any opening from* apo *and closing from the most common two open to any unprotonated state).*

Relative probabilities of channel opening or closure are calculated with the reactive flux module of the Deeptime Python library, which is based on transition path theory (Metzner et al., 2009 [71]). This analysis reveals that the preferred opening pathway from the *apo* state of VGLUT1 is initial Cl^--binding and protonation, followed by conformational change to enter the open channel mode as oClH (Figure 23J and L). The top three pathways to close from the two most common open channel conformations are much closer in probability, mainly returning to the unprotonated states via the most common open state, oH (Figure 23L and K). The simulated open probability is trained to match the value determined via previously published noise analysis at −160 mV, pH 5.5, and a symmetrical 140 mM [Cl^-] (Kolen et al., 2023 [34]). The simulated open probability decreases from 0.24 at 140 mM Cl^- to 0.04 in the absence of external Cl^-, with negligible variation for both. This appears to be a suitable approximation of the findings showing 20% of steady-state current remaining after all Cl^- is removed from perfusion solutions (Figure 12B). The 250 sampled variants have an open time of 78.1 ± 1.4 µs (mean and 95% confidence interval) regardless of pH or [Cl^-], closely matching the noise analysis prediction of 82.5 ± 5.7 µs (Figure 20), which is independent of pH and V.

The simulation can be tested against the experimental results using their fitted time constants. The biggest absolute difference is found in the fast component of the activating voltage jump with 140 mM external Cl^-, with the simulation being slower due to it covering most of the gating with a higher ratio of the slower process (Figure 24A). The same happens to the Cl^--free equivalent, with the model predicting very little contribution by the fast component. Aside from this difference, all time constants appear to have realistic values, well within an order of magnitude of the experimental data.

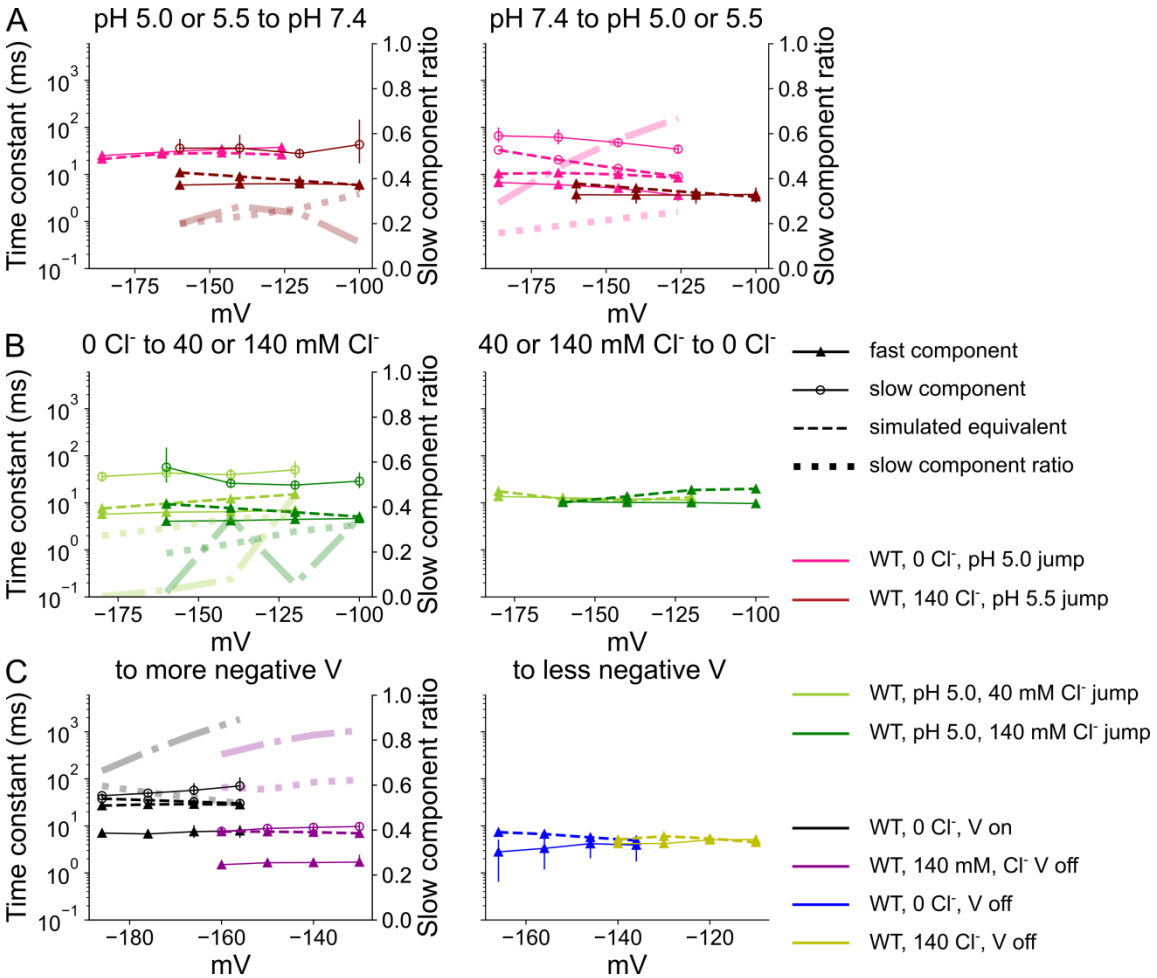

Figure 24: WT time constants fitted to experimental data and simulation. *Time constants of activation or deactivation by pH change (A), [Cl⁻] change (B), and voltage jump (C) with fits of the same selection of 250 simulations shown in Figure 23. Data are given as mean, obtained by bootstrapping with a global fit with a sampling of 1000, and 95% of the bootstrapped values as confidence interval error bars. Dataset voltage differences are the result of* a posteriori *liquid junction potential correction.*

3.7.2 Modelled WT VGLUT1 Cl^- channel rates

A visual representation of model variance was generated in two separate ways. Values obtained by the aforementioned exploratory mutation are shown sorted by protonation, Cl^--binding, and open state (Figure 25). Processes involving the association and dissociation of protons tend to be too fast to be meaningfully described by individual rates, so simulations of these rates are combined into pK_a values instead (Figure 25A). Violin plots show the total amplitude spread for each parameter, or pK_a calculated from two rate amplitudes, as obtained through exploratory mutation. The effect of manual amplitude variation on the overall goodness-of-fit (as RSS) is additionally shown for individual rates, with overlap below 150% RSS or between violin plots interpreted as the values of different rates being indistinguishable.

At −160 mV, Cl^- increases the pK_a of the first protonation from 1.1 (for a total amplitude range of 0.9–1.2) to 2.0 (1.7–2.1; solid violin plots). This is after a reduction caused by the membrane potential used for the experiments that were simulated: without the negative voltage (drawn in open rectangles or dashed lines), the *apo* state pK_a would be 2.3 (2.1–2.4) rather than the aforementioned 1.1 (0.9–1.2), and 4.3 (4.1–4.5) instead of 2.0 (1.7–2.1) after Cl^- binding. For the second proton in the closed state, the voltage increases the pK_a from 6.3 (6.0–6.5) to 8.3 (8.2–8.5) without and from 6.4 (6.1–6.7) to 8.4 (8.1–8.6) with Cl^- bound. Cl^- reduces the first protonation pK_a of the open channel from 6.3 (6.2–6.4) to 5.0 (5.0–5.1), but increases it for the second protonation from 3.1 (3.0–3.3) to 6.7 (6.5–6.9). This, combined with opening from a single protonated state, may explain the relatively high occupancy of $cClH_2$ while VGLUT1 is closed (Figure 23K).

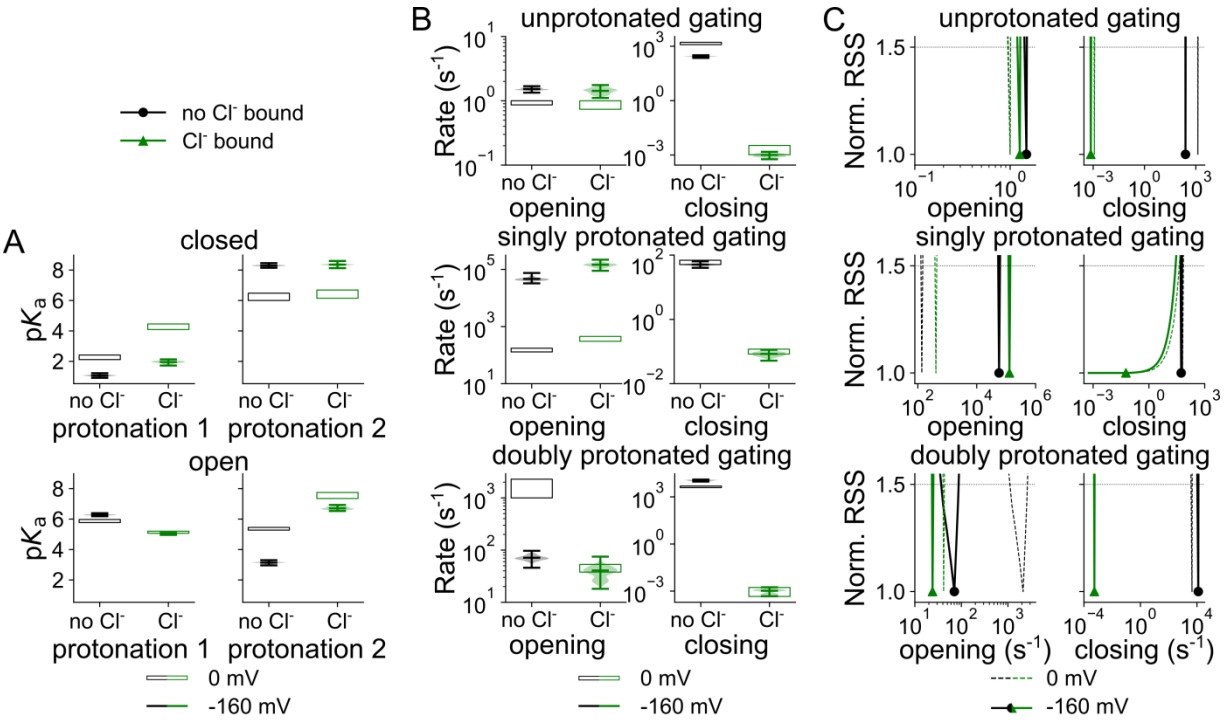

Figure 25: effect of allosteric Cl^- on modelled pK_a and opening rates of WT VGLUT1. *Simulated rate constant-based pK_a generated through exploratory mutation shown as violin plots (A), exploratory mutation violin plots showing transition rates between open and closed channel states (B), and transition rates between open and closed channel states depicted as normalised RSS representing goodness-of-fit (C). Transitions between Cl^--free states are shown in black and between Cl^--bound states in green, with base rate constants shown as empty rectangles or dashed lines and the corresponding solid styles depicting rates as modified by a membrane potential of −160 mV. Corresponding* z *and* d *parameters are shown in Figure 48-S.*

Cl^- binding to VGLUT1 promotes channel opening by increasing the rate with single protonation from 4.6×10^4 (3.3×10^4–7.5×10^4) s^{-1} to 1.5×10^5 (9.0×10^4–2.2×10^5) s^{-1}. This opening is highly voltage-dependent and much higher than it would be without a membrane potential, with 157 (129–174) s^{-1} and 361 (305–451) s^{-1} without and with Cl^-, respectively. The primary current-boosting effect of Cl^- appears to be found in a reduction in closing rates

across the board, from 277 (228–319) s^{-1} to 9.9×10^{-4} (5.8×10^{-4}–1.5×10^{-3}) s^{-1} when unprotonated, 51 (40–64) s^{-1} to 0.08 (0.05–0.11) s^{-1} when singly protonated, and 1.1×10^{4} (9.4×10^{3}–1.3×10^{4}) s^{-1} to 1.1×10^{-3} (4.7×10^{-4}–1.8×10^{-3}) s^{-1} when doubly protonated (Figure 25B). Note that opening rate constants for unprotonated opening are limited to 1 s^{-1} and, prior to modification by membrane potential, never exceed one transition per second.

Average concentration-normalised rates for the binding of Cl^-, as well as unbinding rates, are higher when the channel is in its open conformation under standard conditions (pH 5.5, 140 mM Cl^-, −160 mV; Figure 26A). This makes sense with the increased accessibility expected for a protein in an open conformation. Association to the closed channel is noticeably lower for the singly protonated state, with concentration-normalised rates of 1.8×10^{3} (1.6×10^{3}–2.1×10^{3}) M^{-1} s^{-1}, compared to 6.7×10^{8} (5.8×10^{8}–7.2×10^{8}) M^{-1} s^{-1} and 1.1×10^{7} (9.4×10^{6}–1.3×10^{7}) M^{-1} s^{-1} for unprotonated and doubly protonated states, respectively. Unbinding rates show the same pattern, with the singly protonated state being several orders of magnitude lower than both other states. Like protonation, rates of Cl^- association affect the probability of binding site occupation. To determine whether the effects protonation has on VGLUT1 Cl^- binding are due to changes in association rates or binding affinity, a similar RSS test is shown where unbinding is changed in tandem with binding to maintain a constant ratio and thereby exclude the influence of the Cl^- K_D (Figure 26B). Only singly protonated Cl^- in the closed state is sharply defined, revealing that the individual association rates of its decreased affinity are more important here than for any of the other states. This suggests that, during anion channel activation, VGLUT1 transiently assumes occluded states where the Cl^- binding site is not accessible from the external solution.

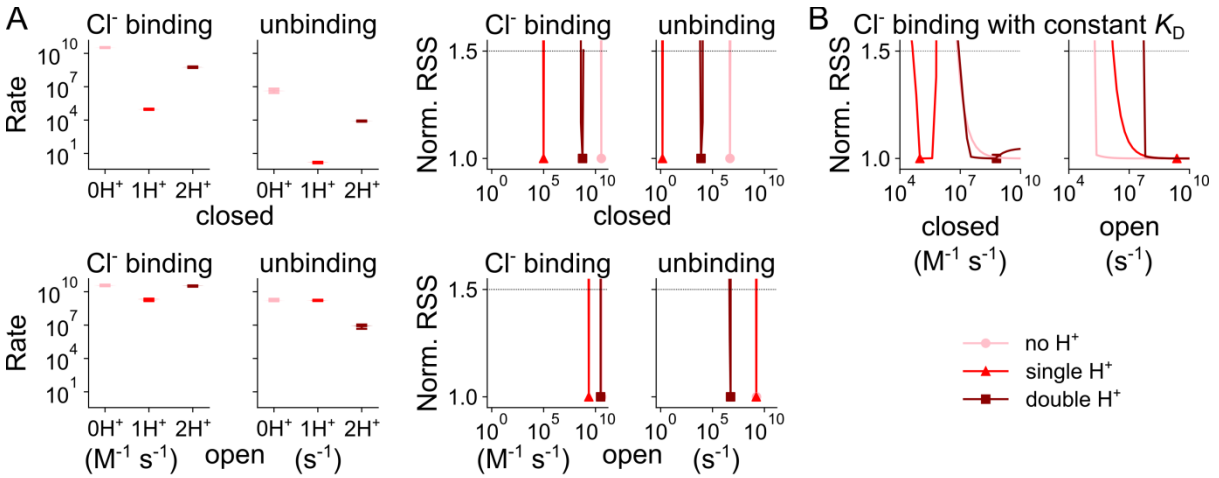

Figure 26: modelled rates for the binding and unbinding of Cl^- by protonation state. *[Cl^-]-normalised rates at −160 mV depicted as exploratory mutation violin plots or normalised RSS representing goodness-of-fit (A) and the effect of changing Cl^- binding amplitude on RSS while maintaining the K_D through a parallel shift in unbinding (B). Darker red indicates a higher protonation number. Corresponding* z *and* d *parameters are shown in Figure 48-S.*

3.7.3 Simulated H120A VGLUT1 Cl^- current

Experimental datasets equivalent to those used for the kinetic model representing WT VGLUT1$_{PM}$ were collected for mutant H120A. The same kinetic model was fitted to these experimental values and time courses and then once again mutated and optimised with the DEAP algorithm. Several of the calculated values and steady-state behaviours determined for the WT are not hugely different in H120A (Figure 27B and C). H120A exhibits an unchanged pK_M value of 5.4 ± 0.003 (mean and 95% confidence interval; Hill coefficient of 1.3) with 140 mM Cl^- (compared to the WT with 5.4 ± 0.003, Hill coefficient of 1.1, p = 0.89), but a reduced pK_M of 5.0 ± 0.004 (Hill coefficient of 1.2) without external Cl^-, compared to 5.3 ± 0.003 for the WT (Hill coefficient of 1.2, p = 2.2×10^{-6}). The mutation decreased the K_M to 19.4 ± 0.2 mM Cl^-, down from 28.3 ± 0.7 for the WT (p = 0.047). These differences, combined with its slower overall gating, required a substantial adjustment of the kinetic variables.

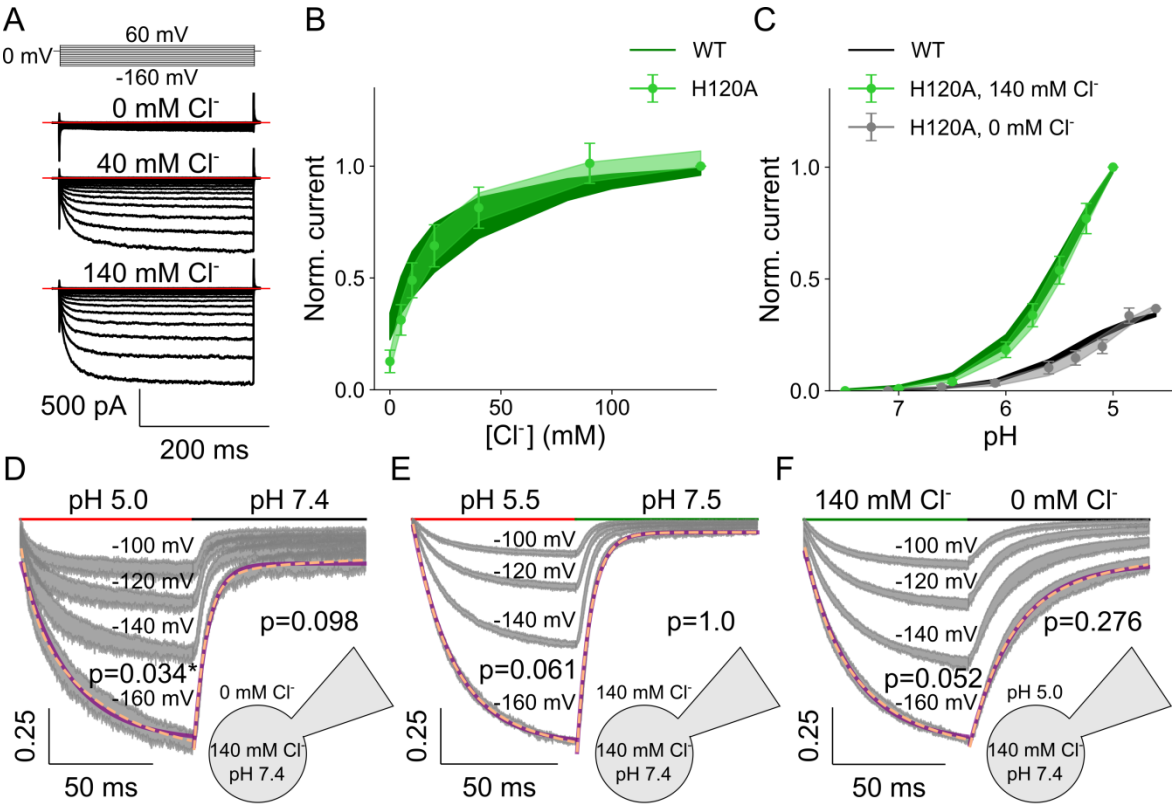

Figure 27: H120A VGLUT1$_{PM}$ Cl^- current modulated by voltage, external pH, and [Cl^-]. *Representative recording of H120A depicting voltage steps at pH 5.5 and various external [Cl^-] (A), steady-state current dependence on external [Cl^-] (B, −160 mV and pH 5.5, contrasted to dark green for the WT) and steady-state current dependence on pH (C, no external Cl^- in grey and 140 mM Cl^- in light green, −160 mV, contrasted to the WT in black and dark green), and current time courses responding to pH jumps in the absence of external Cl^- (D, n = 12), pH jumps with 140 mM external Cl^- (E, n = 15), and Cl^- jumps (F, n = 13). Data is shown as mean ± 95% confidence interval; p-values indicate whether the maximum current trace is described significantly better with a double (dashed orange) rather than a single (purple line) exponential function.*

Eventually, the optimised set of parameters once again settled on a distribution that allows Cl^- current behaviour to be replicated fairly reliably. With a minimally varying open probability of 0.25, similar to the WT, H120A can produce different gating while maintaining accurate pH and Cl^- dependence (Figure 28A–I). The optimised H120A parameter set is shown in Table 7-S.

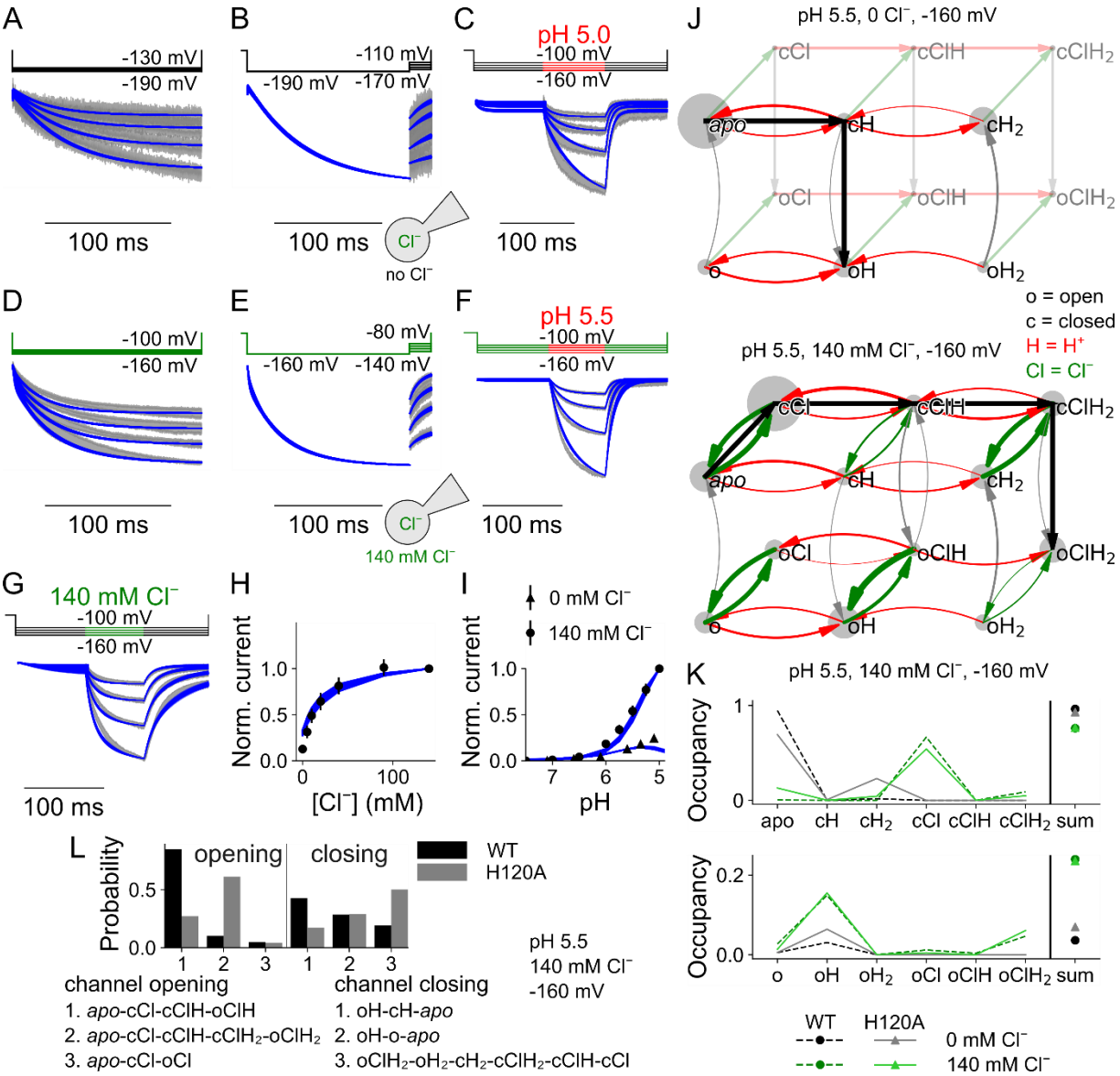

Figure 28: simulation results of the H120A VGLUT1$_{PM}$ Cl^- channel model. *Comparison of a 95% confidence interval of experimental results overlaid with 250 equidistant simulations of the same conditions in blue from a population of 10,000 for voltage steps from 0 down to negative V (A), from more negative to less negative V (B), and during pH change (C) in the absence of external Cl^- (black voltage protocols), voltage steps from 0 down to negative V (D), from more negative to less negative V (E), and during pH change (F) with 140 mM [Cl^-], Cl^- jump from 0 to 140 mM (G), and overall dependence on [Cl^-] (H) and pH (I, data with 0 external Cl^- was normalised, and then scaled to relative current compared to 140 mM Cl^- at pH 5.5), relative state occupancy in grey circles and rates as black arrows at 0 and 140 mM Cl^- showing the primary* apo*-to-open pathway (J), occupancy of closed and open states (K), and three most common opening and closing pathways (L, any opening from* apo *and closing from the most common two open to any unprotonated state) compared to the WT in darker or dashed lines.*

Using the same relative current normalisation, the simulated open probability without external Cl^- is a feasible 0.07, slightly higher than the same value simulated for the WT. Once again pH and [Cl^-]-independent, the simulated open times for H120A are 83.4 ± 0.7 µs (mean and 95% confidence interval), overlapping with the experimental value of 86.2 ± 3.6 µs (Figure 20). Protonation-based simulated gating in an absence of Cl^- is not too different from the WT, still opening mainly with a single proton, but the presence of Cl^- shifts opening towards double protonation (Figure 28J). Like the simulated version of the WT, simulated H120A time constants can be compared to the corresponding experimental data. To allow comparison between both simulations, the axes against which time constants are plotted were kept the same. The simulation of the mutant compares to its experimental data similarly to the WT, with the bigger differences found in rates for the activating voltage jumps where the simulation predicts a lower contribution of the fast component. Voltage deactivation is additionally difficult to fit with an exponential function, being nearly linear.

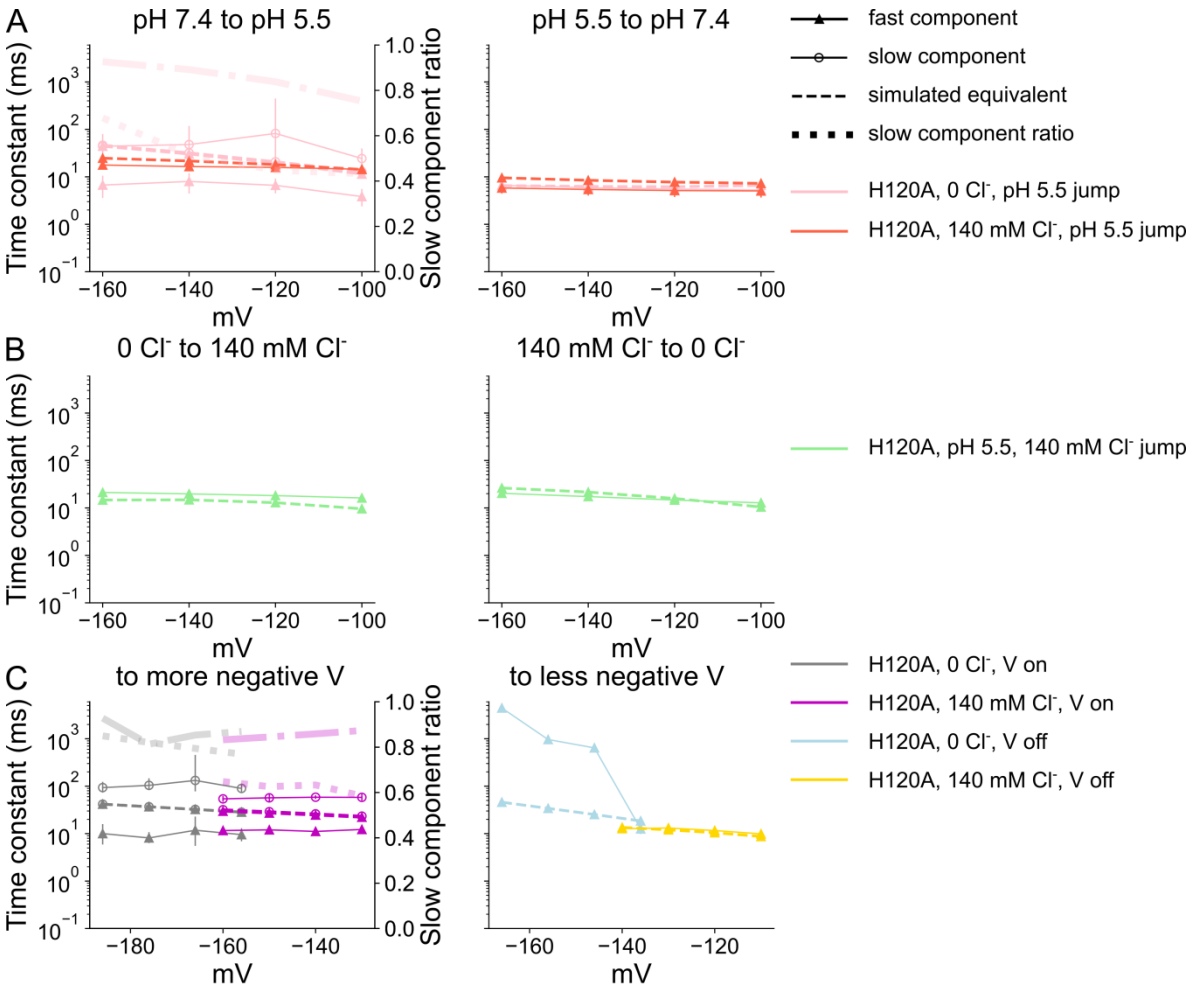

Figure 29: H120A time constants fitted to experimental data and simulation. *Time constants of activation or deactivation by pH change (A), [Cl^-] change (B), and voltage jump (C) with fits of the same selection of 250 simulations shown in Figure 28. Data are given as mean, obtained by bootstrapping with a global fit with a sampling of 1000, and 95% of the bootstrapped values as confidence interval error bars. Dataset voltage differences are the result of* a posteriori *liquid junction potential correction.*

3.7.4 Effect of H120A VGLUT1 on modelled rates

Without Cl^-, H120A strongly increases the pK_a of the first protonation site of the closed channel from 1.1 (0.9–1.2; median and parameter amplitude range) to 3.7 (3.5–3.9; Figure 30A, corresponding *z* and *d* parameters shown in Figure 48-S). While still higher than the WT, Cl^- binding to H120A slightly reduced the *apo* pK_a to 3.1 (2.8–3.2). H120A impairs the protonation of the second site, regardless of Cl^-. For Cl^--bound open VGLUT1, H120A decreases the pK_a of the first protonation site from 5.0 (5.0–5.1) to 2.7 (2.6–3.0), with a smaller increase from 6.7 (6.5–6.9) to 7.8 (7.6–8.0) for the second protonation site. While by itself not enough to explain the slowed-down gating displayed by the mutant whenever the external [Cl^-] is high, this does fit with the observation that only acidification without external Cl^- results in gating comparable to the WT.

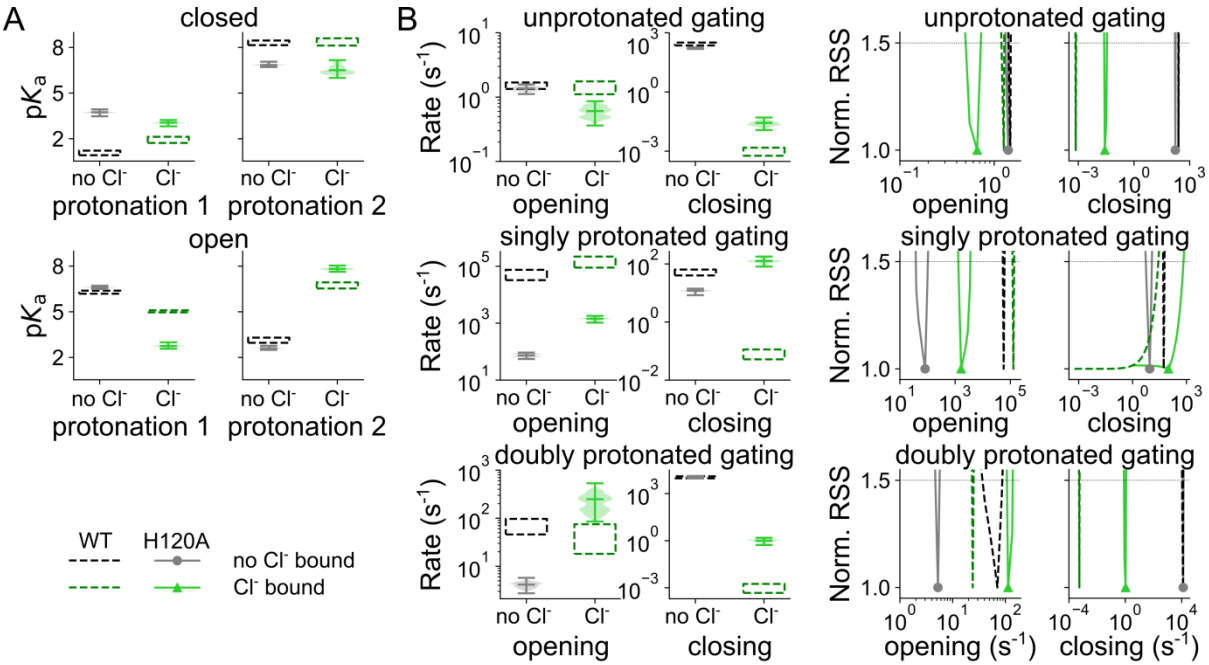

Figure 30: Cl^- modulating modelled pK_a and opening rates of WT and H120A VGLUT1. *Simulated rate constant-based pK_a at −160 mV generated through exploratory mutation shown as violin plots (A) and transition rates between open and closed channel states depicted as exploratory mutation violin plots or normalised RSS representing goodness-of-fit (B). Transitions between Cl^--free states are shown in black and between Cl^--bound states in green, the WT in darker dashed lines and H120A in lighter solid styles. Corresponding* z *and* d *parameters are shown in Figure 48-S.*

H120A decreases singly protonated opening rates, from 4.6×10^4 (3.3×10^4–7.5×10^4) s^{-1} to 74 (55–93) s^{-1} without Cl^- and from 1.5×10^5 (9.0×10^4–2.2×10^5) s^{-1} to 1439 (1044–1807) s^{-1} with Cl^- (Figure 30B). For doubly protonated states, H120A has a lower opening rate than the WT in the absence of Cl^- with 4.2 (2.7–5.7) s^{-1} versus 71 (46–97) s^{-1}, but a higher rate in its presence with 250 (85–532) s^{-1} versus 41 (18–75) s^{-1}. While Cl^--bound, it additionally increases closing rates: from 9.9×10^{-4} (5.8×10^{-4}–1.5×10^{-3}) s^{-1} to 0.026 (0.012–0.050) s^{-1} when unprotonated, and from 1.1×10^{-3} (4.7×10^{-4}–1.8×10^{-3}) s^{-1} to 1.0 (0.5–1.5) s^{-1} when doubly protonated. H120A alters preferred pathways through changes in channel opening

and closing, effectively switching its preferred Cl^--activated opening state from single to double protonation. While neither of the individual singly protonated closing rates are sharply defined, it is likely that a much higher closing rate distribution contributes to this pattern.

Figure 31 shows a pronounced reduction in the Cl^- association under the influence of H120A, with corresponding *z* and *d* parameters given in Figure 48-S. It increases binding and unbinding rates for the closed channel and, except for singly protonated binding, reduces all rates for the open channel (Figure 31A), suggesting reduced binding stability.

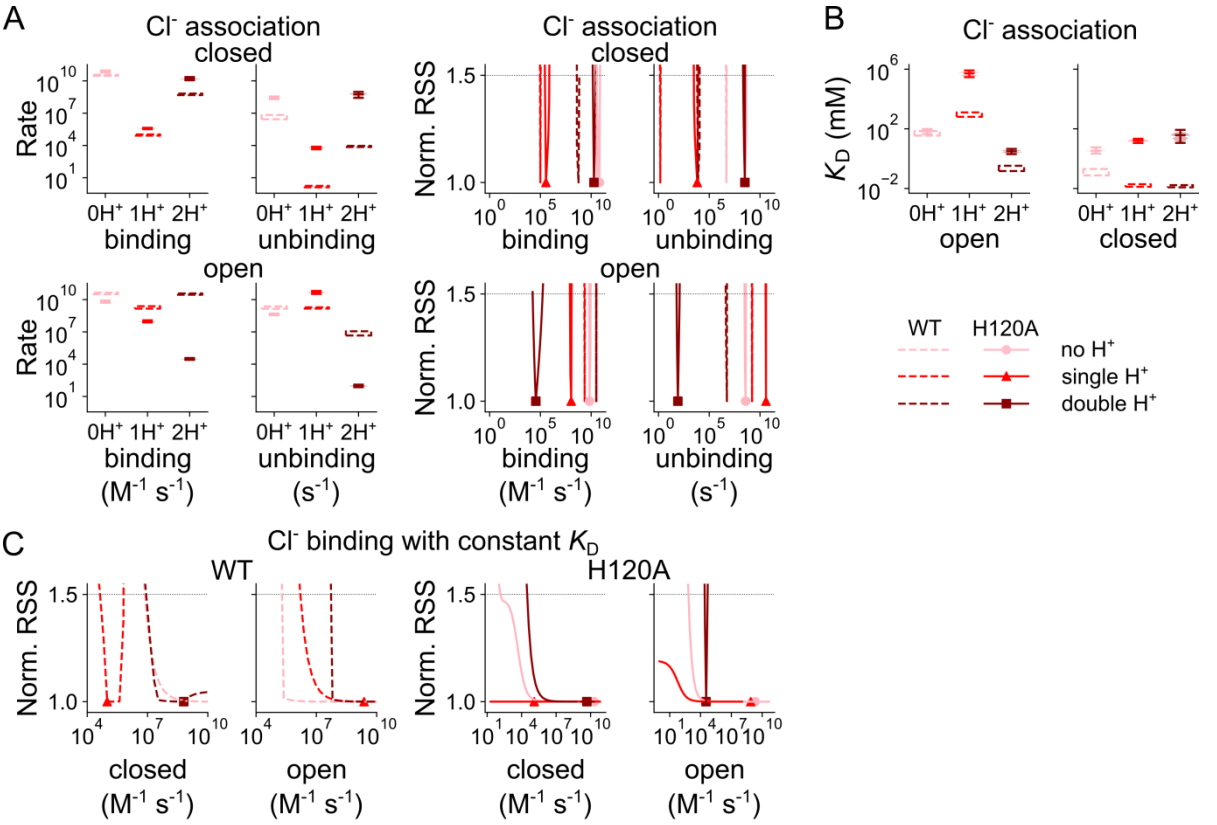

Figure 31: modelled rates for binding and unbinding of Cl^- by protonation state. *[Cl^-]-normalised rates at −160 mV depicted as exploratory mutation violin plots or normalised RSS representing goodness-of-fit (A), dissociation constants calculated from these rates (B), and the effect of changing Cl^- binding amplitude on RSS while maintaining the K_D through a parallel shift in unbinding (C). Darker red indicates a higher protonation number. Corresponding* z *and* d *parameters are shown in Figure 48-S.*

Whereas H120A has the same Cl^- dissociation constant for the unprotonated open channel, the trend of higher exchange rates causes an increase in K_D in all other states. In open channels it increases from 869 (641–1263) mM to 5.8×10^5 (2.9×10^5–8.3×10^5) mM when singly protonated and from 0.24 (0.15–0.36) mM to 3.1 (2.0–4.5) mM when doubly protonated, in closed channels from 0.12 (0.08–0.20) mM to 3.4 (2.2–5.8) mM when unprotonated, from 0.017 (0.013–0.019) mM to 16 (11–22) mM when singly protonated, and from 0.014 (0.012–0.017) mM to 38 (11–85) mM when doubly protonated. Testing the variation in Cl^- binding to an open or closed channel at a fixed affinity and finding no

distinction in the individual rates demonstrates that H120A changes the affinity of the binding site rather than its accessibility (Figure 31C).

3.8 WT VGLUT1 transports $Glut^-$ and Asp^- with similar steady-state properties

With their substantial similarity as the only two negatively charged acidic amino acids (Figure 32), one should not be overly surprised to find overlap in protein interactions with $Glut^-$ and Asp^-. Compared to $Glut^-$, less is known about Asp^-, but it is more commonly associated with NMDA signalling (Chen et al., 2005 [72]). Previous studies found little worth noting in interactions between Asp^- and VGLUTs: it is not recognised in vesicular uptake assays and does not compete with $Glut^-$ (Naito et al., 1985 [28], Takamori et al., 2001 [73]). Unlike VGLUTs, interactions with Asp^- have been documented with other $Glut^-$ transporters commonly found in neurotransmission. Among these are the aforementioned EAAT1 (referred to as "glutamate aspartate transporter" or GLAST-1 in rats and mice, where it was originally discovered), and a transporter called Sialin, known for its affinity with nitrate and sialic acid (Miyaji et al., 2008 [74]). With 18 ± 3 µM (mean and standard error), EAAT1 even has a higher affinity for Asp^- than for $Glut^-$ with 31 ± 2 µM (Cater et al., 2014 [75]).

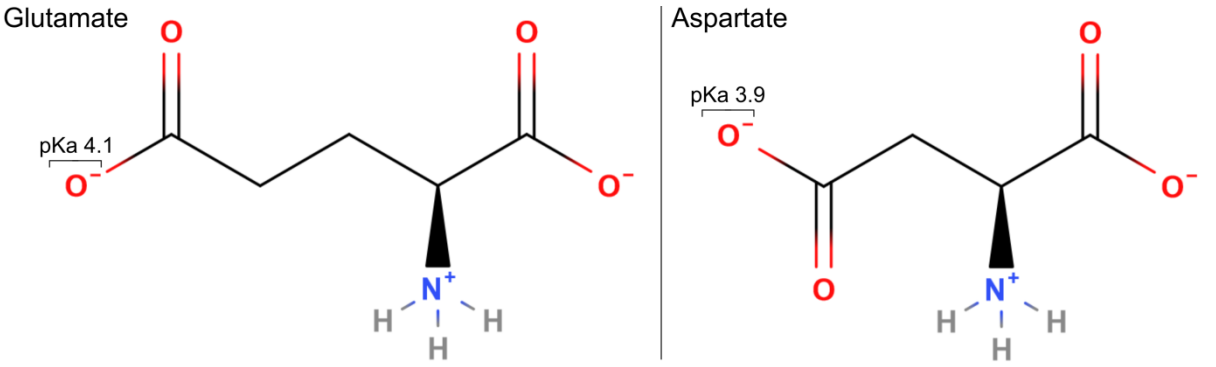

Figure 32: structurally similar amino acid neurotransmitters $Glut^-$ and Asp^-. *Both are depicted with their amino acid backbone in the same position on the right and the acidic head group with its pK_a on the left. Positive electrostatic charge is represented in blue and negative in red, with only full elementary charges in the corresponding colour labelled with a plus or minus, respectively.*

Insights into the way transporters distinguish between $Glut^-$ and Asp^- may provide useful information regarding the intrinsic mechanisms underlying $Glut^-$ transport. Several polyatomic anions were used to test their current through $VGLUT1_{PM}$, primarily while analysing current blocking with Rose Bengal as described in the materials and methods section. Several are likely transported actively, unlike Cl^- and NO_3^-, which are conducted using an apparent channel function. $Glut^-$ and Asp^- are in the polyatomic category, ions that tend to be larger and physiologically the most similar. Contrasting same-condition measurements, $VGLUT1_{PM}$ Asp^- currents are generally similar in their most obvious features (Figure 33). Current traces for both amino acids show less gradual current activation upon

voltage steps than displayed by Cl^- current. This is likely caused at least in part by their lower overall current amplitude, which also leads to the larger relative size of capacitive artefacts compared to other anions. Both have a comparable dependence on pH and [Cl^-] and response to acid activation. However, Asp^- current has a different reversal potential (Figure 33A and B), and its current amplitude changes much slower upon [Cl^-] steps. This activation and deactivation of Asp^- current by external Cl^- is the only active transport with likely biexponential properties observed during fast application measurements discussed here.

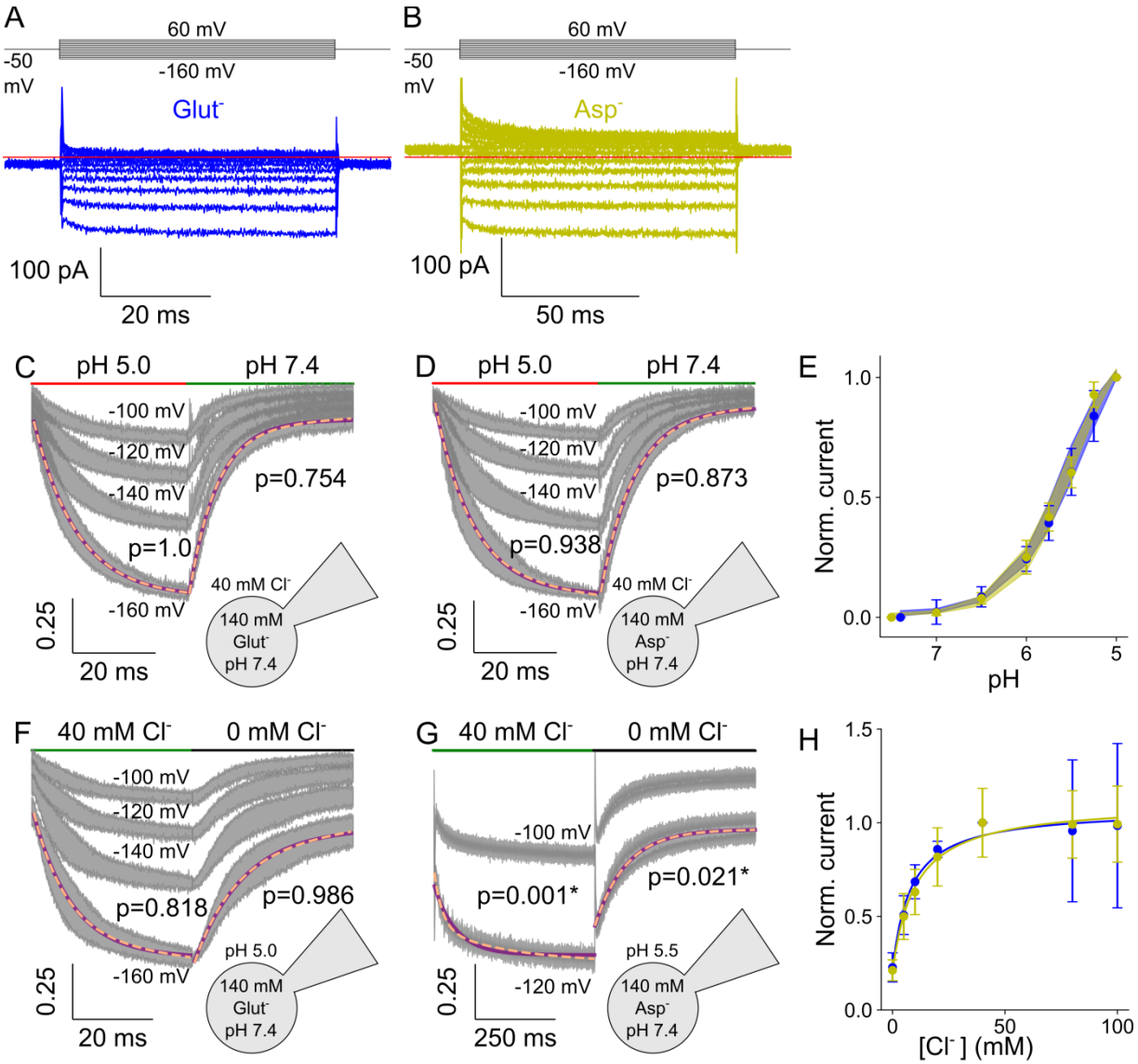

Figure 33: characteristics of $Glut^-$ and Asp^- current. *Representative recordings with voltage jumps from a holding potential of −50 mV, to between −160 and 60 mV for $Glut^-$ (A) and Asp^- (B, capacitive peaks cropped at ±150 mV), pH jumps at a constant 40 mM Cl^- for $Glut^-$ (C, n = 17 for activations and 16 for deactivations) and Asp^- (D, n = 10), steady-state pH dependence (E, at −160 mV, 95% of 10,000 bootstrap samples as a confidence interval), Cl^- jumps at constant pH (not bootstrapped because cells measured at few solutions made it unreliable) for $Glut^-$ (F, n = 10, with pH 5.0) and Asp^- (G, n = 11 for −120 mV and 12 for −100 mV, with pH 5.5) and steady-state Cl^- dependence at pH 5.5 and −140 mV with error bars representing a 95% confidence interval (H, unequal variance due to re-normalisation at 40 mM Cl^-).*

The steady-state current amplitude of both actively transported substrates is roughly similar, at least when contrasted to the Cl^- channel. Quantified current normalised by fluorescence published earlier (Figure 3J of Kolen, Borghans et al. 2023) shows that the current of Asp^- can exceed that of $Glut^-$ at very negative voltages: by up to a factor of 2.3, at −160 mV (pH 5.5, 40 mM Cl^-). Using this 2.3 ratio and the $Glut^-$ transport rate of 561 ± 123 s^{-1} (mean and 95% confidence interval), which were determined at the same pH, [Cl^-], and V, the Asp^- transport rate can be estimated. VGLUT1 would transport 561 × 2.3 = 1290 Asp^- per second if it used the same proton coupling. However, the transport of Asp^- is largely uncoupled, meaning H^+ constitutes far less than 50% of its current, which instead consists almost entirely of Asp^-. Therefore, its actual transport rate may be twice as high, up to 2581 s^{-1}. Asp^- transport out of the cytosol drops off quickly at more positive voltages and becomes less than $Glut^-$ around −80 mV.

A bootstrapped global fit with a sampling of 1000 provides indistinguishable pK_M values of 5.527 ± 0.005 ($Glut^-$, Hill coefficient of 1.3) and 5.542 ± 0.002 (Asp^-, Hill coefficient of 1.4, p = 0.54). The apparent K_M describing the allosteric Cl^- effect was determined to be 8.1 ± 2.0 mM Cl^- for $Glut^-$and 9.9 ± 2.2 mM Cl^- for Asp^-, using the Michaelis-Menten equation with offset fitted to means ± approximate error from covariance. The datasets for $Glut^-$ and Asp^- contain cells measured at few solutions, which makes bootstrapping unreliable. Their K_M values can still be determined to be well below those of Cl^- current with 28.3 ± 0.7 mM, with p = 0.0098 for $Glut^-$ and 0.014 for Asp^-, as calculated using one-sample Wilcoxon signed-rank tests.

$Glut^-$ and Asp^- behave similarly during fast pH application measurements (Figure 34A). The real difference is in the modulation by allosteric Cl^-, where activating current with 40 mM Cl^- appears to have the same primary time constant as $Glut^-$ but gains a pronounced slow exponential process, which causes it to be much slower overall (Figure 34B). Asp^- slows the corresponding deactivation through removal of all external Cl^- down even more, through reduction of the primary time constant rather than the addition of a secondary one. To record this, the Asp^- measurement was extended to the point where the survival of enough cells during the second-long sweep became a concern. Fewer sweeps and a smaller peak voltage of −120 and −100 mV were used instead of the usual range from −160 to 0 or higher. Consequently, no background trace is available to subtract and remove the (likely capacitive) peaks caused by solution exchange. These peaks were excluded from calculations involving these measurements, using only the starting point and post-peak current. These artefacts and the limitations they impose may be responsible for the apparent biexponential features in the activation and deactivation of Asp^- by Cl^-.

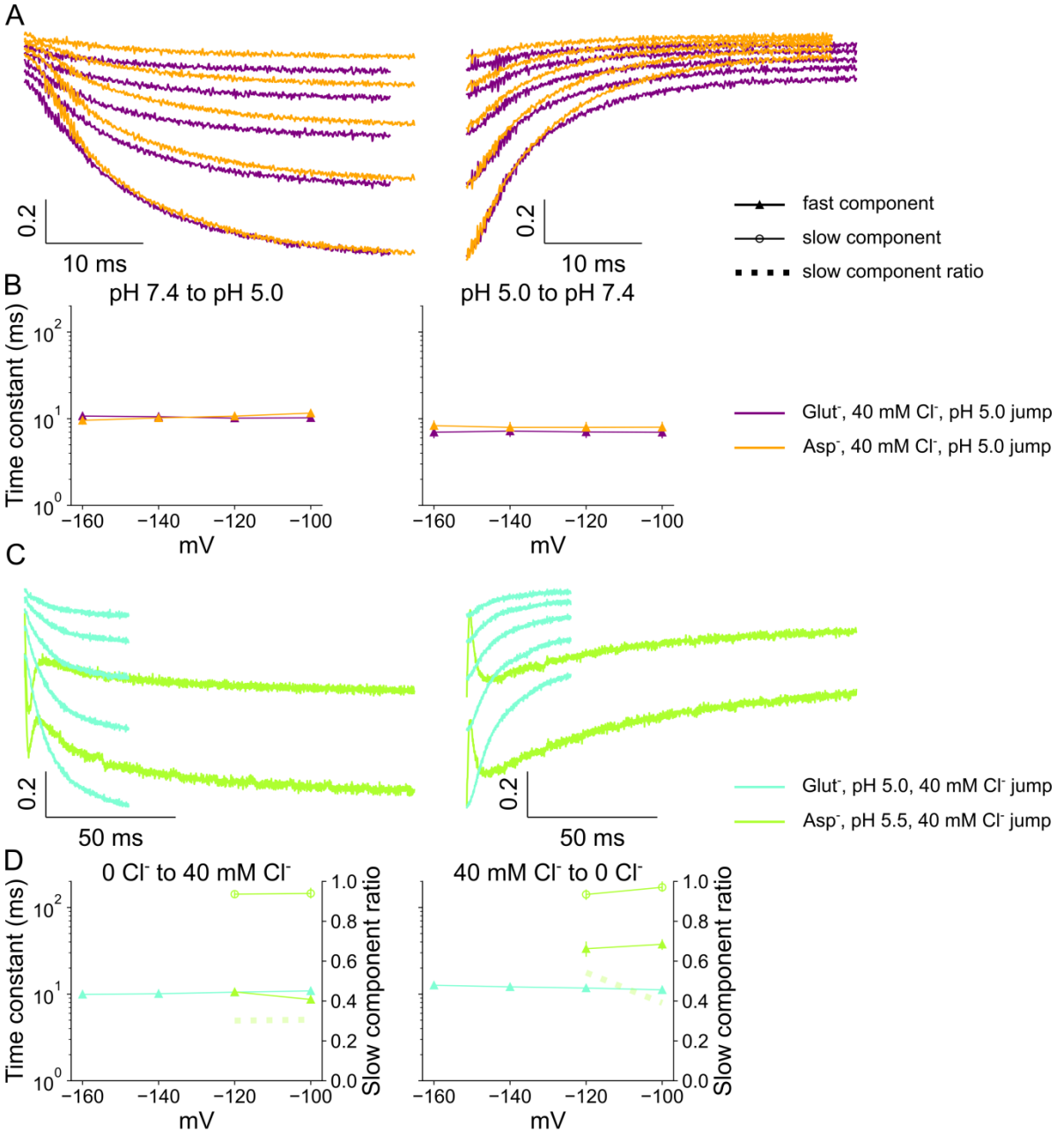

Figure 34: VGLUT1$_{PM}$ Glut$^-$ and Asp$^-$, Cl$^-$ and pH activation and deactivation rates. *Activation and deactivation by applying pH 5.0 and 7.4, respectively (A) with corresponding time constants (B), and activation and deactivation by applying 40 and 0 mM Cl$^-$, respectively (C) with corresponding time constants (D). Data are given as mean, obtained by bootstrapping with a global fit with a sampling of 1000, and 95% of the bootstrapped values as confidence interval error bars.*

3.9 A kinetic model to describe VGLUT1 active transport

The framework used to simulate VGLUT1 Cl$^-$ current was modified, and a different model was developed to simultaneously describe the 1:1 Glut$^-$ proton antiport and uncoupled Asp$^-$ uniport (Figure 35). The Cl$^-$ channel model is free to bind or unbind the ions that modulate it and open as long as it is protonated. In contrast, active transport is modelled using alternating access modes and is more restrictive in the transitions it allows to permit clearly

defined transport cycles. This was used to hypothesise that the second proton (to which $Glut^-$ transport is coupled) binds from the outward-facing side, which enables $Glut^-$ release. Going backward through the transport cycle, this only works if the transition from the inward-facing side carries $Glut^-$ with only the first proton, which suggests that transition with $Glut^-$ and double protonation is restricted. Model symmetry was maintained by placing the unbinding of the second proton directly before the outward transition, along with allowing substrate binding only when doubly protonated to ensure that the coupled proton ends up inside the cell.

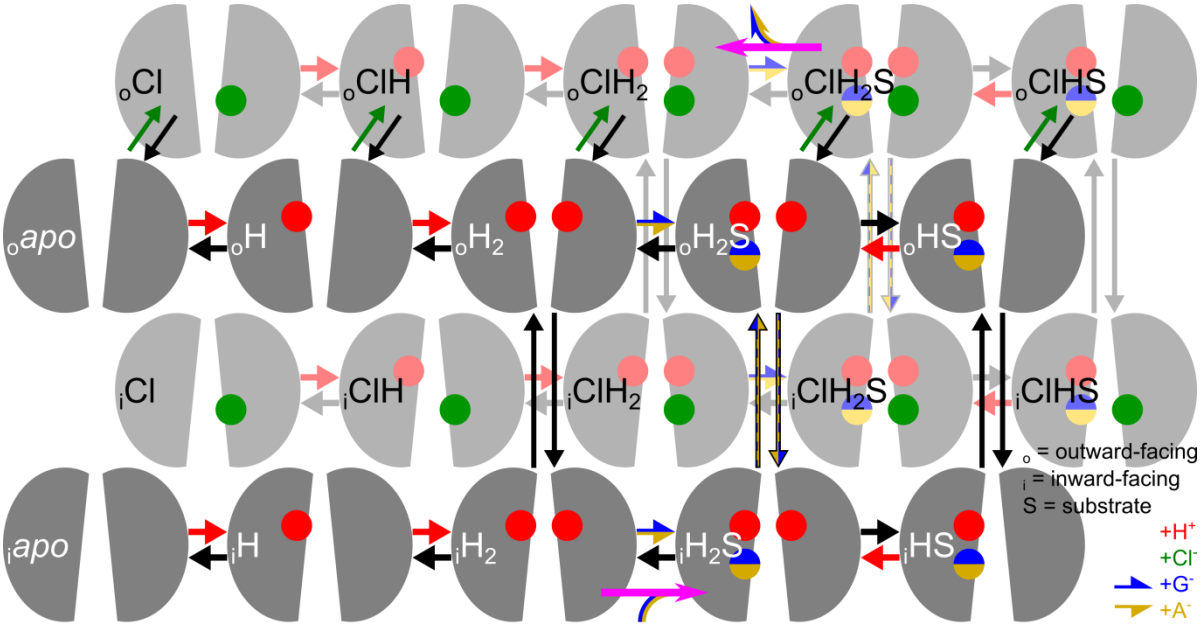

Figure 35: kinetic model describing secondary active $Glut^-$ and Asp^- transport. *States are depicted in either inward ($_i$) or outward-facing ($_o$) conformation with vertical transitions between them in black, protonation in red, and binding of the substrates in blue/yellow. Green arrows depict Cl^- binding from the dark grey front layer to the lighter back layer, but only when the protein faces outward (preventing Cl^- transport). Doubly protonated inward-outward transition is restricted for $Glut^-$. Pink arrows show general transport direction.*

The doubly protonated inward-outward transition is freely available when Asp^- is bound but restricted with $Glut^-$ to ensure proton coupling via the singly protonated pathway. Just like unprotonated channel opening in the Cl^- model, these rate constants are limited to 1 s^{-1}. The remaining rate constants and other parameters can only differ when distinct substrates are bound, so both applications of this model use the same set of values for all states where this is not the case.

3.9.1 Simulating the secondary active VGLUT1 transport of $Glut^-$ and Asp^-

Both substrates are evaluated through separate experimental datasets, using the shared substrate-independent variables plus the ones specific to a substrate. Compatibility is maintained by mutating and optimising all variables as a single overarching set from which

shared and specific parts are combined for each substrate: 13 × 4 shared + 14 × 4 $Glut^-$ + 14 × 4 Asp^- = 164 variables. Optimisation of these variables (shown in Table 8-S) and generation of variants through exploratory mutation produces the simulations below.

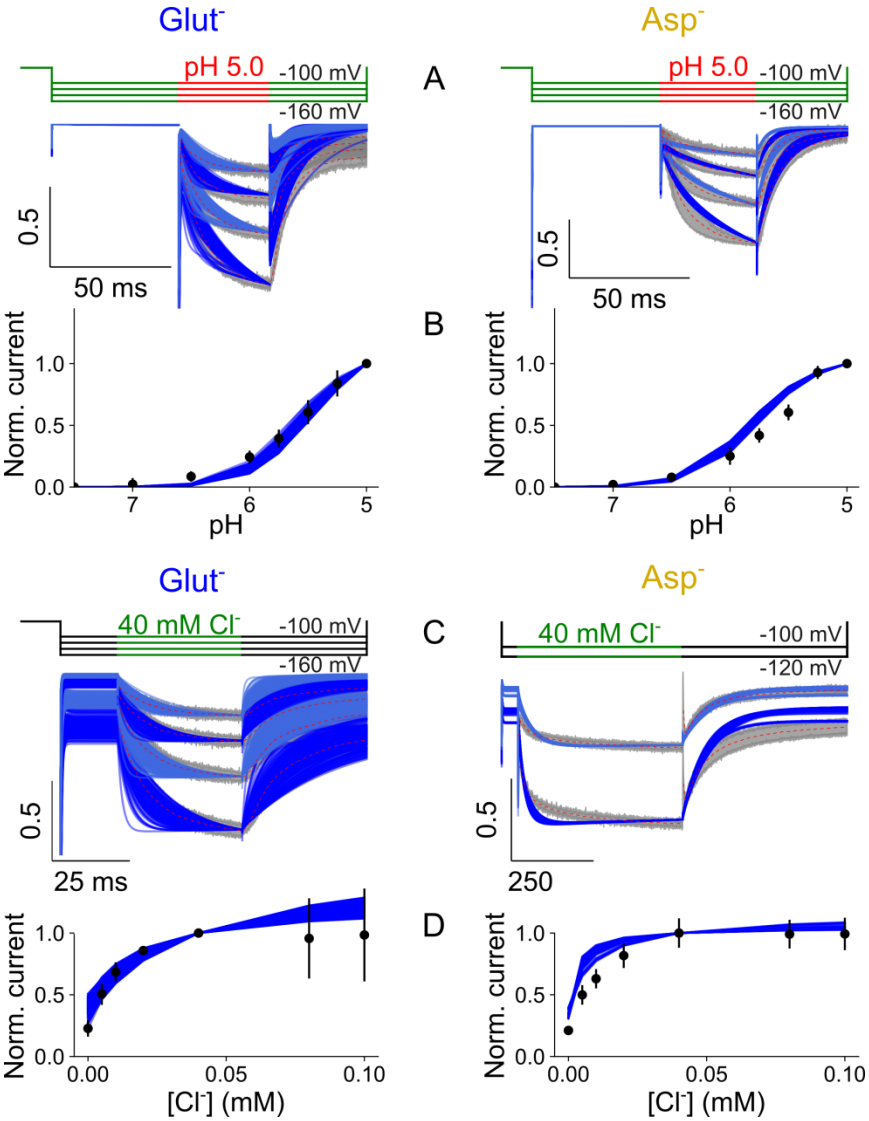

Figure 36: $VGLUT1_{PM}$ $Glut^-$ or Asp^- current and 250 corresponding simulations. *pH jump with $Glut^-$ and Asp^- (A) with the overall pH dependence (B, 40 mM Cl^- and −160 mV) and Cl^- jumps (C, at pH 5.0 for $Glut^-$, pH 5.5 for Asp^-) with the overall Cl^- dependence (D, pH 5.5 and −140 mV). All experimental values are shown in black and the experimental time courses in grey as a 95% confidence interval, with 250 parameter variant simulations in blue. The means of experimental data are additionally shown as dashed red lines to be visible over the wider trace spreads of the simulations.*

3.9.2 Analysis of rates obtained from the modelled VGLUT1 active transport

The $Glut^-$ transport cycle, at pH 5.5, −160 mV, and either 0 or 40 mM Cl^-, can be analysed for each transition in the transport cycle (Figure 37, corresponding *z* and *d* parameters are shown in Figure 49-S).

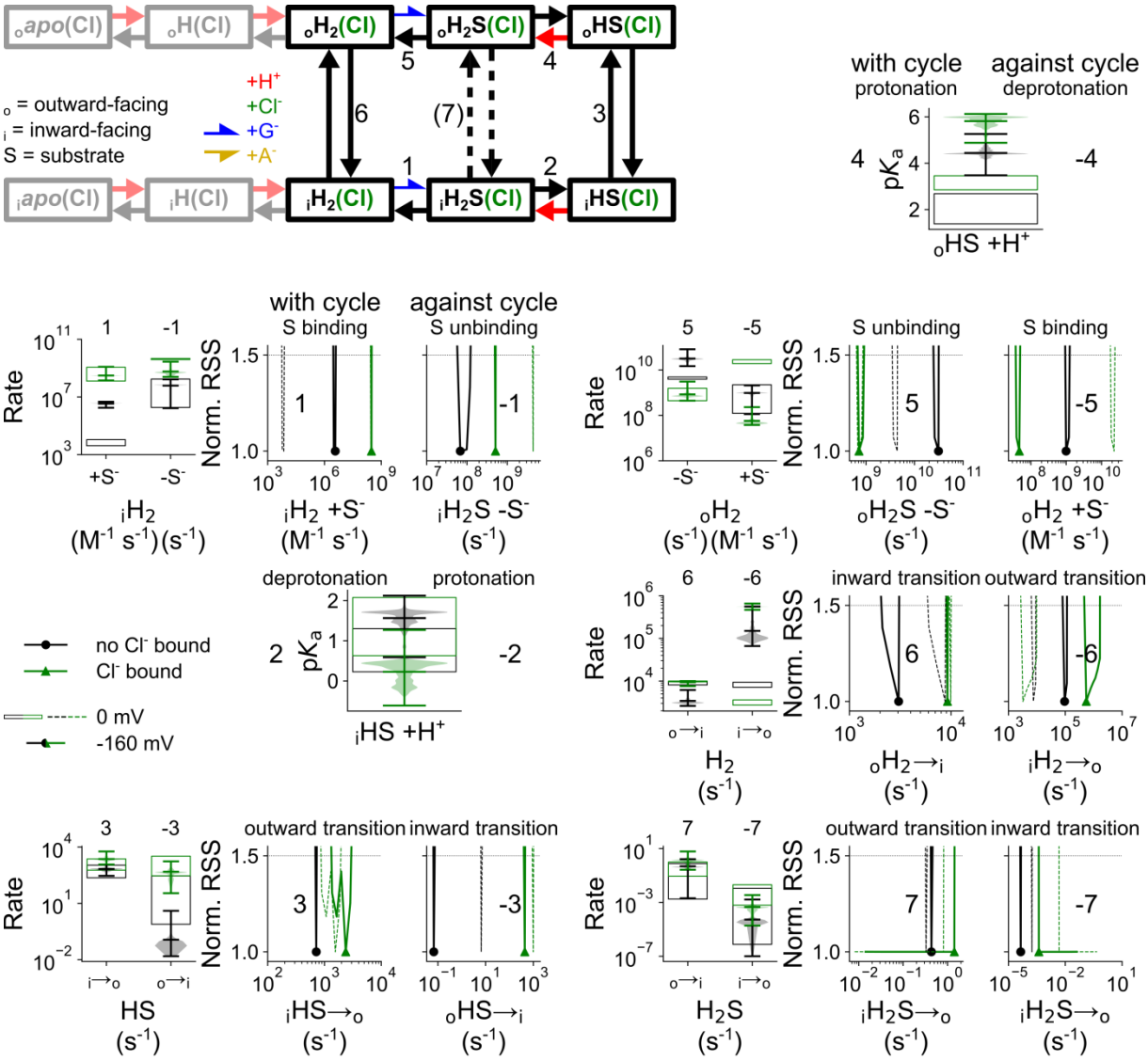

Figure 37: Glut⁻ transport cycle parameters modulated by Cl⁻ binding. *The simplified kinetic scheme has combined Cl⁻-free and Cl⁻-bound states. Steps in the cycle are numbered in the transport direction, starting with substrate binding, corresponding to panels with the same number showing rate amplitudes at −160 mV, protonation steps represented by pK_a values, and all others as exploratory mutation violin plots or normalised RSS representing goodness-of-fit. Transport steps are inward substrate binding (1), inward deprotonation (2), outward transition with single protonation (3), outward protonation (4), outward substrate unbinding (5), substrate-independent outward transition (6), and outward transition with double protonation (7). Dashed arrows show the rate constant of transition step 7 is limited to 1 s^{-1} for Glut⁻. Corresponding* z *and* d *parameters are shown in Figure 49-S.*

Cl^- increases the rate of substrate binding from the cytosol (step 1) from 6.9×10^4 (3.5×10^4–9.1×10^4, median and parameter amplitude range at) M^{-1} s^{-1} to 6.0×10^6 (2.8×10^6–2.4×10^7) M^{-1} s^{-1} in the transport direction, without effect on the reverse rate. The pK_a representing the subsequent inward deprotonation (step 2) is unchanged, and the singly protonated outward transition rate (step 3) is narrowly accelerated from 682 (294–1137) s^{-1} to 2286 (1178–5859) s^{-1}, along with a larger reverse rate increase from 0.07 (0.02–4.01) s^{-1} to 453 (35–1726) s^{-1}. Outward-facing protonation (step 4) is once again unchanged, but the increase in binding affinity of step 1 now reduces outward-facing substrate unbinding (step 5) from 3.1×10^{10}

(1.5×10^{10}–8.1×10^{10}) s^{-1} to a still rapid 7.4×10^{8} (4.4×10^{8}–3.1×10^{9}) s^{-1}, with no change to the binding rate. The inward transition of the empty transporter (step 6) is slightly faster with 9293 (7602–9966) s^{-1} compared to 3152 (2608–6165) s^{-1}, and the restricted singly protonated transition with substrate (step 7) is unchanged. Cl$^-$ appears to promote Glut$^-$ transport primarily by increasing the substrate binding rate, and secondarily speeds up conformational changes. Figure 38 similarly compares the pK_a values and rate constants for Glut$^-$ and Asp$^-$ transport in the Cl$^-$-bound cycle, with the corresponding *z* and *d* parameters shown in Figure 50-S.

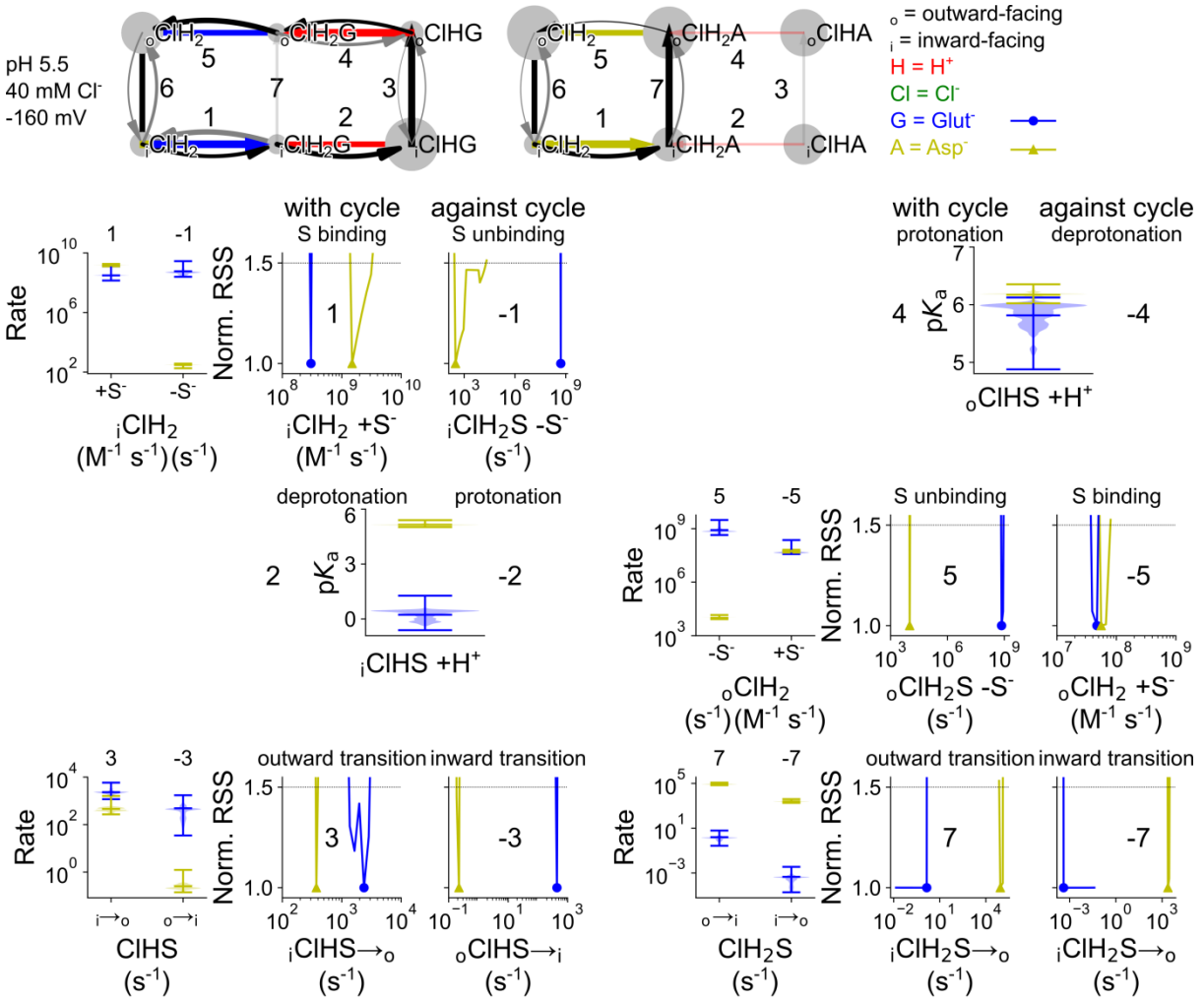

Figure 38: Cl$^-$-bound transport cycle differences between Glut$^-$ and Asp$^-$. *Simplified Cl$^-$-bound transport cycles depict primary substrate pathways with black arrows, state occupancy as grey circle size, and rate amplitude as curved arrow width (both normalised, with amplitude cut-off at 10^{-8} for Glut$^-$ and 10^{-6} for Asp$^-$ to show only the largest rates in the transport direction). The numbered rate amplitudes within this cycle are shown at −160 mV with protonation steps represented by pK_a values and all others as exploratory mutation violin plots or normalised RSS representing goodness-of-fit, starting with inward substrate binding (1), then inward deprotonation (2), outward transition with single protonation (3), outward protonation (4), outward substrate unbinding (5), and outward transition with double protonation (7). The rate constant of the conformational change in step 7 is limited to 1 s^{-1} for Glut$^-$, and the outward transition of step 6 is omitted due to being substrate-independent. Corresponding* z *and* d *parameters are shown in Figure 50-S.*

The doubly protonated transporter is able to bind substrates and, with Asp^- bound, immediate transition outward. $Glut^-$ mostly requires deprotonation before outward transition and re-protonation before release. While both substrates bind at similar rates to the doubly protonated inward-facing transporter (step 1), the unbinding of $Glut^-$ is less stable with a much faster 5.1×10^8 (2.5×10^8–2.8×10^9, median and parameter amplitude range at −160 mV) s^{-1} compared to Asp^- with 309 (181–366) s^{-1}. The pK_a representing inward-facing deprotonation (step 2) is 0.3 (−0.6–1.3) for $Glut^-$-bound transporters and 5.1 (5.0–5.4) with Asp^-. This results in far more deprotonation at the neutral cytosolic pH and a path of preferred proton exchange when $Glut^-$ is bound. Substrate-bound outward translocation in the singly protonated state (step 3) and a pK_a of approximately 6 for outward-facing protonation (step 4) are the same for both substrates. Eventual outward substrate release (step 5) is much faster for $Glut^-$, with 7.4×10^8 (4.4×10^8–3.1×10^9) s^{-1} compared to Asp^- with 1.0×10^4 (8.4×10^3–1.4×10^4) s^{-1}. Return of the empty transporter to the inward-facing conformation (step 6) is independent of the substrate and occurs at the rates shown in Figure 37. Because doubly protonated outward transition (step 7) is restricted with $Glut^-$ with 1.4 (0.3–6.2) s^{-1}, this process is much faster for aspartate with 8.5×10^4 (6.9×10^4–1.2×10^5) s^{-1}. This makes it easier for driving forces other than pH, such as membrane potential, to directly accelerate Asp^- current. This is consistent with its higher current amplitudes at very negative voltages in whole-cell recordings (Kolen et al., 2023 [34]).

Figure 39 compares all association rates for protons and Cl^- in the active transport model. The protonation sites required for the active transport of VGLUT1 appear to be readily accessed from the outward-facing side, both binding protons with a pK_a close to 8 regardless of Cl^- as long as there is no substrate bound (Figure 39A). Figure 39B demonstrates that Cl^- facilitates substrate selectivity in the transport cycle, heavily favouring deprotonation to the cytosol but only when transporting $Glut^-$.

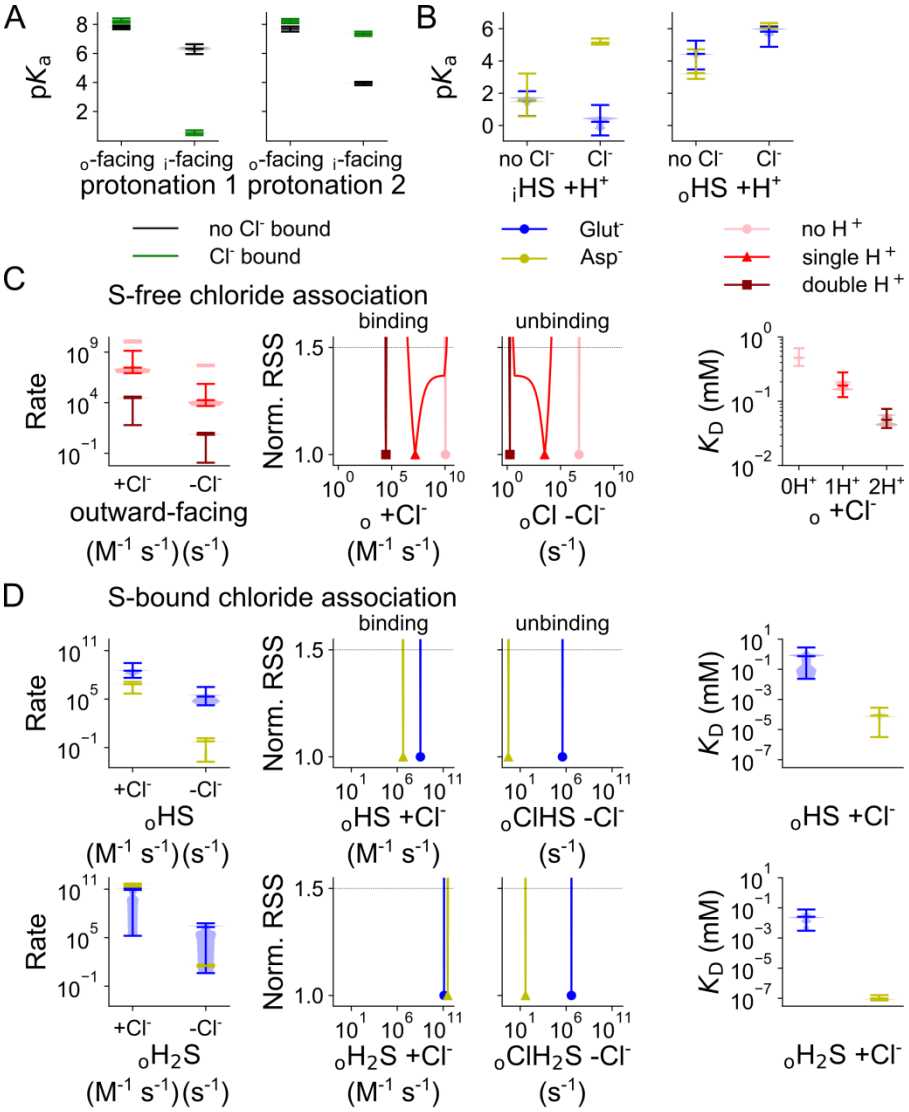

Figure 39: modelled active transport rates for the binding/unbinding of protons and Cl^-. *Proton association as pK_a violin plots generated through exploratory mutation, for substrate-independent rates by Cl^--binding (A) or for substrate-specific rates (B), and exploratory mutation violin plots or normalised RSS representing goodness-of-fit depicting substrate-independent Cl^- binding by protonation (C) or substrate-specific Cl^- association rates (D), all at −160 mV. Corresponding* z *and* d *parameters are shown in Figure 51-S.*

The rates for the binding and unbinding of Cl^- without a substrate decrease with protonation, cumulatively resulting in a minimal K_D and maximal binding stability under double protonation (Figure 39C). For substrate-bound VGLUT1, singly protonated Cl^- binding and unbinding is much slower with bound Asp^-: Cl^- binding at 1.1×10^4 (7.7×10^2–2.2×10^4) M^{-1} s^{-1} and unbinding at 0.529 (0.002–1.433) s^{-1}, versus binding at 5.6×10^5 (6.8×10^4–4.6×10^6) M^{-1} s^{-1} and unbinding at 1.9×10^5 (1.7×10^4–3.1×10^6) s^{-1} with $Glut^-$ (Figure 39D). The result of these changes can be seen in fast Cl^- application experiments (Figure 33F) and imply the existence of an occluded state partially inaccessible to Cl^- in the external solution, which is promoted by the binding of Asp^-. Double protonation makes the Cl^- binding and unbinding rates much closer, but results in far tighter Cl^- binding with a K_D of 9.5×10^{-8} (7.2×10^{-8}–1.6×10^{-7}) mM with Asp^- compared to 0.024 (0.003–0.078) mM with $Glut^-$.

The substrate-bound deprotonation pK_a appears to be important for the difference in transport mechanism and stoichiometry between Glut⁻ and Asp⁻. To test this, the simulation was repeated with different pK_a values via altered unbinding rates in either the inward- or outward-facing conformation. At pH 5.5, 40 mM Cl^-, and −160 mV, the total number of charges transported per second by the kinetic model of VGLUT1 is −1135 ± 1 for Glut⁻ (mean and 95% confidence interval), which includes H^+ flux and amounts to approximately 568 Glut⁻ s^{-1}. Since H^+ exchange is minimal when Asp⁻ is bound, the simulated −2578 ± 3 charges per second can be taken as an estimate of the transport rate of Asp⁻. These transport rates, corresponding to unitary currents of roughly −0.2 and −0.4 fA, respectively (Figure 40A), closely match the empirical transport rates of 561 Glut⁻ s^{-1} and 2581 Asp⁻ s^{-1} that were calculated from fluorescence-normalised current (Kolen et al., 2023 [34]).

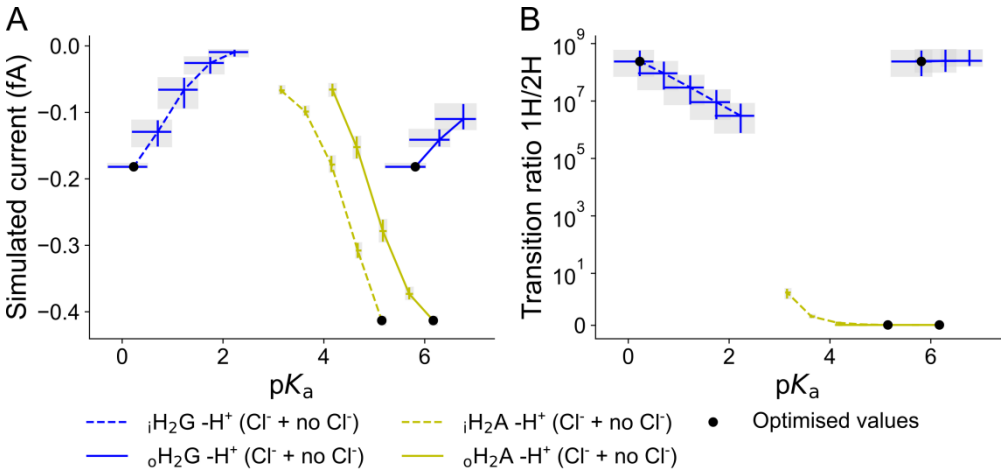

Figure 40: amplitude and H^+ coupling of transport modulated by deprotonation pK_a. *The effect of altering the substrate-bound deprotonation pK_a, up for Glut⁻ and down for Asp⁻, on simulated unitary current at 40 mM Cl^-, pH 5.5, and −160 mV (A) and the overall ratio between singly and doubly protonated outward transition as a metric for proton coupling (B). Black markers show the optimised values; others represent a change by a factor of 3, 10, 30, and 100, with a confidence interval for both their x and y values showing 95% of these metrics for the aforementioned 250 exploratory mutation parameter variants.*

Increasing the low Glut⁻ value and decreasing the high Asp⁻ value also reduces the transport rates, with the inward-facing deprotonation additionally determining the amount of proton coupling, showing the importance of the optimised rates for VGLUT1 function (Figure 40B).

Figure 41 shows time constants fitted to the simulated active transport of VGLUT1. The smaller voltages of the simulated Cl^- dependence of Asp⁻ are less accurate than other results, likely due to the fitting function deeming it largely monoexponential. Aside from this, the simulation of the activation and deactivation of Glut⁻ and Asp⁻ currents by pH and [Cl^-] matches experimental data well.

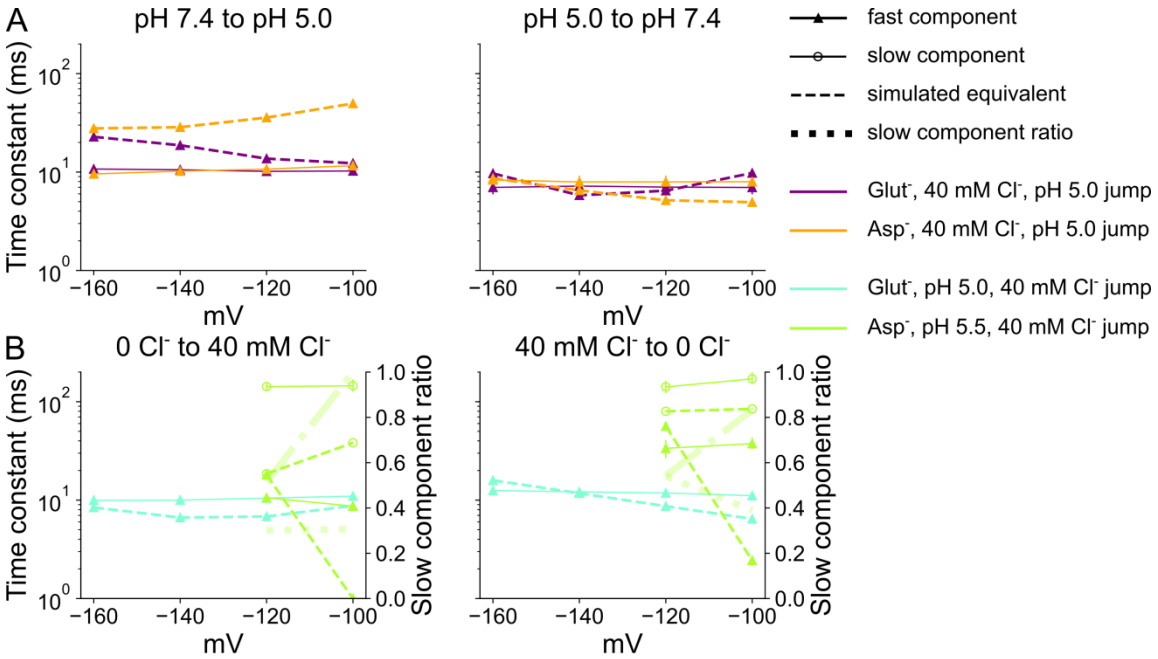

Figure 41: Glut⁻ and Asp⁻ time constants fitted to experimental data and simulation. *Activation or deactivation by pH change or [Cl⁻] change, Data are given as mean, obtained by bootstrapping with a global fit with a sampling of 1000, and 95% of the bootstrapped values as confidence interval error bars, simulation from the same selection of 250 shown in Figure 36.*

4. Conclusions and discussion

4.1 VGLUT1 Cl^- channel gating is modulated by allosteric Cl^- and double sequential protonation

When building kinetic or other Markov models, it is important to only include physiologically relevant factors. In theory, a sufficiently large set of random variables can describe any dataset but risks turning into a black box. These opaque systems may output correct predictions, but their lack of meaningful internal mechanisms or explanations makes them unsuitable for fundamental research. A model with unnecessary variables instead of physiologically selected underpinnings additionally increases the risk of overfitting: replicating the coincidental noise of the data it was trained on too closely, losing its ability to correlate to the actual underlying mechanism or predict anything other than the training data. This is a common problem with the mathematical modelling of incompletely understood processes, including in computational protein biology. In practice, the easiest solution to this problem is to provide the minimum number of realistically relevant factors that allow for a good fit with the data (Chicco, 2017 [76]).

The kinetic description of VGLUT1 channel function relies on a transition between open and closed conformations and its modulation by pH and $[Cl^-]$. The presence of biexponential gating requires access to two opening pathways even in the absence of Cl^-, which is covered by a pair of sequential protonation steps with their own opening transition. Cl^- binding steps account for its allosteric activation. This model is capable of predicting all physiologically relevant parameter interactions between pH, $[Cl^-]$, V, and describes empirical Cl^- current well (Figure 23).

While future findings may restrict Cl^- binding to some states, there is currently no decisive way to determine whether this is justified, so this feature is available to all of them (Figure 22). The model is set up to theoretically permit the removal of excess states and transitions between them, and doing so would not necessarily hamper its ability to represent experimental data. This type of pruning could be performed based on a detailed analysis of the relative importance of pathways in the model but is susceptible to bias and a reliance on insufficiently founded assumptions. These may turn out to be false, and the risks appear to outweigh the potential benefits until more information is available. Without introducing a bias into the result with further and unfounded assumptions, this appears to be the simplest way to model the VGLUT1 channel function with sufficient accuracy.

4.2 External Cl^- allosterically activates VGLUT1 Cl^- current by increasing the initial pK_a and stabilising the open channel

Modification of rate constants in the kinetic model of WT VGLUT1 upon Cl^- association provides insights into the mechanisms underlying channel opening. The pK_a of the initial *apo* state is substantially increased by Cl^- binding, suggesting that anion channel activation is initiated by this allosteric activation under physiological conditions (Figure 25A). This conformation-specific effect suggests that Cl^- binds close to the affected protonation site only in the closed conformation. The negative charge density of the anion provides an attractive electrostatic force, making it easier for the proton to bind (Figure 42, top).

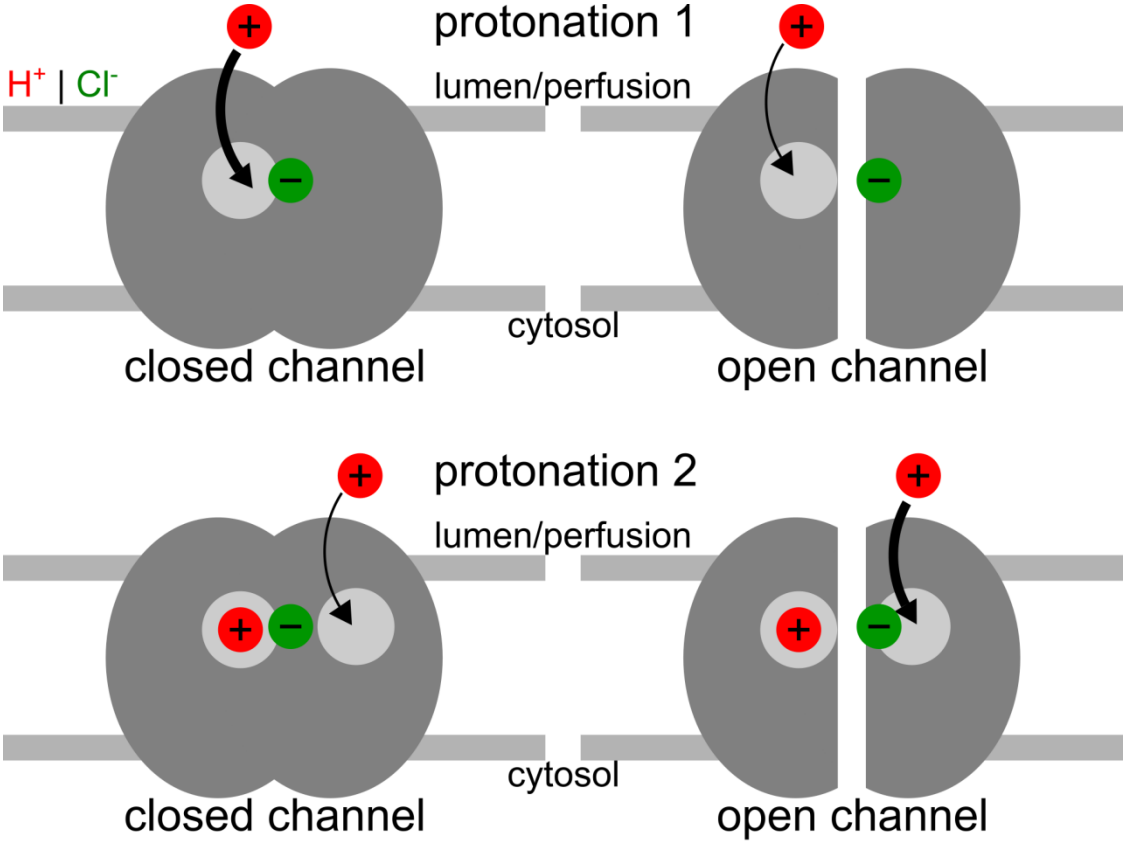

Figure 42: sequential protonation of open and closed Cl^--bound VGLUT1. *Cl^- facilitates the initial protonation of the* apo *state but does not support further protonation unless the channel opens.*

After the initial protonation of the *apo* state, bound Cl^- also supports channel opening of the singly protonated protein. Regardless of protonation, Cl^- stabilises the open state by reducing closing rates, seemingly stabilising this structure (Figure 25B). Unlike the corresponding closed state, Cl^- binding increases the open state pK_a of the second protonation (Figure 42, bottom). This implies a change in the positioning of residues that makes the proton acceptor more accessible in a way that allows the local influence of Cl^- to stabilise the binding site of the second proton, and suggests that both locations are only close together in the open state. Its effect on the stability of the Cl^- channel provides

evidence that modulation by allosteric Cl^- operates through the negative charge it brings to a central position in the positively charged core of the protein.

WT $VGLUT1_{PM}$ mostly opens from a singly protonated open state, and the lowered unbinding rates while the channel is in a protonated open state likely help the Cl^- remain bound (Figure 26). This forms the foundation of the predicted pathway for opening (*apo* → $+Cl^-$ → $+H^+$ → open) into a stable oH state from where it typically closes, as determined by reactive flux calculations (Figure 23L). The protonation of certain residues appears to be a prerequisite for the transport of all physiologically relevant anions that were tested, and the intermediate occupation of doubly protonated open states may be the cause of several of the biexponential gating processes observed in WT $VGLUT1_{PM}$ (Figure 12). The anion channel is likely a required and conserved feature, facilitating the removal of Cl^- in order to reduce the repulsion between the negative charges that accumulate during vesicular $Glut^-$ loading.

4.3 H120A impairs Cl^- association, resulting in protonation without Cl^- and doubly protonated Cl^- channel opening

The positive charge of a protonated histidine is one factor capable of stabilising the binding of anions, and it is likely that histidine 120 in VGLUT1 interacts with the binding pocket of Cl^-. Its absence in H120A explains the decrease in the pK_a of the second protonation of its closed state as well as its reduced Cl^- affinity. The broad increase of its Cl^- dissociation constants is caused by a combination of reduced binding, especially to the closed channel, and increased unbinding regardless of protonation (Figure 31). Neutralisation of the histidine with H120A thus impedes the establishment of a positive charge and hinders the allosteric effect of Cl^-. This finding agrees with computational reports that H128, equivalent to H120 in VGLUT1, plays a critical role in the allosteric regulation of VGLUT2 by supporting the binding of Cl^- to R184 (Rostamipour et al., 2022 [77]).

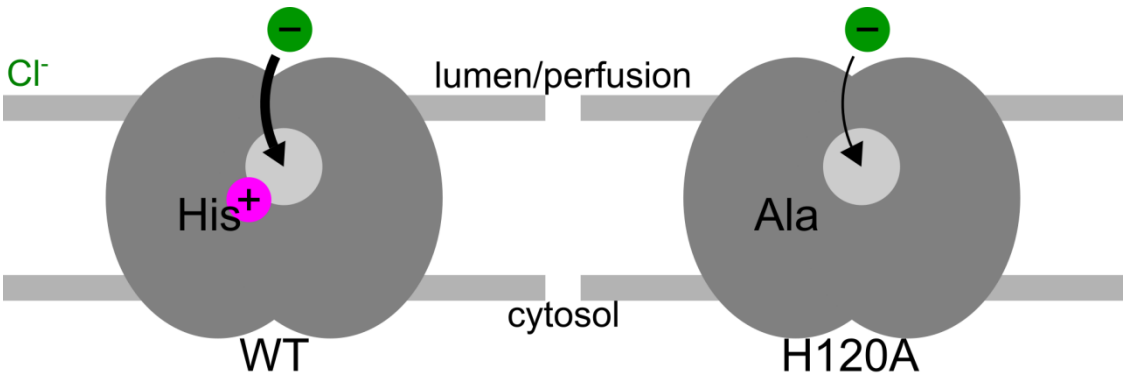

Figure 43: initial Cl^- binding to WT and H120A VGLUT1. *Protonated histidine 120 helps the* apo *state of WT VGLUT1 bind Cl^- well, and neutralisation of this residue in H120A reduces the affinity for Cl^-.*

H120A increases the pK_a of the *apo* state to a value far above the pK_a of even the Cl^--bound WT (Figure 30). This suggests that the first protonation site is close to the residue, as

replacing the typically protonated and therefore positively charged histidine 120 with a neutral alanine would prevent the repulsive effect on positive protons. This serves as an explanation for the mutant having similar gating speeds during Cl^--free pH jumps compared to the WT (Figure 18). The protonation of the *apo* state does not depend on allosteric activation by the charge of Cl^-, which would make the WT faster, and is instead favourable right away (Figure 44). The slight drop in pK_a when Cl^- binds to *apo* H120A may be the result of a shift in the Cl^- binding site that sterically hinders the first protonation.

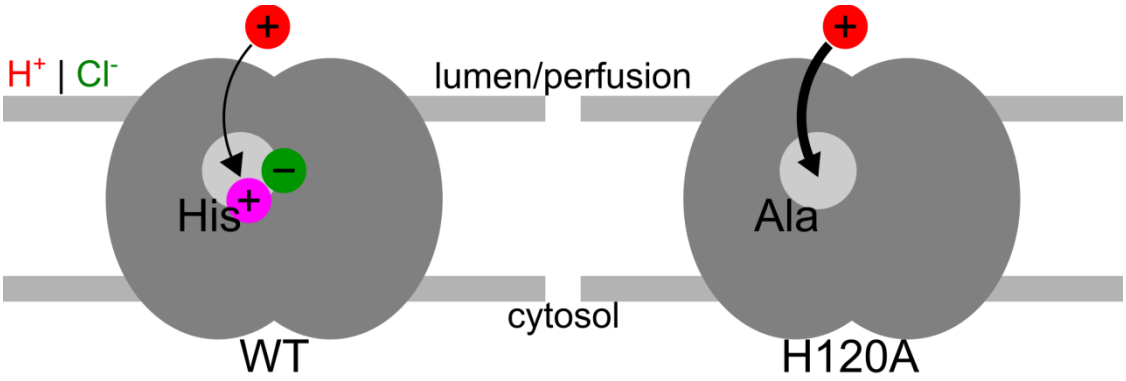

Figure 44: first protonation of Cl^--bound WT and *apo* H120A VGLUT1. Apo *state protonation of VGLUT1 is supported by Cl^- binding in the WT but does not need this allosteric effect when the positive charge of histidine 120 is neutralised.*

Further protonation of the same conformation is more difficult without a negative charge to counteract the positive protons. H120A reduces the second protonation pK_a of the closed state. The second protonation is easier once the protein reaches its open state, facilitating its preference for Cl^--activated doubly protonated channel function. Because the mutation of histidine 120 shifts the opening preference of the channel toward double protonation (Figure 28), it takes longer for H120A to reach stable open states and steady-state current under most conditions. The kinetic model explains the slower channel gating of H120A as the protein spending more time in closed states without Cl^- bound, even when it is available, where its allosteric effect would allow the WT to open faster. The change to protonation rates also explains why the H120A Cl^- channel function activates and deactivates just as fast as the WT upon pH jumps.

4.4 H120A only has a major effect on VGLUT1 pK_M in the absence of Cl^-

At an average pK_M of 5.4, VGLUT1$_{PM}$ consistently produces more anion current with higher luminal [H^+], in agreement with other VGLUT variants. This value is close to the physiological pH in neuronal vesicles, enabling efficient H^+-based modulation of its transport activity *in vivo*. Nearly all conditions tested deviate at most a single decimal point from this value, which indicates the importance of a robust pH sensor to operate consistently in acidic neuronal vesicles. This applies to currents of Cl^-, $Glut^-$, and Asp^- for plasma membrane constructs of

the WT protein with and without external Cl^-, but for H120A only with external Cl^-. Without Cl^-, only the mutant has a significantly lower apparent pK_M of 5.010 ± 0.004 (mean and 95% confidence interval; Figure 27).

VGLUTs seem to exhibit limited H^+ saturation under more conditions than just Cl^--free H120A. This makes accurately determining specific pK_a or pK_M values difficult, requiring measurements at a pH well below the physiological value. Increased overall current naturally increases the variance in measurements: the higher conductance is more likely to induce changes to the environment and also makes existing differences in behaviour more visible. This was used to increase variance due to channel opening (which peaks at an open probability of 0.5 as per Equation 4) in the noise analysis experiment, but can also affect other biological and electronic artefacts (Lei et al., 2020 [78]). These effects consequently decrease the confidence in exact amplitudes measured under such conditions, especially when normalised to a more moderate pH 5.5 from which it can be more easily compared to other measurements.

Aside from this general observation and the fact that pK_a is defined under equilibrium conditions, the problem with low pH measurements determining VGLUT1 pK_a values lies in the fact that many mammalian cells and their derived cell lines have endogenous channels that activate upon external acidification (Zhang et al., 2022 [79]). Experimental results can be skewed in an acidic pH range, roughly below 5, by acid-activated channels such as proton-activated Cl^- (PAC) and other TMEM206-based channels (Ullrich et al., 2019 [80]). Preventing this type of interference requires specific knock-out cell lines to be generated. These need to survive and behave normally for consecutive generations, even though their natural proteome is restricted. On top of this, they need to be validated as stable vectors for other constructs. Such technology should be applied consistently during all related measurements to ensure comparability. At the start of this project, there was insufficient awareness of, and no solutions for, these problems. Although the findings have since been shown to be comparable to those observed in cell lines with PAC knocked out, conclusions based on measured pK_M should be drawn carefully.

4.5 VGLUT1 functions as a Cl^--activated H^+/$Glut^-$ antiporter

Kinetic models for the $Glut^-$ conductance exhibited by $VGLUT1_{PM}$ are centred on the premise of $Glut^-$ transport being proton-coupled (Figure 35). Based on the two protons needed to model the Cl^- channel, VGLUT1 is also assumed to be doubly protonated when functioning as a neurotransmitter transporter. To account for coupled H^+-$Glut^-$ exchange and restrict uncoupled transport, transition between the inward- and outward-facing conformations is severely limited for this substrate. This drives transport via doubly protonated *apo* and singly protonated $Glut^-$-bound conformations. For Asp^- uniport, with no known strict stoichiometry,

both transitions are left unrestricted to allow the simulation to predict a mechanism for the difference in transport mode.

The evolutionary algorithm that optimised the kinetic properties eventually converged on transport behaviour that fits experimental data well (Figure 36). The model is trained to produce higher current amplitudes with Cl^- and does so firstly by substantially increasing $Glut^-$ binding rates under its effect. Secondly, it slightly increases the speed of both (alternating access) conformational changes along the transport cycle (Figure 37). Structural analysis of VGLUT2 identified a likely $Glut^-$ binding site in the pore, in between the positive charges of two arginine residues (R88 and R322) equivalent to R80 and R314 in VGLUT1 (Li et al., 2020 [24]). These arginines reach inward from opposing sides of the pore and can electrostatically hold a large anion with two negatively charged groups, such as carboxylic acids. $Glut^-$ fits snugly between them, and the modelled binding rates suggest that Cl^- induces a conformational change that improves the cytosolic accessibility of this binding site.

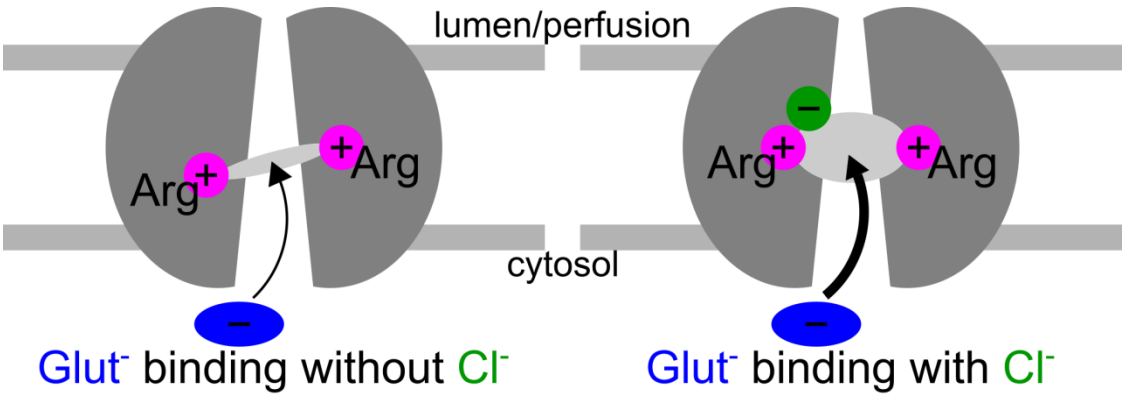

Figure 45: allosteric effect of Cl^-, which opens the $Glut^-$ binding site to the cytosol. *Access to the predicted binding site between the positive charges of two arginines is accelerated when Cl^- is bound to VGLUT1.*

The changes in VGLUT1 caused by the binding of Cl^- also modify a few rates in ways that reduce transport, such as increasing inward transition with $Glut^-$ and inhibiting outward $Glut^-$ unbinding, to a smaller extent. This may explain why Cl^- causes a relatively small change in current amplitude compared to other allosteric factors, and additionally play a role in the biphasic nature of this dependence that reduces current amplitudes at higher [Cl^-] (Naito et al., 1985 [28]).

4.6 The binding of Asp^- modifies VGLUT1 protonation affinity

The only structural difference between $Glut^-$ and Asp^- is the number of methylene carbons separating their carboxyl group from the amino acid backbone (Figure 32). The structures suggest that Asp^- is too short to fit the binding site between R80 and R314 in the same way $Glut^-$ does. Asp^- exhibits a stronger binding to VGLUT1, with a lower unbinding rate (Figure 38). These findings suggest that, instead of being stabilised in the middle, the change in

electrostatic properties causes Asp^- to bind tightly to a single arginine at the side of the pore. This leaves the positive charge of the other arginine available to stabilise the binding of Cl^-, causing the observed increase in Cl^- retention caused by the binding of Asp^-.

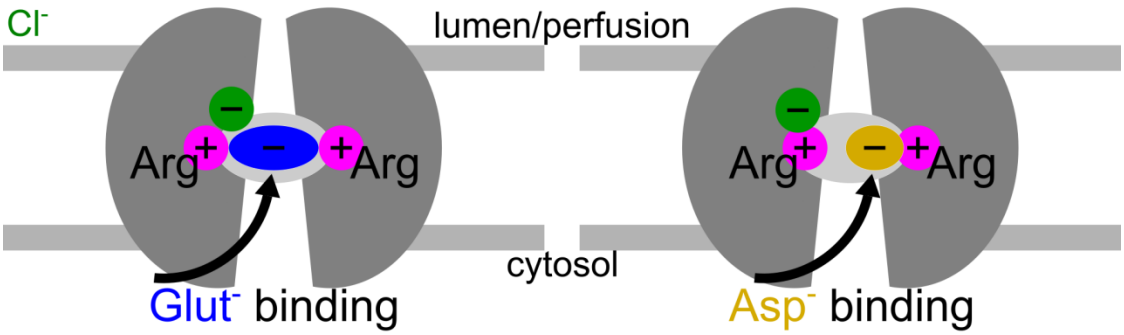

Figure 46: effect of substrate shape on binding locations in the pore of VGLUT1. *$Glut^-$ is expected to bridge two arginines, whereas the shorter Asp^- binds on one side and leaves the other free to stabilise Cl^-.*

With $Glut^-$ bound as its substrate, VGLUT1 tends to unbind a proton in the cytosol before transitioning outward and re-protonating in the lumen. An increase in pK_a, from 0.3 (-0.6–1.3, mean and 95% confidence interval) to 5.1 (5.0–5.4) in the inward-facing conformation, makes this deprotonation far less likely when Asp^- is bound (Figure 38). Its reduced backbone length increases the density of the negative charge its acid group carries, and the strength with which it stabilises the second proton implies that the protonated residue is close to the inward-facing substrate binding site.

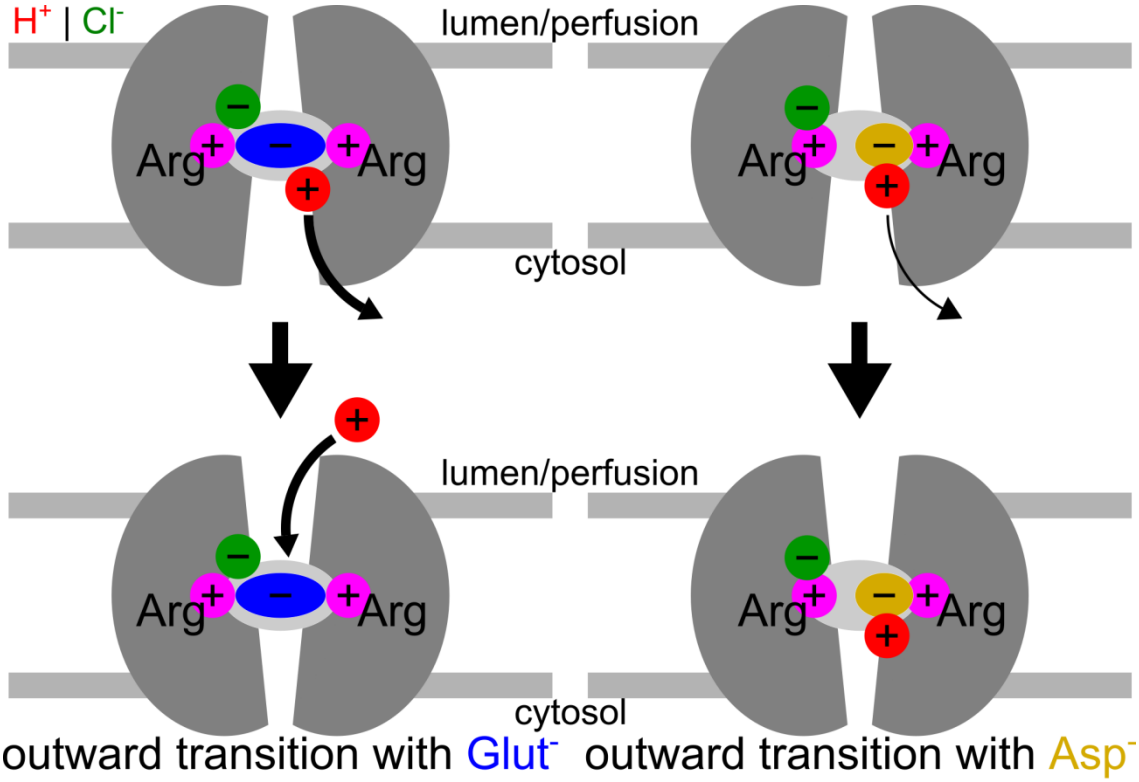

Figure 47: substrate-specific association of the second proton during outward transition. *The negative charge of the larger Glut⁻ substrate is shared between two arginines, while the more localised Asp⁻ helps retain a second proton during conformational change.*

This difference in binding affinity does not exist in the outward-facing conformation, with both substrates promoting protonation with a pK_a of approximately 6, ensuring that Glut⁻ regains and Asp⁻ retains a second proton (Figure 39). This makes Cl⁻ necessary for substrate selectivity. With Asp⁻ the protein remains doubly protonated longer, and from there substrate binding can be directly followed by outward transition. While it is difficult to make judgements on causality, the increased stability of protonation may be what allows VGLUT1 to directly transition with Asp⁻ in the first place.

This explanation fits with the observation that Asp⁻ currents are larger than Glut⁻ at extreme negative voltage amplitudes. Even though Glut⁻ current also includes the flow of protons, larger negative potentials can drive ion flow more efficiently through the reduced number of steps in the Asp⁻ transport cycle. The *in vitro* transport through VGLUTs is likely further exaggerated by the increased concentration of substrates, as there appears to be no indication that neuronal Asp⁻ is more abundant than Glut⁻.

It is not known to play a major role in glutamatergic signalling, which could be different if its concentration were higher, but it seems vesicles are not loaded with significant levels of Asp⁻ under physiological conditions regardless (Kolen et al., 2023 [34]): a continuum model was used to simulate the driving force of this pH gradient on Glut⁻ transport by VGLUT1, in combination with Cl⁻ flux through a channel, as differential equations. The channel open

probability and maximum transport rate were assumed to be voltage-independent, and the pH was kept at 5.5 using proton leak channels. The model accurately described the reported behaviour, quantified as molecule numbers. By comparing this to a corresponding simulation of the uncoupled transport of Asp^-, the coupling itself was determined to be sufficient to explain the selective uptake of $Glut^-$. It seems coupling to the vesicular proton gradient provides a seemingly slower, but physiologically overpoweringly driving force only to $Glut^-$ transport.

4.7 VGLUT1 kinetics suggest different parallel transport mechanisms with limited overlap

Findings regarding various ions transported by $VGLUT1_{PM}$ have played a role in this project. Overall, the plasma membrane mutation has proven itself fairly consistent with previous literature regarding the various aspects of its function. The first simulation was limited to the VGLUT1 Cl^- channel, modulated by different extracellular factors for two constructs. The subsequent kinetic modelling of transport of $Glut^-$ and Asp^- required a rework of the way conductance is calculated. Active transport of the charges of both $Glut^-$ and H^+ across the membrane and Asp^- without H^+ coupling differs strongly from the quantification used for the Cl^- channel, which is based on the distribution of open and closed states.

Kinetic modelling is predicated on the Markov property of stochastic processes not being influenced by past events. VGLUT1 should not have different behaviours for protonation, Cl^--binding, or conformational change before the binding of a substrate. It is theoretically possible for a single kinetic model to describe all conductance properties a protein exhibits, and the presented models could be combined by allowing channel opening only from substrate-free states. However, adding variables and interactions exponentially increases the complexity and data requirement of such models, which then exponentially slows down optimisation and the determining of parameters. While the presented models provide some insight into the mechanisms, the extent to which conducted anions rely on the same residues and pathways remains purely hypothetical. The anion conductance mechanisms of VGLUT1 appear to be varied and explainable, but too convoluted to combine into a single model until more information is gathered. Regardless, the difference in protonation characteristics between both models is consistent with different residues being protonated between both VGLUT1 transport functions (Figure 25 and Figure 39). This implies that they are distinct, and their current properties would not be physiologically representative if connected as-is.

5. Supplementary data

5.1 Number of exponents in VGLUT1$_{PM}$ activation and deactivation

Protein, anion, change	F-test on	Relative slow ratio	F-test off
WT, Cl^-, V jump	0.0048*	0.596, 0.566, 0.543, 0.520	0.2680
WT, Cl^-, V jump	0.0382*	0.590, 0.577, 0.613, 0.625	0.3936
H120A, Cl^-, V jump	0.0322*	0.847, 0.820, 0.795, 0.769	1.0000
H120A, Cl^-, V jump	0.0188*	0.650, 0.628, 0.629, 0.585	1.0000
WT, Cl^-, pH jump	0.0775	0.157, 0.189, 0.223, 0.250	0.0111*
WT, Cl^-, pH jump	0.0076*	0.198, 0.232, 0.267, 0.335	1.0000
H120A, Cl^-, pH jump	0.0342*	0.682, 0.512, 0.439, 0.431	0.0977
H120A, Cl^-, pH jump	0.0612	N/A	1.0000
WT, Cl^-, Cl^- jump	0.0079*	0.272, 0.306, 0.349, 0.354	0.1146
WT, Cl^-, Cl^- jump	0.0133*	0.193, 0.235, 0.292, 0.323	1.0000
H120A, Cl^-, Cl^- jump	0.0516	N/A	0.2761
WT, $Glut^-$, pH jump	1.0000	N/A	0.7536
WT, Asp^-, pH jump	0.9377	N/A	0.8726
WT, $Glut^-$, Cl^- jump	0.8180	N/A	0.9864
WT, $Glut^-$, Cl^- jump	0.0540	N/A	1.0000
WT, Asp^-, Cl^- jump	0.0005*	0.301, 0.306 0.541, 0.391	0.021*

Table 4-S: F-test p-values and relative slow ratio of experimental time course fits. *Function fitting was applied to measurements with the most negative voltage; significantly better biexponential fits are marked with an asterisk (*) with a cut-off at p = 0.05. Voltage jumps differ by 10 mV, all others by 20 mV. Ratio values are horizontally aligned to the corresponding on/off F-test (left for activation, right for deactivation, and two each for Cl^- jumps with Asp^-). Experiments and corresponding values in black are perfused exclusively with solutions that do not contain Cl^-; light green indicates the use of a [Cl^-] of 40 mM, and dark green a [Cl^-] of 140 mM. "N/A" denotes a monoexponential process without a slow ratio.*

5.2 Time constants fitted to VGLUT1$_{PM}$ activation and deactivation

Protein, anion, change	Fast time constants (ms)	Slow time constants (ms)
WT, Cl^-, V jump on	6.9, 6.7, 7.4, 7.6	43.5, 50.0, 55.6, 66.7
WT, Cl^-, V jump off	2.8, 3.3, 4.2, 3.9	N/A
WT, Cl^-, V jump on	1.5, 1.6, 1.6, 1.7	7.6, 8.8, 9.3, 9.6
WT, Cl^-, V jump off	4.0, 4.1, 5.0, 5.1	N/A
H120A, Cl^-, V jump on	9.5, 7.9, 10.0, 9.2	90.9, 100.0, 111.1, 90.9
H120A, Cl^-, V jump off	33.3, 25.6, 25.0, 12.2	N/A
H120A, Cl^-, V jump on	11.5, 11.9, 11.0, 12.2	52.6, 55.6, 58.8, 58.8
H120A, Cl^-, V jump off	12.2, 12.5, 11.5, 9.6	N/A
WT, Cl^-, pH jump on	25.0, 29.4, 34.5, 37.0	N/A
WT, Cl^-, pH jump off	6.7, 6.0, 5.1, 3.5	66.7, 58.8, 47.6, 34.5
WT, Cl^-, pH jump on	5.9, 6.2, 6.4, 6.0	34.5, 32.3, 27.0, 29.4
WT, Cl^-, pH jump off	3.7, 3.7, 3.6, 3.8	N/A
H120A, Cl^-, pH jump on	6.1, 7.4, 6.4, 3.6	40.0, 37.0, 45.5, 22.7

H120A, Cl^-, pH jump off	6.6, 5.9, 5.5, 5.3	N/A
H120A, Cl^-, pH jump on	17.9, 16.4, 15.9, 14.5	N/A
H120A, Cl^-, pH jump off	5.8, 5.4, 5.1, 5.0	N/A
WT, Cl^-, Cl^- jump on	5.7, 6.3, 6.5, 7.0	35.7, 43.5, 38.5, 47.6
WT, Cl^-, Cl^- jump off	13.5, 12.8, 11.9, 11.5	N/A
WT, Cl^-, Cl^- jump on	4.0, 4.2, 4.4, 4.6	45.5, 25.6, 23.8, 27.8
WT, Cl^-, Cl^- jump off	10.5, 10.2, 10.1, 9.6	N/A
H120A, Cl^-, Cl^- jump on	21.3, 19.6, 18.2, 16.1	N/A
H120A, Cl^-, Cl^- jump off	20.4, 17.2, 14.7, 12.8	N/A
WT, $Glut^-$, pH jump on	10.5, 10.4, 10.1, 10.0	N/A
WT, $Glut^-$, pH jump off	6.9, 7.1, 6.9, 6.9	N/A
WT, Asp^-, pH jump on	9.3, 9.9, 10.4, 11.2	N/A
WT, Asp^-, pH jump off	8.2, 7.8, 7.9, 7.9	N/A
WT, $Glut^-$, Cl^- jump on	9.7, 9.8, 10.2, 10.5	N/A
WT, $Glut^-$, Cl^- jump off	12.3, 12.0, 11.6, 11.0	N/A
WT, $Glut^-$, Cl^- jump on	4.6, 4.3, 4.4, 4.3	N/A
WT, $Glut^-$, Cl^- jump off	6.7, 6.0, 5.6, 4.9	N/A
WT, Asp^-, Cl^- jump on*	10.5, 8.6	142.9, 142.9
WT, Asp^-, Cl^- jump off*	33.3, 37.0	142.9, 166.7

Table 5-S: time constants fitted to the most negative voltages in 20 mV steps. *Slow components are shown where a biexponential fit was significantly better as determined by F-testing (Table 4-S). Experiments and corresponding values in black are perfused exclusively with solutions that do not contain Cl^-; light green indicates the use of a [Cl^-] of 40 mM, and dark green a [Cl^-] of 140 mM. The asterisk-marked Cl^- jumps with Asp^- (*) were recorded at fewer voltages and could consequently not have solution change artefacts removed, resulting in reduced confidence in the exponential resolution of its rates. "N/A" denotes a monoexponential process without slow rates.*

5.3 Optimised kinetic parameters for the Cl^- model

WT, Cl^- current	**Rate constant**	**Reverse rate constant**	***z* (e)**	***d***
closed (*apo*), protonation 1	2.26×10^{8} s^{-1}	9.26×10^{5} s^{-1}	0.5134	0.9922
closed H, protonation 2	8.62×10^{8} s^{-1}	7.48×10^{2} s^{-1}	−0.8101	0.1373
open, protonation 1	4.95×10^{9} s^{-1}	7.19×10^{3} s^{-1}	−0.1450	0.0122
open H, protonation 2	7.97×10^{8} s^{-1}	3.11×10^{3} s^{-1}	0.8802	0.4811
closed Cl, protonation 1	1.51×10^{9} s^{-1}	5.85×10^{4} s^{-1}	0.9119	0.7206
closed ClH, protonation 2	4.87×10^{9} s^{-1}	2.88×10^{3} s^{-1}	−0.7656	0.7472
open Cl, protonation 1	4.83×10^{9} s^{-1}	3.54×10^{4} s^{-1}	0.0394	0.9990
open ClH, protonation 2	1.69×10^{8} s^{-1}	5.93 s^{-1}	0.3075	0.9646
apo, opening	1.00 s^{-1}	1.32×10^{3} s^{-1}	−0.3278	0.1912
H, opening	1.37×10^{2} s^{-1}	6.38×10^{1} s^{-1}	−0.9862	0.9736
H_2, opening	2.12×10^{3} s^{-1}	4.46×10^{3} s^{-1}	0.7041	0.7684
Cl, opening	1.00 s^{-1}	1.17×10^{-3} s^{-1}	−0.1130	0.3306
ClH, opening	4.12×10^{2} s^{-1}	9.11×10^{-2} s^{-1}	−0.9856	0.9269
ClH_2, opening	4.16×10^{1} s^{-1}	5.48×10^{-4} s^{-1}	0.0876	0.9991
apo, Cl^- binding	4.98×10^{9} s^{-1}	6.29×10^{7} s^{-1}	−0.4133	0.0119

closed H, Cl^- binding	1.38×10^4 s^{-1}	1.65 s^{-1}	−0.0147	0.0347
closed H_2, Cl^- binding	8.88×10^7 s^{-1}	7.21×10^3 s^{-1}	0.0297	0.6099
open, Cl^- binding	3.69×10^9 s^{-1}	2.54×10^9 s^{-1}	−0.1226	0.5012
open H, Cl^- binding	3.31×10^8 s^{-1}	1.15×10^9 s^{-1}	0.0618	0.0917
open H_2, Cl^- binding	4.17×10^9 s^{-1}	1.31×10^8 s^{-1}	−0.5109	0.0144

Table 6-S: modelled WT VGLUT1$_{PM}$ Cl^- current rate constant, *z*, and *d* amplitudes. *Binding steps and bound ions are shown in red for protons and green for Cl^-.*

H120A, Cl^- current	**Rate constant**	**Reverse rate constant**	***z* (*e*)**	***d***
closed (*apo*), protonation 1	7.32×10^8 s^{-1}	7.88×10^4 s^{-1}	0.1686	0.5009
closed H, protonation 2	1.29×10^9 s^{-1}	1.18×10^2 s^{-1}	0.0086	0.1624
open, protonation 1	2.95×10^9 s^{-1}	3.50×10^3 s^{-1}	−0.2266	0.8712
open H, protonation 2	2.39×10^8 s^{-1}	1.25×10^3 s^{-1}	0.9583	0.9993
closed Cl, protonation 1	4.99×10^9 s^{-1}	6.59×10^5 s^{-1}	0.3560	0.6793
closed ClH, protonation 2	4.98×10^9 s^{-1}	2.43×10^3 s^{-1}	−0.2697	0.8423
open Cl, protonation 1	1.27×10^8 s^{-1}	2.59×10^3 s^{-1}	0.7151	0.4965
open ClH, protonation 2	4.70×10^8 s^{-1}	1.20×10^1 s^{-1}	−0.0967	0.8788
apo, opening	9.36×10^{-1} s^{-1}	1.74×10^2 s^{-1}	−0.0694	0.9343
H, opening	5.29×10^1 s^{-1}	1.08×10^2 s^{-1}	−0.4647	0.1494
H_2, opening	3.61×10^1 s^{-1}	4.21×10^3 s^{-1}	0.4850	0.6315
Cl, opening	1.18×10^{-1} s^{-1}	8.80×10^{-1} s^{-1}	−0.8295	0.3306
ClH, opening	8.40×10^2 s^{-1}	9.72×10^2 s^{-1}	−0.4704	0.2274
ClH_2, opening	1.73×10^1 s^{-1}	1.05 s^{-1}	−0.2975	0.9991
apo, Cl^- binding	2.98×10^9 s^{-1}	3.38×10^9 s^{-1}	−0.5598	0.3190
closed H, Cl^- binding	1.74×10^4 s^{-1}	2.42×10^4 s^{-1}	−0.3725	0.4418
closed H_2, Cl^- binding	6.62×10^8 s^{-1}	4.90×10^9 s^{-1}	−0.6507	0.3362
open, Cl^- binding	2.91×10^8 s^{-1}	7.21×10^8 s^{-1}	−0.2906	0.6533
open H, Cl^- binding	1.07×10^8 s^{-1}	4.56×10^9 s^{-1}	0.6512	0.4770
open H_2, Cl^- binding	4.78×10^3 s^{-1}	9.95×10^2 s^{-1}	−0.4039	0.0144

Table 7-S: modelled H120A VGLUT1$_{PM}$ Cl^- current rate constant, *z*, and *d* amplitudes. *Binding steps and bound ions are shown in red for protons and green for Cl^-.*

5.4 Optimised kinetic parameters for the active transport model

$Glut^-$/Asp^- transport	**Rate constant**	**Reverse rate constant**	***z* (*e*)**	***d***
$_i$, protonation 1	1.10×10^9 s^{-1}	1.00×10^3 s^{-1}	−0.1542	0.8510
$_i$H, protonation 2	2.94×10^8 s^{-1}	1.64×10^7 s^{-1}	−0.9968	5×10^{-8}
$_i$$H_2$, transition to $_o$	7.53×10^3 s^{-1}	8.76×10^3 s^{-1}	−0.5700	0.7060
$_o$H, protonation 2	1.47×10^8 s^{-1}	1.00×10^3 s^{-1}	−0.9236	0.1722
$_o$, protonation 1	1.49×10^8 s^{-1}	1.00×10^3 s^{-1}	−0.9649	0.9931
$_i$Cl, protonation 1	1.39×10^9 s^{-1}	3.67×10^8 s^{-1}	0.0226	0.7430
$_i$ClH, protonation 2	8.58×10^8 s^{-1}	1.00×10^3 s^{-1}	−0.5163	0.9987
$_i$ClH_2, transition to $_o$	3.21×10^3 s^{-1}	9.93×10^3 s^{-1}	−0.8287	0.9860
$_o$ClH, protonation 2	3.72×10^8 s^{-1}	1.00×10^3 s^{-1}	−0.9631	0.2655

$_{o}$Cl, protonation 1	9.49×10^{8} s^{-1}	1.00×10^{3} s^{-1}	−0.8142	0.0105
$_{o}$H$_2$, Cl$^-$ binding	1.00×10^{3} s^{-1}	6.38 s^{-1}	−0.2256	0.1031
$_{o}$H, Cl$^-$ binding	6.20×10^{5} s^{-1}	1.00×10^{4} s^{-1}	−0.1861	0.0317
$_{o}$, Cl$^-$ binding	4.34×10^{8} s^{-1}	4.46×10^{7} s^{-1}	−0.3368	0.0062
$_{i}$H$_2$, Glut$^-$ binding	1.00×10^{3} s^{-1}	6.88×10^{7} s^{-1}	−0.9959	0.9986
$_{i}$HG, protonation 2	2.85×10^{9} s^{-1}	3.84×10^{8} s^{-1}	−0.3117	0.5904
$_{i}$HG, transition to $_{o}$	7.16×10^{2} s^{-1}	6.50 s^{-1}	−0.7275	0.0002
$_{o}$HG, protonation 2	4.41×10^{9} s^{-1}	3.49×10^{7} s^{-1}	−0.8462	0.8150
$_{o}$H$_2$, Glut$^-$ binding	1.40×10^{8} s^{-1}	4.41×10^{9} s^{-1}	0.3120	0.0031
$_{i}$ClH$_2$, Glut$^-$ binding	3.92×10^{7} s^{-1}	4.38×10^{9} s^{-1}	−0.3548	0.0365
$_{i}$ClHG, protonation 2	1.32×10^{9} s^{-1}	5.72×10^{7} s^{-1}	0.3283	0.3824
$_{i}$ClHG, transition to $_{o}$	1.55×10^{3} s^{-1}	9.92×10^{2} s^{-1}	−0.1965	0.3414
$_{o}$ClHG, protonation 2	4.97×10^{9} s^{-1}	1.98×10^{6} s^{-1}	−0.9578	0.8616
$_{o}$ClH$_2$, Glut$^-$ binding	3.17×10^{9} s^{-1}	6.77×10^{8} s^{-1}	0.9912	0.9907
$_{o}$HG, Cl$^-$ binding	3.75×10^{7} s^{-1}	3.21×10^{4} s^{-1}	0.5653	0.2922
$_{o}$H$_2$G, Cl$^-$ binding	5.00×10^{9} s^{-1}	2.16×10^{5} s^{-1}	0.4536	0.0003
$_{i}$H$_2$G, transition to $_{o}$	3.27×10^{-1} s^{-1}	1.74×10^{-4} s^{-1}	−0.2621	0.1697
$_{i}$ClH$_2$G, transition to $_{o}$	8.07×10^{-1} s^{-1}	4.75×10^{-3} s^{-1}	−0.4827	0.1859
$_{i}$H$_2$, Asp$^-$ binding	6.01×10^{5} s^{-1}	8.49×10^{5} s^{-1}	−0.0518	0.1549
$_{i}$HA, protonation 2	5.54×10^{8} s^{-1}	1.99×10^{8} s^{-1}	−0.3738	0.0692
$_{i}$HA, transition to $_{o}$	1.97×10^{2} s^{-1}	3.04×10^{2} s^{-1}	−0.9498	0.2251
$_{o}$HA, protonation 2	4.93×10^{9} s^{-1}	1.14×10^{9} s^{-1}	−0.9422	0.1306
$_{o}$H$_2$, Asp$^-$ binding	3.09×10^{9} s^{-1}	3.75×10^{9} s^{-1}	1.0000	0.9951
$_{i}$ClH$_2$, Asp$^-$ binding	1.84×10^{7} s^{-1}	1.00×10^{3} s^{-1}	−0.5723	0.6742
$_{i}$ClHA, protonation 2	3.98×10^{9} s^{-1}	1.00×10^{3} s^{-1}	0.5408	0.9997
$_{i}$ClHA, transition to $_{o}$	1.82×10^{1} s^{-1}	2.37×10^{-1} s^{-1}	−0.4913	0.9779
$_{o}$ClHA, protonation 2	1.00×10^{8} s^{-1}	1.00×10^{3} s^{-1}	−0.4346	4×10^{-5}
$_{o}$ClH$_2$, Asp$^-$ binding	1.10×10^{8} s^{-1}	1.00×10^{3} s^{-1}	0.7896	0.5335
$_{o}$HA, Cl$^-$ binding	1.00×10^{3} s^{-1}	1.11 s^{-1}	−0.9436	0.8707
$_{o}$H$_2$A, Cl$^-$ binding	8.67×10^{8} s^{-1}	4.16×10^{1} s^{-1}	−0.4360	0.9674
$_{i}$H$_2$A, transition to $_{o}$	2.20×10^{2} s^{-1}	2.19×10^{2} s^{-1}	−0.5182	0.0049
$_{i}$ClH$_2$A, transition to $_{o}$	6.38×10^{3} s^{-1}	3.31×10^{3} s^{-1}	−0.4668	0.8902

Table 8-S: rate constant, *z*, and *d* amplitudes of the WT VGLUT1$_{PM}$ active transport model. *Binding steps and bound ions are shown in red for protons, green for Cl$^-$, blue for Glut$^-$, and yellow for Asp$^-$.*

5.5 Amplitude of the *z* and *d* variables for WT and H120A VGLUT1 Cl^- model

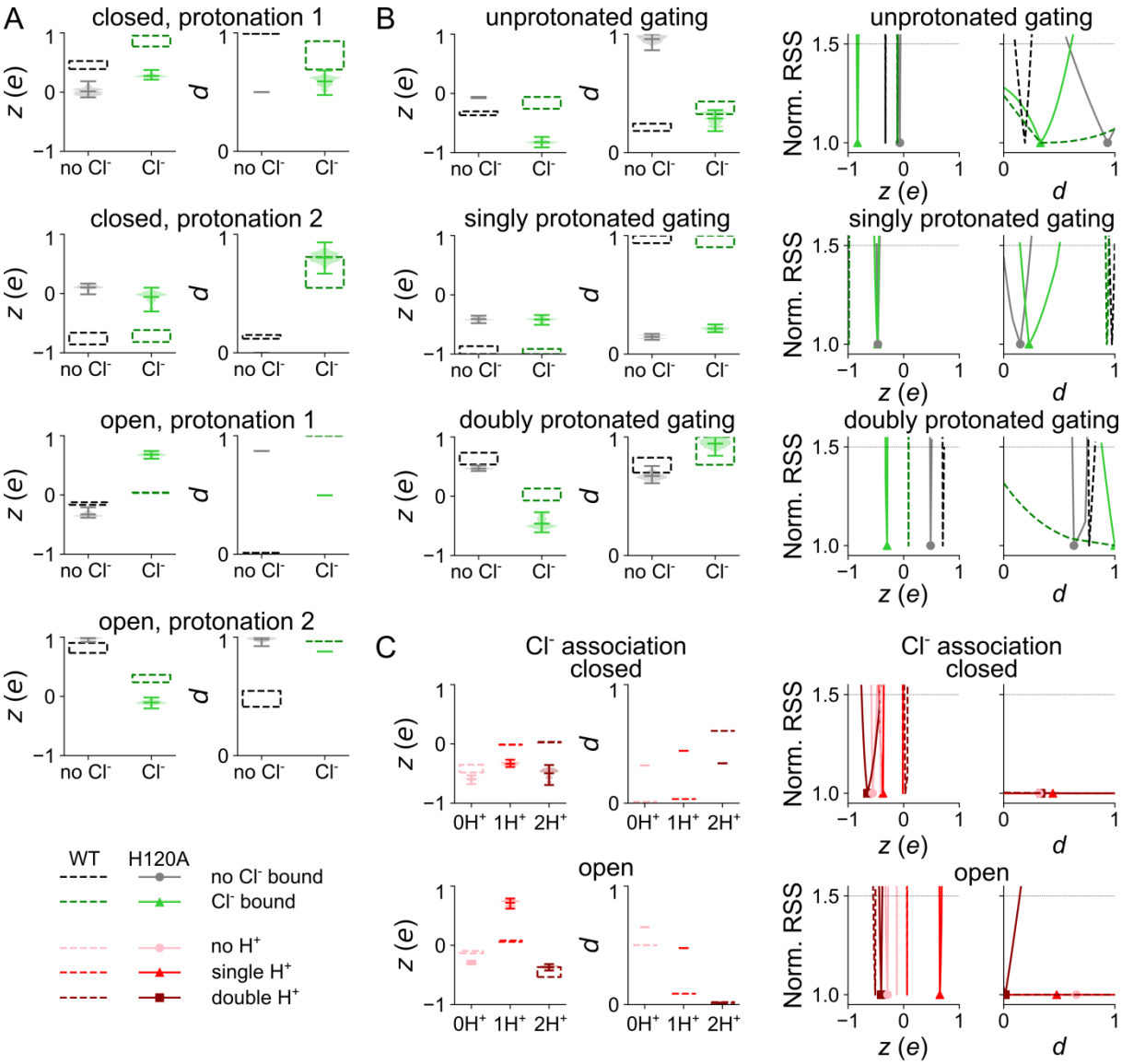

Figure 48-S: charge movement and symmetry of Cl^- channel protonation and opening. *Parameters for simulated pK_a modulated by external Cl^- shown as violin plots (A), and transitions between open and closed states modulated by external Cl^- (B) or Cl^- association modulated by protonation (C) depicted as exploratory mutation violin plots or normalised RSS representing goodness-of-fit corresponding to the data in Figure 25, Figure 26, Figure 30, and Figure 31.*

5.6 Cl^--based amplitude of the *z* and *d* variables of $Glut^-$ transport

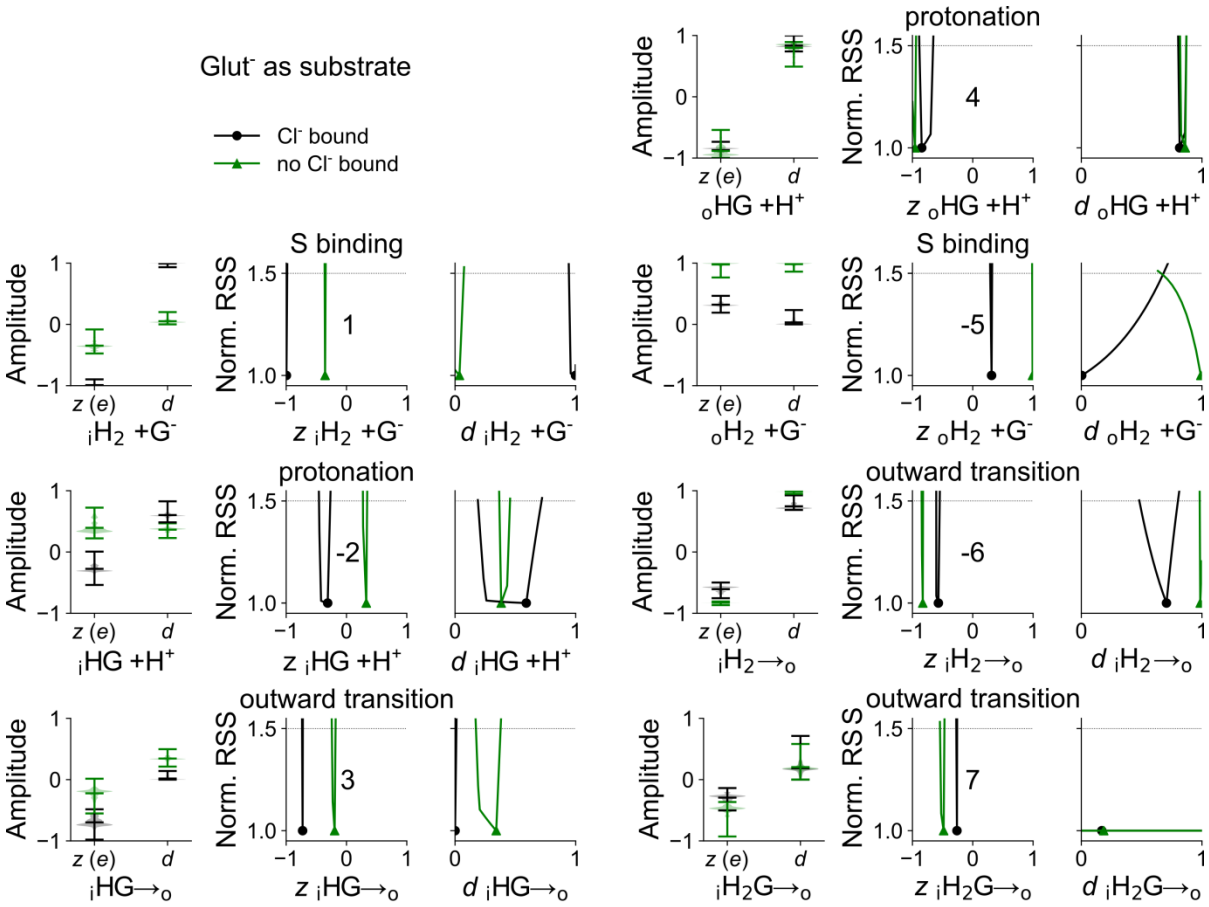

Figure 49-S: charge movement and symmetry of the modelled $Glut^-$ transport cycle. *Parameters for inward substrate binding (1), inward deprotonation (2), outward transition with single protonation (3), outward protonation (4), outward substrate unbinding (5), substrate-independent outward transition (6), and outward transition with double protonation (7) are depicted as exploratory mutation violin plots or normalised RSS representing goodness-of-fit corresponding to the data in Figure 37.*

5.7 Substrate-based amplitude of the *z* and *d* variables of Cl^--bound transport

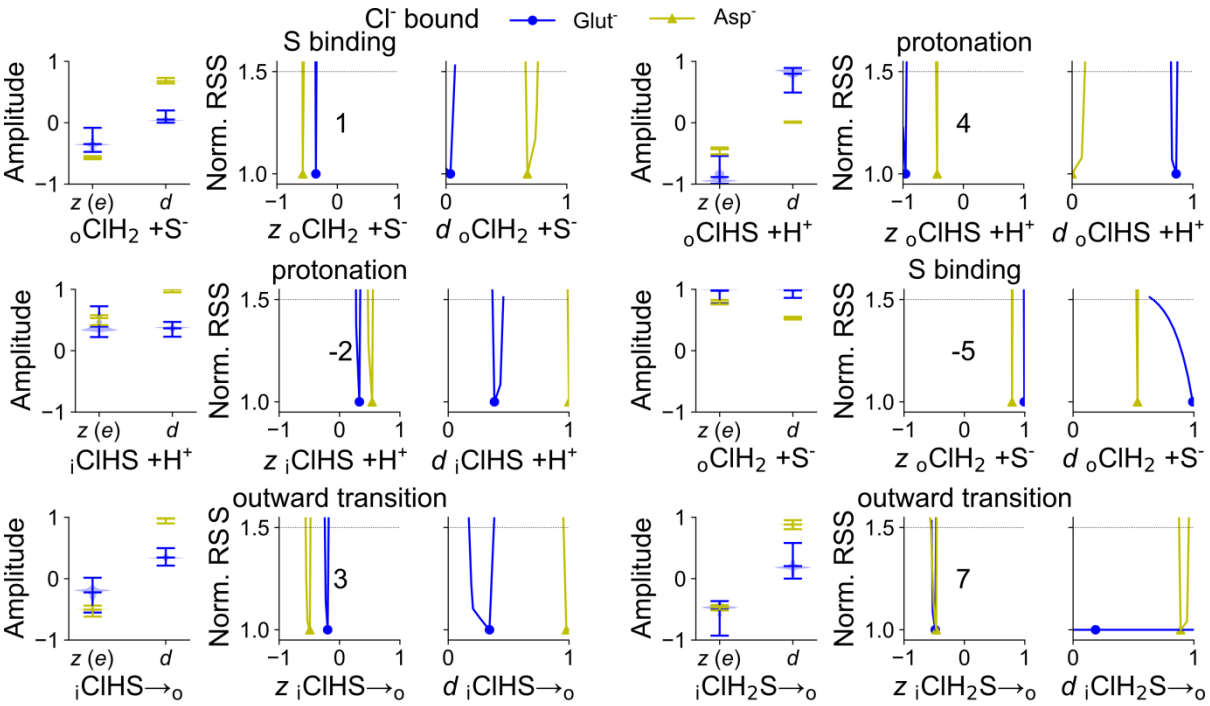

Figure 50-S: charge movement and symmetry of $Glut^-$ and Asp^- transport cycles with Cl^-. *Parameters for inward substrate binding (1), inward deprotonation (2), outward transition with single protonation (3), outward protonation (4), outward substrate unbinding (5), and outward transition with double protonation (7) are depicted as exploratory mutation violin plots or normalised RSS representing goodness-of-fit corresponding to the data in Figure 38. The outward transition of step 6 is omitted due to being substrate-independent.*

5.8 Amplitude of the *z* and *d* variables of proton and Cl^- association in the $Glut^-$ and Asp^- model

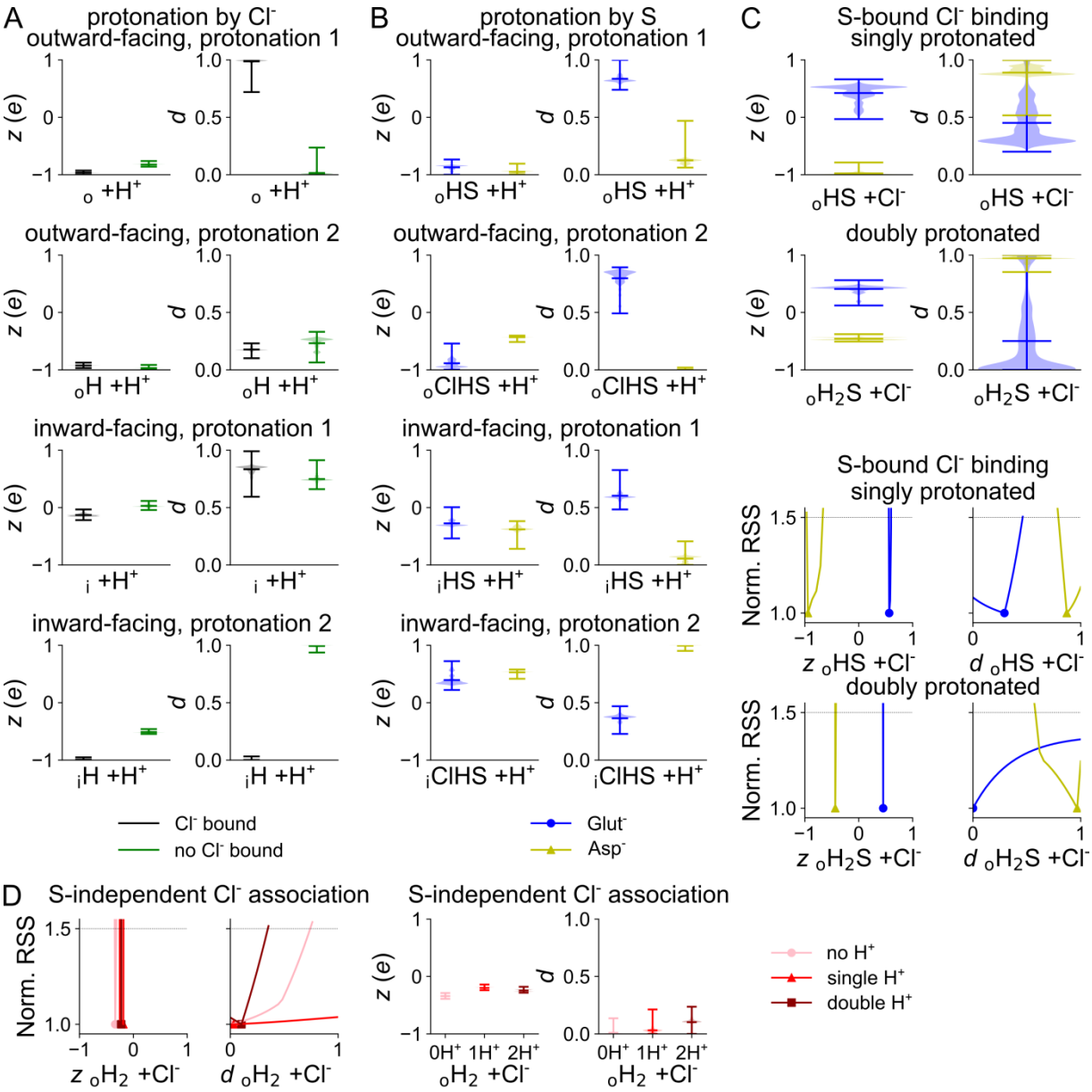

Figure 51-S: charge movement and symmetry of active transport H^+ and Cl^- association. *Exploratory mutation violin plots depicting parameters for substrate-independent protonation (A) or substrate-specific protonation (B), and exploratory mutation violin plots or normalised RSS representing goodness-of-fit for the parameters of substrate-specific Cl^- binding (C) or substrate-independent Cl^- binding (D) corresponding to the data in Figure 39.*

6. References

1. Lopez-Munoz F, Boya J, Alamo C. Neuron theory, the cornerstone of neuroscience, on the centenary of the Nobel Prize award to Santiago Ramon y Cajal. *Brain Res Bull.* 2006;70(4-6):391-405.

2. Nickel M. Kinetics and rhythm of body contractions in the sponge Tethya wilhelma (Porifera: Demospongiae). *J Exp Biol.* 2004;207(Pt 26):4515-4524.

3. Sakarya O, Armstrong KA, Adamska M, et al. A Post-Synaptic Scaffold at the Origin of the Animal Kingdom. *Plos One.* 2007;2(6).

4. Han Y, Kebschull JM, Campbell RAA, et al. The logic of single-cell projections from visual cortex. *Nature.* 2018;556(7699):51-56.

5. Loewi O. Über humorale übertragbarkeit der Herznervenwirkung. *Pflügers Arch.* 1921;189:239–242.

6. Meldrum BS. Glutamate as a neurotransmitter in the brain: Review of physiology and pathology. *J Nutr.* 2000;130(4):1007s-1015s.

7. Rusakov DA. Ca2+-dependent mechanisms of presynaptic control at central synapses. *Neuroscientist.* 2006;12(4):317-326.

8. Platt SR. The role of glutamate in central nervous system health and disease--a review. *Vet J.* 2007;173(2):278-286.

9. Maren S, Tocco G, Standley S, Baudry M, Thompson RF. Postsynaptic factors in the expression of long-term potentiation (LTP): increased glutamate receptor binding following LTP induction in vivo. *Proc Natl Acad Sci U S A.* 1993;90(20):9654-9658.

10. Contractor A, Swanson GT, Sailer A, O'Gorman S, Heinemann SF. Identification of the kainate receptor subunits underlying modulation of excitatory synaptic transmission in the CA3 region of the hippocampus. *J Neurosci.* 2000;20(22):8269-8278.

11. Hardingham GE, Fukunaga Y, Bading H. Extrasynaptic NMDARs oppose synaptic NMDARs by triggering CREB shut-off and cell death pathways. *Nat Neurosci.* 2002;5(5):405-414.

12. Carvajal FJ, Mattison HA, Cerpa W. Role of NMDA Receptor-Mediated Glutamatergic Signaling in Chronic and Acute Neuropathologies. *Neural Plast.* 2016;2016:2701526.

13. Shigemoto R, Kinoshita A, Wada E, et al. Differential presynaptic localization of metabotropic glutamate receptor subtypes in the rat hippocampus. *J Neurosci.* 1997;17(19):7503-7522.

14. Fahlke C, Kortzak D, Machtens JP. Molecular physiology of EAAT anion channels. *Pflugers Arch.* 2016;468(3):491-502.

15. Anderson CM, Swanson RA. Astrocyte glutamate transport: Review of properties, regulation, and physiological functions. *Glia.* 2000;32(1):1-14.

16. Zerangue N, Kavanaugh MP. Flux coupling in a neuronal glutamate transporter. *Nature.* 1996;383(6601):634-637.

17. Mim C, Balani P, Rauen T, Grewer C. The glutamate transporter subtypes EAAT4 and EAATs 1-3 transport glutamate with dramatically different kinetics and voltage dependence but share a common uptake mechanism. *J Gen Physiol.* 2005;126(6):571-589.

18. Cisneros IE, Ghorpade A. Methamphetamine and HIV-1-induced neurotoxicity: role of trace amine associated receptor 1 cAMP signaling in astrocytes. *Neuropharmacology.* 2014;85:499-507.

19. Martinez-Hernandez A, Bell KP, Norenberg MD. Glutamine synthetase: glial localization in brain. *Science.* 1977;195(4284):1356-1358.

20. Lau A, Tymianski M. Glutamate receptors, neurotoxicity and neurodegeneration. *Pflugers Arch.* 2010;460(2):525-542.

21. Danbolt NC. Glutamate uptake. *Prog Neurobiol.* 2001;65(1):1-105.

22. Reimer RJ. SLC17: a functionally diverse family of organic anion transporters. *Mol Aspects Med.* 2013;34(2-3):350-359.

23. Fremeau RT, Jr., Voglmaier S, Seal RP, Edwards RH. VGLUTs define subsets of excitatory neurons and suggest novel roles for glutamate. *Trends Neurosci.* 2004;27(2):98-103.

24. Li F, Eriksen J, Finer-Moore J, et al. Ion transport and regulation in a synaptic vesicle glutamate transporter. *Science.* 2020;368(6493):893-897.

25. Juge N, Yoshida Y, Yatsushiro S, Omote H, Moriyama Y. Vesicular glutamate transporter contains two independent transport machineries. *J Biol Chem.* 2006;281(51):39499-39506.

26. Egashira Y, Takase M, Takamori S. Monitoring of Vacuolar-Type H ATPase-Mediated Proton Influx into Synaptic Vesicles. *Journal of Neuroscience.* 2015;35(8):3701-3710.

27. Miesenböck G. Visualizing secretion and synaptic transmission with pH-sensitive green fluorescent proteins. *Nature.* 1998;394(6689):192-195.

28. Naito S, Ueda T. Characterization of glutamate uptake into synaptic vesicles. *J Neurochem.* 1985;44(1):99-109.

29. Preobraschenski J, Cheret C, Ganzella M, et al. Dual and Direction-Selective Mechanisms of Phosphate Transport by the Vesicular Glutamate Transporter. *Cell Rep.* 2018;23(2):535-545.

30. Eriksen J, Li F, Edwards RH. The mechanism and regulation of vesicular glutamate transport: Coordination with the synaptic vesicle cycle. *Biochim Biophys Acta Biomembr.* 2020;1862(12):183259.

31. Farsi Z, Preobraschenski J, van den Bogaart G, Riedel D, Jahn R, Woehler A. Single-vesicle imaging reveals different transport mechanisms between glutamatergic and GABAergic vesicles. *Science.* 2016;351(6276):981-984.

32. Farsi Z, Jahn R, Woehler A. Proton electrochemical gradient: Driving and regulating neurotransmitter uptake. *Bioessays.* 2017;39(5).

33. Martineau. VGLUT1 functions as a glutamate/proton exchanger with chloride channel activity in hippocampal glutamatergic synapses. *Nature Communications.* 2017;8.

34. Kolen B, Borghans B, Kortzak D, et al. Vesicular glutamate transporters are H(+)-anion exchangers that operate at variable stoichiometry. *Nat Commun.* 2023;14(1):2723.

35. Pietrancosta N, Djibo M, Daumas S, El Mestikawy S, Erickson JD. Molecular, Structural, Functional, and Pharmacological Sites for Vesicular Glutamate Transporter Regulation. *Mol Neurobiol.* 2020;57(7):3118-3142.

36. Burger PM, Mehl E, Cameron PL, et al. Synaptic vesicles immunoisolated from rat cerebral cortex contain high levels of glutamate. *Neuron.* 1989;3(6):715-720.

37. Takamori S, Holt M, Stenius K, et al. Molecular anatomy of a trafficking organelle. *Cell.* 2006;127(4):831-846.

38. Omote H, Miyaji T, Juge N, Moriyama Y. Vesicular neurotransmitter transporter: bioenergetics and regulation of glutamate transport. *Biochemistry.* 2011;50(25):5558-5565.

39. Maycox PR, Hell JW, Jahn R. Amino acid neurotransmission: spotlight on synaptic vesicles. *Trends Neurosci.* 1990;13(3):83-87.

40. Hille. *Ion Channels of Excitable Membranes.* Sinauer Associates; 2001.

41. Chay TR. Kinetic modeling for the channel gating process from single channel patch clamp data. *J Theor Biol.* 1988;132(4):449-468.

42. Hodgkin AL, Huxley AF, Katz B. Measurement of current-voltage relations in the membrane of the giant axon of Loligo. *J Physiol.* 1952;116(4):424-448.

43. Foss SM, Li H, Santos MS, Edwards RH, Voglmaier SM. Multiple dileucine-like motifs direct VGLUT1 trafficking. *J Neurosci.* 2013;33(26):10647-10660.

44. Eriksen J, Chang R, McGregor M, Silm K, Suzuki T, Edwards Robert H. Protons Regulate Vesicular Glutamate Transporters through an Allosteric Mechanism. *Neuron.* 2016;90(4):768-780.

45. Hillen W, Berens C. Mechanisms underlying expression of Tn10 encoded tetracycline resistance. *Annu Rev Microbiol.* 1994;48:345-369.

46. Sakmann B, Neher E. Patch clamp techniques for studying ionic channels in excitable membranes. *Annu Rev Physiol.* 1984;46:455-472.

47. Zielen AJ. The Elimination of Liquid Junction Potentials With the Glass Electrode. *J Phys Chem.* 1963;67(7):1474–1479.

48. Bagur R, Hajnoczky G. Intracellular Ca(2+) Sensing: Its Role in Calcium Homeostasis and Signaling. *Mol Cell.* 2017;66(6):780-788.

49. Vormann J. Magnesium: Nutrition and Homoeostasis. *AIMS Public Health.* 2016;3(2):329-340.

50. Osei-Owusu J, Yang J, Vitery MDC, Qiu Z. Molecular Biology and Physiology of Volume-Regulated Anion Channel (VRAC). *Curr Top Membr.* 2018;81:177-203.

51. Ogita K, Hirata K, Bole DG, et al. Inhibition of vesicular glutamate storage and exocytotic release by Rose Bengal. *Journal of Neurochemistry.* 2008;77(1):34-42.

52. Cannell MB, Nichols CG. Effects of pipette geometry on the time course of solution change in patch clamp experiments. *Biophys J.* 1991;60(5):1156-1163.

53. Smith DO, Franke C, Rosenheimer JL, Zufall F, Hatt H. Desensitization and resensitization rates of glutamate-activated channels may regulate motoneuron excitability. *J Neurophysiol.* 1991;66(4):1166-1175.

54. Gray PT. Analysis of whole cell currents to estimate the kinetics and amplitude of underlying unitary events: relaxation and 'noise' analysis. In: *Microelectrode Techniques: The Plymouth Workshop Handbook.* Cambridge: The Company of Biologists Ltd; 1999:189–207.

55. Ehrenstein G, Lecar H, Nossal R. The nature of the negative resistance in bimolecular lipid membranes containing excitability-inducing material. *J Gen Physiol.* 1970;55(1):119-133.

56. Sigworth FJ. The variance of sodium current fluctuations at the node of Ranvier. *J Physiol.* 1980;307:97-129.

57. Alvarez O, Gonzalez C, Latorre R. Counting channels: a tutorial guide on ion channel fluctuation analysis. *Adv Physiol Educ.* 2002;26(1-4):327-341.

58. Alekov AK, Fahlke C. Channel-like slippage modes in the human anion/proton exchanger ClC-4. *J Gen Physiol.* 2009;133(5):485-496.

59. Sharpe DJ, Wales DJ. Nearly reducible finite Markov chains: Theory and algorithms. *Journal of Chemical Physics.* 2021;155(14):140901.

60. Björketun ME, Tripkovic V, Skúlason E, Rossmeisl J. Modeling of the symmetry factor of electrochemical proton discharge *via* the Volmer reaction. *Catal Today.* 2013;202:168-174.

61. Lewis GN. A New Principle of Equilibrium. *Proc Natl Acad Sci U S A.* 1925;11(3):179-183.

62. Fortin FA, De Rainville FM, Gardner MA, Parizeau M, Gagné C. DEAP: Evolutionary Algorithms Made Easy. *Journal of Machine Learning Research.* 2012;13:2171-2175.

63. Metzner. Transition Path Theory for Markov Jump Processes. *Multiscale Model Sim.* 2009;7(3):1192-1219.

64. Chang R, Eriksen J, Edwards RH. The dual role of chloride in synaptic vesicle glutamate transport. *Elife.* 2018;7.

65. Slater JC. Atomic Radii in Crystals. *Journal of Chemical Physics.* 1964;41(10):3199-3204.

66. Imai K, Mitaku S. Mechanisms of secondary structure breakers in soluble proteins. *Biophysics (Nagoya-shi).* 2005;1:55-65.

67. Hnasko TS, Chuhma N, Zhang H, et al. Vesicular glutamate transport promotes dopamine storage and glutamate corelease in vivo. *Neuron.* 2010;65(5):643-656.

68. Silberberg SD, Magleby KL. Preventing Errors When Estimating Single-Channel Properties from the Analysis of Current Fluctuations. *Biophysical Journal.* 1993;65(4):1570-1584.

69. Yu H, Dhingra RR, Dick TE, Galan RF. Effects of ion channel noise on neural circuits: an application to the respiratory pattern generator to investigate breathing variability. *J Neurophysiol.* 2017;117(1):230-242.

70. Thompson CM, Chao CK. VGLUT substrates and inhibitors: A computational viewpoint. *Biochim Biophys Acta Biomembr.* 2020;1862(12):183175.

71. Metzner P, Schütte C, Vanden-Eijnden E. Transition Path Theory for Markov Jump Processes. *Multiscale Modeling & Simulation.* 2009;7(3):1192-1219.

72. Chen PE, Geballe MT, Stansfeld PJ, et al. Structural features of the glutamate binding site in recombinant NR1/NR2A N-methyl-D-aspartate receptors determined by site-directed mutagenesis and molecular modeling. *Mol Pharmacol.* 2005;67(5):1470-1484.

73. Takamori S, Rhee JS, Rosenmund C, Jahn R. Identification of differentiation-associated brain-specific phosphate transporter as a second vesicular glutamate transporter (VGLUT2). *Journal of Neuroscience.* 2001;21(22).

74. Miyaji T, Echigo N, Hiasa M, Senoh S, Omote H, Moriyama Y. Identification of a vesicular aspartate transporter. *Proc Natl Acad Sci U S A.* 2008;105(33):11720-11724.

75. Cater RJ, Vandenberg RJ, Ryan RM. The domain interface of the human glutamate transporter EAAT1 mediates chloride permeation. *Biophys J.* 2014;107(3):621-629.

76. Chicco D. Ten quick tips for machine learning in computational biology. *Biodata Min.* 2017;10.

77. Rostamipour K, Talandashti R, Mehrnejad F. Atomistic insight into the luminal allosteric regulation of vesicular glutamate transporter 2 by chloride and protons: An all-atom molecular dynamics simulation study. *Proteins.* 2022;90(12):2045-2057.

78. Lei CL, Clerx M, Whittaker DG, Gavaghan DJ, de Boer TP, Mirams GR. Accounting for variability in ion current recordings using a mathematical model of artefacts in voltage-clamp experiments. *Philos Trans A Math Phys Eng Sci.* 2020;378(2173):20190348.

79. Zhang J, Yuan H, Yao X, Chen S. Endogenous ion channels expressed in human embryonic kidney (HEK-293) cells. *Pflugers Arch.* 2022;474(7):665-680.

80. Ullrich F, Blin S, Lazarow K, Daubitz T, von Kries JP, Jentsch TJ. Identification of TMEM206 proteins as pore of PAORAC/ASOR acid-sensitive chloride channels. *Elife.* 2019;8.

8. Acknowledgements

Thanks to Prof. Dr. Christoph Fahlke for offering me the opportunity to do research in his group and being patient and supportive (financially and otherwise) during the arduous process of fitting dozens of kinetic models to five separate experimental datasets. His creative insights and critical commentary were an invaluable driving force during my work.

I would like to express my gratitude to several people who have also contributed to it:

Prof. Dr. Christine Rose, for accepting the role of second reviewer for my work.

Dr. Daniel Kortzak, for serving as an intermediate supervisor, guiding especially the computational aspects of my PhD, including helping me learn the Python programming language effectively from scratch, providing base scripts, and introducing me to kinetic modelling.

Dr. Bettina Kolen, for being my predecessor in the VGLUT electrophysiology project and providing an experimental foundation upon which I built much of my own work.

My future successor as senior VGLUT patcher Victor Lugo for contributing a few measurements to my work and to the publication I share with Bettina, as well as Dr. Piersilvio Longo and Prof. Dr. Jan-Philipp Machtens, for their help with off-site scripts, computation, and data hosting.

And finally secretaries Anita Eckert and her successor Sia Perousakis, who helped out a lot with the various forms of paperwork required by the German tradition of bureaucracy.

A nod to the remaining colleagues in our late institute ICS-4 and born-again institute IBI-1, to a substantial number of whom I spent years providing the services of VGLUT meeting reminder, Lipofectamine secret storage keeper, and seminar planner. Especially our fleeting colleague Dr. Andriy Kazantsev, who showed better judgement by abandoning science and instead choosing to go defend his home country of Ukraine against invading Russians.

A shout-out to my family, who has supported me in what little ways they could from the fairly literal (topographical) side-line, including everyone who has been enjoying the fruits of more lucrative careers and the others who have already finished theirs.

This work is dedicated to three people who did not live to see the conclusion of my work: my uncle Hans Haenen, my last remaining grandfather Jacob Borghans, colleague Doris Höppner-Heitmann, who was arguably the most important technician to us electrophysiologists, and new building office mate PhD student Jan-Gerrit Folkerts. In loving memory, you will be missed.

7. Eidesstattliche Versicherung

Ich versichere an Eides Statt, dass die Dissertation von mir selbstständig und ohne unzulässige fremde Hilfe unter Beachtung der „Grundsätze zur Sicherung gutter wissenschaftlicher Praxis an der Heinrich-Heine-Universität Düsseldorf“ erstellt worden ist.

Jülich, October 2024 Bart Borghans